

# The grain-scale distribution and behaviour of melt and fluid in crystalline analogue systems

Dissertation zur Erlangung des Grades  
„Doktor der Naturwissenschaften“

am Fachbereich Geowissenschaften  
der Johannes Gutenberg–Universität Mainz

Nicolas Peter Walte  
geboren in Bremen

Mainz, Oktober 2004

## Erklärung

Ich versichere hiermit, die vorliegende Arbeit selbständig und nur unter Verwendung der angegebenen Quellen und Hilfsmittel verfasst zu haben.

Mainz, Oktober 2004

Dekanin: Prof. Dr. B. M. W. Ratter

1. Gutachter:

2. Gutachter:

Tag der mündlichen Prüfung:

„Hier sei nur kurz vorausbemerkt: (...) Je besser und feiner eine geologische Struktur bekannt ist, desto vollständiger stimmt sie nach meinen Erfahrungen mit dem sachgemäß ausgeführten Experiment überein, welches der Natur nicht nur durch die Sichtbarkeit seiner Entwicklung, sondern auch durch die Vollkommenheit seiner Aufschlüsse überlegen ist.“

Hans Cloos



## Abstract

The production, segregation and migration of melt and aqueous fluids (henceforth called liquid) plays an important role for the transport of mass and energy within the mantle and the crust of the Earth. Many properties of large-scale liquid migration processes such as the permeability of a rock matrix or the initial segregation of newly formed liquid from the host-rock depends on the grain-scale distribution and behaviour of liquid. Although the general mechanisms of liquid distribution at the grain-scale are well understood, the influence of possibly important modifying processes such as static recrystallization, deformation, and chemical disequilibrium on the liquid distribution is not well constrained. For this thesis analogue experiments were used that allowed to investigate the interplay of these different mechanisms *in-situ*.

In high-temperature environments where melts are produced, the grain-scale distribution in “equilibrium” is fully determined by the liquid fraction and the ratio between the solid-solid and the solid-liquid surface energy. The latter is commonly expressed as the dihedral or wetting angle between two grains and the liquid phase (Chapter 2). The interplay of this “equilibrium” liquid distribution with ongoing surface energy driven recrystallization is investigated in Chapter 4 and 5 with experiments using norcamphor plus ethanol liquid. Ethanol in contact with norcamphor forms a wetting angle of about 25°, which is similar to reported angles of rock-forming minerals in contact with silicate melt. The experiments in Chapter 4 show that previously reported disequilibrium features such as trapped liquid lenses, fully-wetted grain boundaries, and large liquid pockets can be explained by the interplay of the liquid with ongoing recrystallization. Closer inspection of dihedral angles in Chapter 5 reveals that the wetting angles are themselves modified by grain coarsening. Ongoing recrystallization constantly moves liquid-filled triple junctions, thereby altering the wetting angles dynamically as a function of the triple junction velocity. A polycrystalline aggregate will therefore always display a range of equilibrium and dynamic wetting angles at raised temperature, rather than a single wetting angle as previously thought.

For the deformation experiments partially molten  $\text{KNO}_3\text{-LiNO}_3$  experiments were used in addition to norcamphor-ethanol experiments (Chapter 6). Three deformation regimes were observed. At a high bulk liquid fraction >10 vol.% the aggregate deformed by compaction and granular flow. At a “moderate” liquid fraction, the aggregate deformed mainly by grain boundary sliding (GBS) that was localized into conjugate shear zones. At a low liquid fraction, the grains of the aggregate formed a supporting framework that deformed internally by crystal plastic deformation or diffusion creep. Liquid segregation was most efficient during framework deformation, while GBS lead to slow liquid segregation or even liquid dispersion in the deforming areas.



## Contents

<b>Abstract</b> .....	<b>5</b>
<b>Contents</b> .....	<b>7</b>
<b>1. Introduction</b> .....	<b>11</b>
1.1 Melting the Earth.....	12
1.2 Melt segregation, migration, and accumulation.....	13
1.3 Problems of investigating the geology of liquid .....	14
1.4 Experiments with partially-molten systems.....	16
1.5 The importance of the small-scale liquid geometry for the large-scale liquid behaviour .....	16
1.6 Aims and structure of this study.....	17
1.7 Published parts .....	19
<b>2. The liquid distribution in ideal solid-liquid systems in textural equilibrium</b> .....	<b>21</b>
2.1 The wetting angle concept .....	21
2.2 The role of interfacial curvature.....	23
2.3 Liquid distribution in two and three dimensions .....	27
2.4 Recrystallization and Ostwald ripening.....	33
<b>3. Sample preparation and experimental setup</b> .....	<b>39</b>
3.1 Norcamphor experiments.....	39
3.2 Nitrate experiments .....	42
<b>4. Disequilibrium melt distribution during static recrystallization</b> .....	<b>45</b>
Abstract.....	45
4.1 Introduction.....	45
4.2 Experiments .....	47
4.3 Results .....	48

## Contents

4.4	Discussion.....	51
4.5	Conclusion .....	53
<b>5.</b>	<b>Evolution and significance of dynamic wetting angles in a polycrystalline solid–liquid system.....</b>	<b>55</b>
	Abstract.....	55
5.1	Introduction.....	55
5.2	Experiments and Methods .....	60
5.3	Results .....	65
5.4	Discussion.....	70
5.5	Conclusion .....	74
<b>6.</b>	<b>Deformation of melt-bearing systems – insight from in situ grain-scale analogue experiments .....</b>	<b>77</b>
	Abstract.....	77
6.1	Introduction.....	77
6.2	Experiments .....	79
6.3	Results .....	81
6.4	Discussion.....	90
6.5	Conclusions.....	101
<b>7.</b>	<b>The grain-scale behaviour of liquid in crystalline aggregates: A summary and outlook .....</b>	<b>103</b>
7.1	Response of a liquid to a change of the dynamic or the equilibrium wetting angle.....	105
7.2	Driving forces for the change of $\theta_{inst}$ or $\theta_{eq}$ .....	106
7.3	Surface energy driven static recrystallization .....	107
7.4	Gravity and liquid overpressure .....	107
7.5	Chemical disequilibrium between the liquid and the grains.....	110
7.6	Deformation .....	111
	<b>Appendix A: Notation .....</b>	<b>117</b>

## Contents

<b>Appendix B: Movie captions</b> .....	<b>119</b>
Static norcamphor– ethanol experiments.....	119
Overview movies.....	119
Details.....	123
Norcamphor–ethanol deformation experiments.....	124
High strain rate (Motor A).....	124
Medium strain rate (Motor B).....	126
Low strain rate (Motor C).....	128
KNO <sub>3</sub> –LiNO <sub>3</sub> experiments.....	129
<b>References</b> .....	<b>139</b>
<b>Zusammenfassung</b> .....	<b>146</b>
<b>Danksagung</b> .....	<b>149</b>
<b>Lebenslauf</b> .....	<b>151</b>



## 1. Introduction

Throughout the history of the Earth, melt and fluid have played an important role in geological processes at nearly all time and length scales. The early differentiation of the Earth at ca. 4,6 Ga already involved the formation and percolation of metallic and sulphidic melt through a possibly unmolten silicate framework to form the core (e.g. Bruhn et al., 2000, Laporte and Provost, 2000), and at the present time silicate melt is constantly formed beneath middle oceanic ridges, subduction zones, and hot spots as an important part of the global plate tectonic cycle. In fact, the ability of a rocky planet or moon to produce melt in its interior and transport it to the surface is an important indicator for a “living”, geologically active body. Apart from the Earth, other examples of such active bodies in our solar system are the Jupiter moons Io (e.g. Keszthelyi et al., 2001) (with the largest known volcanoes of the solar system) and, possibly, the ice moon Europa (e.g. Stevensen, 2000). Both are shaped by the extrusion of molten sulphur and “ice melt” (water), respectively. These two examples also illustrate that the most important aspect of melt is not so much in its variable nature and chemistry (e.g. water versus metallic, silicate, or sulphuric melt), which is often emphasised by geochemists, but rather its common role to act as a geological shaping agent.

Melt is the liquid part of silicate magma according to the Oxford concise dictionary of Earth sciences (1990). In this thesis the term “melt” is used more broadly to characterize all fused crystalline materials such as silicates, nitrates, or organic crystals (norcamphor, paraffin wax) at elevated temperatures. Substances that are liquid at room temperature such as water or ethanol are therefore excluded from this definition. The term “fluid” is generally used in the Earth sciences to characterize H<sub>2</sub>O and/or CO<sub>2</sub> dominated volatile components that can contain dissolved material. Under crustal conditions there is a miscibility gap between “wet” silicate melt with dissolved water and C-O-H fluid carrying dissolved matter. However, it was shown that under special circumstances e.g. in pegmatites or at mantle pressure this gap may close (Thomas et al. 2000, Bureau and Keppeler, 1999) so that the distinction between melt and fluid becomes meaningless. The term “liquid” is therefore used in this thesis to include all kinds of melts and fluids in geological and experimental systems.

The common characteristic of all liquids in geological systems is their much lower viscosity and a different density compared to the surrounding solid rocks. These properties make liquids of all kinds ideal for transporting mass and energy from the interior of a planet to its surface, and for occupying and migrating through geometric voids of all scales that are created by the interplay of liquids with tectonic forces (e.g. grain edge melt networks, liquid-filled veins and dykes at the small- to medium-scale, batholiths and spreading ridges with newly formed ocean floor at the global scale). Even at the grain-scale, the behaviour of high-

temperature aqueous fluids can be described by the same theories as those for silicate melts (Bulau et al., 1979, von Bargen and Waff, 1986), since the distribution of both is mainly determined by surface energy (see Chapter 2). The use of the general term liquid to include all geologically relevant melts and fluids seems therefore to be appropriate in this thesis as long as a distinction in terms of the chemistry is not necessary.

## 1.1 Melting the Earth

Apart from the liquid outer core, which is the largest molten body of the Earth with ca. 160 billion km<sup>3</sup> of metallic and sulphidic melt, the Earth is essentially solid, since the normal thermal gradient of the Earth in tectonically “inactive” regions (i.e. in the centres of the lithospheric plates away from ridges, subduction zones, and hot-spots) is generally agreed to run below the solidus. The production of melt in the crust or mantle has to be initiated by overstepping the melting temperature of the rocks. This only occurs in special geological environments either by raising the temperature (heating) (+ $\Delta T$ ) or by lowering the temperature of the solidus (e.g. Schmelting, 2000, Best, 2003). Heat can either be produced *in-situ* by the breakdown of radiogenic isotopes of Uranium, Thorium, or Potassium in thickened orogenic crust (England and Thompson, 1984, 1986, Chamberlain and Sonder, 1990), or is added from outside, e.g. by the influx of melt (under- or intraplate) (Huppert and Sparks, 1988, Bergantz, 1989). Lowering of the solidus temperature can be achieved by the addition of aqueous fluids or the production of fluids *in-situ* by the breakdown of hydrous minerals (+ $\Delta X_{\text{fluid}}$ ) (e.g. Wyllie, 1988, Davies and Bickle, 1991), or by decompression melting (- $\Delta P$ ) e.g. of adiabatically uprising mantle in mantle plumes (e.g. hot-spot volcanism) or by passive mantle upwelling (e.g. at mid-ocean ridges or extending rifts) (e.g. McKenzie and Bickle, 1988).

These factors do not exclude each other, and often occur in combination in geological environments. For example, radiogenic heat production (+ $\Delta T$ ) combined with tectonic or erosional denudation (- $\Delta P$ ) could lead to minor melt production in collisional orogens (England and Thompson, 1986). Another good example for the very complex interplay of the different factors is a continental subduction zone such as the Andes. Primary melting of the upper mantle is mainly achieved through the influx of fluids (+ $\Delta X_{\text{fluid}}$ ) formed in the descending slab during high-pressure metamorphic reactions. The C-O-H fluids lower the solidus temperature in the overlying mantle wedge and thereby produce mafic melt (e.g. Wyllie, 1988). The melt rises because of its lower density compared to the mantle until it reaches the continental crust. Because of the lack of a density difference between basalt and crustal material a large proportion of this primary melt does not reach the surface. The

material is under- or intraplated into the lower crust and provides excess and latent (crystallization) heat to the surrounding rocks ( $+\Delta T$ ) that melts partially and produces a secondary, more felsic magma (Huppert and Sparks, 1988, Bergantz, 1989). This magma has a lesser density than the primary melt and the surrounding rocks and therefore has the potential to rise higher in the crust to form plutons or to extrude. Under- and intraplating, and possible tectonic shortening during low-angle subduction thickens the continental crust, which could concentrate radiogenic elements thereby producing extra radiogenic heat ( $+\Delta T$ ) that might further promote crustal melting. Large plutons themselves can give rise to localized partial melting in their contact aureoles. The added heat from the crystallizing magma ( $+\Delta T$ ) raises the temperature until hydrous minerals (mainly muscovite in contact aureoles) of the surrounding rocks become unstable, the released water and possibly magmatic fluids from the pluton lower the solidus ( $+\Delta X_{\text{fluid}}$ ) and a local melt phase is produced (e.g. Storre, 1972, Thompson, 1982) (although breakdown of hydrous minerals is a one-stage melt producing reaction with no intermediate fluid phase, the breakdown of mica still lowers the solidus). This simplified sketch of the complex interplays between geological processes, melting and magma migration shows the importance of the behaviour of liquid in geologically active regions and the wide range of scales involved in these processes.

## 1.2 Melt segregation, migration, and accumulation

Although many parameters such as the pressure and temperature ranges of the melting reactions or the properties and percentage of the produced melt phase are quite well understood (e.g. Brown, 1994, 2001, and references therein), many other important questions are less well constrained: How does the melt segregate out of its host rock? By what process does the melt migrate upwards? How does the melt accumulate to form large igneous bodies? The answers to these questions determine the time scales involved in magmatic events, the efficiency of melt segregation, and the rates of which melt can be transported from the source region to the emplacement regions or to extrusion. Secondary questions like the chemical equilibrium between melt and host rock and the influence of heterogeneous source regions also depend on these processes. The first melt that is formed at the contact of different minerals is dispersed throughout the host rock in the form of small droplets. These micrometer scale droplets, which only make up a few volume percent of the host rock may eventually form large plutons or batholiths that shape the crust as we currently observe it. This process, which involves accumulation of the liquid pocket volume over more than 20 orders of magnitude (Bons and van Milligen, 2001, Bons et al., 2004), is traditionally separated into steps of segregation, accumulation, migration, and emplacement. Investigation

of segregation is concerned with the question of how and why the extraction of the dispersed melt droplets from the host rock e.g. into dykes or melt-filled shear zones is accomplished. Migration models deal with the mode of melt transport to the emplacement level or to the extrusion e.g. through diapirism or dyking and the accompanying time scales. Accumulation of melt into a larger body of melt can be either before migration, as is supposed for models of diapirism (e.g. Paterson and Vernon, 1995), or towards the end of the migration process, as in models of melt transport through dykes and hydrofractures (e.g. Clemens and Mawer, 1992). This also influences the mechanics of the final emplacement that is mainly investigated in now exposed granites. Although it is clear that all these processes have to occur at some stage, many authors have doubted the possibility of a clear separation of these stages. For example, models that suggest melt segregation and migration in the mantle by compaction and porous flow (McKenzie, 1984) integrate these two processes into one. If porous flow becomes episodic and the melt is transported in the form of porosity waves (e.g. Scott and Stevenson, 1986, Richter and McKenzie, 1984), segregation, migration, and the formation of magma chambers and plutons were suggested to occur simultaneously (Rabinowicz et al, 2001). Other opposing models suggest melt migration in the mantle or the crust by melt induced embrittlement in the form of large open or self-propagating dykes (Spence and Turcotte, 1990, Clemens and Mawer, 1992, Kelemen et al. 1997, and references therein), or as a self-organized process of interacting hydrofractures, that also combines medium- to large-scale segregation, migration, and accumulation (Bons and van Milligen, 2001). Recently, Connolly and Podladchikov (2004) have attempted to integrate the model of propagating porosity waves with fracture and dyke transport. Their “swiss cheese” model assumes kilometre-scale spherical to ellipsoidal regions in the lower crust that contain a raised melt-fraction, which is either contained in a “classical” grain-scale liquid network (porous flow) or in a brittle fracture and dyke network. They argue, that both networks would propagate in the form of three-dimensional waves (Connolly and Podladchikov, 2004).

### **1.3 Problems of investigating the geology of liquid**

Although the last Section only gives a short overview of current ideas on segregation, accumulation and migration of liquid, the wide range of often contrasting models for the behaviour of liquid is apparent. For example, melt migration by continuous porous flow or in porosity waves is a very slow process which occurs with velocities in the range of mm per year (Scott and Stevenson, 1986, Schmeling, 2000), while melt transport in dyke networks or through self-propagating hydro-fractures can reach up to super-sonic velocities (Spence and Turcotte, 1990). This results in completely opposite predictions regarding chemical solid-

liquid equilibrium and potential liquid-fluxes. Part of the problem of the apparent confusion in these important questions regarding the functioning of the Earth system is that most of the models for large-scale liquid behaviour cannot be adequately tested in the field or the laboratory. Most geological research relies on the ability of geological materials to maintain a memory of (part of) their history that is recorded e.g. in structures, in mineral assemblages, in the geochemistry, and in fossils. However, when considering the geology of liquids, even the exact geometry of once-molten systems is very hard to attain at any scale. All traces of melt that can be observed and mapped at outcrop or thin Section scale do generally not represent the geometry and distribution while it was liquid. Even the interpretation what really once represented melt is often controversial on the decimetre scale and below. For example, the geochemical composition of leucosomes in migmatites rarely equal the expected composition of eutectic melt from the host rock, and they are therefore sometimes interpreted as cumulates (Ellis and Obata, 1992). At the grain-scale, thin monomineralic feldspar- or quartz fringes were described and interpreted as pseudomorphs of former melt although they clearly do not represent melt composition (Rosenberg and Riller, 2000, Sawyer, 2001, Marchildon and Brown, 2002). Even if the geometry and extent of former melt can be observed or inferred in nature, general conclusions about magma production, accumulation and migration in the Earth have to be treated with great care because the frozen melt that can be observed in outcrop or thin Section represents the melt that did **not** make it upwards to an intrusion or eruption. The term “failed granite” has been used for migmatites in the context of this apparent paradox between the melt that did segregate to form plutons or volcanoes but that cannot be observed, and melt that can be observed but that definitively did not contribute to a pluton or volcano (see Brown, 1994, for discussion). If non-continuous melt transport such as porosity waves or hydrofractures contributes a significant part to melt transport in the Earth, it follows that even if the exact geometry of a natural system is established at a certain time, the past and future of the system cannot be inferred automatically. For example, a large self-propagating melt-filled hydrofracture (e.g. Clemens and Mawer, 1992) might have just passed or is about to pass a volume of rock and might leave only small, melt-filled dykes and leucosomes as traces of the migration and accumulation event. To infer the amount of melt transport from the form and volume of the traces would be like trying to infer the amount of water that ran through a garden hose from investigating the number and form of the leftover droplets. All these obstacles for the understanding of partially-molten systems and the opposing models of liquid migration can be summarized with the non-permanent nature of geological liquids and the inability of the geologist to observe these lower crustal or upper mantle systems in-situ over the time of a complete magmatic cycle.

## 1.4 Experiments with partially-molten systems

Some of the problems discussed in the last Section were partly overcome by performing experiments with partially-molten and liquid-bearing natural rocks or aggregates of rock-forming minerals. High-temperature liquid-bearing experiments allow investigating the liquid distribution during static conditions and during deformation. The results can be used to calibrate quantitative models that predict parameters such as permeability of liquid-bearing rocks, which can in turn be used for models of segregation and large-scale liquid migration. One drawback of these experiments is that only snapshots of the ongoing processes in such an aggregate can be observed. It is not possible to run high-temperature experiments and observe the internal microstructure at the same time (*in-situ*), yet, so there is no complete control of the liquid behaviour over time. This drawback can be overcome by liquid-bearing *in-situ* analogue experiments. For these experiments analogue materials such as organic crystals plus melt are used (e.g. Means and Park, 1994, Bauer et al. 2000, Rosenberg and Handy, 2000) that are thought to simulate the behaviour of natural systems in some respect, and that can be used to better understand both nature and high-temperature experiments.

Another unresolved problem of all laboratory experiments is that they can only be performed at a certain scale. The investigations of high-temperature solid-liquid experiments are limited to the distribution and behaviour of liquid at the grain-scale. All scaling of features that can be observed in such experiments, such as small-scale shear zones to large-scale natural features (e.g. Rosenberg and Handy, 2000, Holtzmann et al. 2003) have to be considered carefully in order to be justified (see Chapter 6). This is especially so because the grain-scale behaviour and distribution of liquid is determined or influenced by surface and grain boundary energy (e.g. Bulau et al. 1979), chemical disequilibrium (e.g. Holness and Siklos, 2000), and deformation (e.g. Daines and Kohlstedt, 1997, Holtzmann et al, 2003a, b), while larger bodies of liquid are mainly influenced by buoyancy forces and deformation (e.g. Spence and Turcotte, 1990), so that there is an important difference in behaviour.

## 1.5 The importance of the small-scale liquid geometry for the large-scale liquid behaviour

Although it is not possible to infer directly from the small- (sub-cm) to the large-scale behaviour of liquid (see above), the large-scale behaviour of liquid is nevertheless strongly influenced by its distribution at the small-scale. For example, melt segregation and migration by compaction and porous flow in the mantle (McKenzie, 1984) depends on the existence of a three-dimensionally connected liquid network at low liquid fractions. More specifically,

quantitative modelling of the rate and velocity of melt migration requires the knowledge of the porosity-permeability relation of the rocks which is determined by the exact geometry of this network (von Bargen and Waff, 1986, Schmeling, 1986). Many theoretical and experimental studies have therefore been performed to specify the porosity-permeability relation of simplified geological systems, such as olivine plus mafic or ultramafic melt. Early results (e.g. Bulau et al., 1979, von Bargen and Waff, 1986, Wark and Watson, 1998) indicated that the permeability follows a Blake-Carman-Cozony relation (Carman, 1956), i.e. the permeability is proportional to the porosity to the power of 2 or larger. Modelling based on these results indicated that low liquid fractions < 1 vol.% would already be mobile and could segregate efficiently out of the mantle (McKenzie, 1984). This is confirmed by geochemical investigations, that also suggest efficient melt segregation below 1 vol.% melt-fraction (e.g. O’Nions and McKenzie, 1993). However, studies that focussed on the occurrence of disequilibrium features in the olivine-melt system (Waff and Faul, 1992, Faul, 1994, 1997, 2000, Cmíral et al., 1998) questioned the mobility of melt with a low liquid-fraction in the mantle and suggested a percolation threshold at ca. 2.5 vol. % (Faul, 1997). On the other hand, even the existence of disequilibrium features was questioned by Wark et al. (2003). They envisioned a regular liquid network with only minor modifications due to varying grain-size (see Chapter 4). This debate illustrates that even the experimentally exsible grain-scale distribution of liquid is not fully agreed upon, yet, although it forms the essential base for further investigation of liquid behaviour at all scales.

## 1.6 Aims and structure of this study

This study uses analogue experiments to investigate the grain-scale distribution and behaviour of liquid, including the role of various controlling factors for the equilibrium and disequilibrium distribution of the liquid. Although several solid-liquid analogue studies have previously been performed (Means and Park, 1994, Park and Means, 1996, Rosenberg and Handy, 2000, Bauer et al., 2000, Rosenberg and Handy, 2001), a systematic *in-situ* investigation of liquid distribution in a simple, well-constrained system with low-anisotropy crystals was missing. The aim of this study was to find suitable analogues for partially molten rock-forming minerals with low-anisotropy crystals that could be observed *in-situ*, with a special emphasis on the grain-scale distribution and segregation of the liquid phase. Further aims were to test the degree that the grain-scale liquid distribution in the analogue experiments agrees with theoretical predictions of liquid distribution in model systems at static conditions and during deformation. The content and structure of this study can be summarized as follows:

- The theoretical foundations for the “equilibrium” liquid distribution in simplified model systems are summarized in **Chapter 2**, and some of the implications for natural systems are discussed. The role of solid-solid and solid-liquid surface energy for the distribution of liquid is emphasised. Recrystallization and Ostwald ripening are also treated as important mechanisms that influence the microstructure in high-temperature systems.
- Several liquid-bearing crystalline systems are introduced in **Chapter 3**, which are suitable analogues for partially molten rock-forming minerals. They display a low-anisotropy solid-liquid surface energy and the solid-liquid microstructures are easily observable during analogue experiments.
- The main topic of **Chapter 4** is the interplay between surface energy and grain boundary area reduction recrystallization for the distribution of liquid. The formation and the stability of “disequilibrium” features and their implications for the large-scale liquid migration is discussed and compared with the results of high-temperature experiments.
- The solid-liquid wetting angle is investigated in detail in **Chapter 5**. The connection between dynamic wetting angles and the triple junction migration velocity is investigated and the implications for the liquid distribution are discussed.
- The behaviour of liquid-bearing systems during deformation is the subject of **Chapter 6**. Parameters such as liquid-fraction, rheological strength of the grains and strain rate are varied in the analogue experiments and the interplay between these parameters, the deformation mechanism, and the liquid distribution is investigated.
- The results of the previous Chapters are summarized in **Chapter 7** with an emphasis on the alteration of the small-scale liquid distribution due to different modifying mechanisms such as recrystallisation, chemical disequilibrium, liquid pressure, and stress/strain.

The emphasis of this work was on simple and fundamental small-scale processes that can be expected to occur in all crystalline liquid-bearing systems, regardless of the nature of the liquid. Because of the different parameters that determine liquid behaviour at the small and the large-scale (surface energy dominated versus buoyancy dominated, see Section 1.4), no attempts were made to scale static or deformational features observed in the experiments to larger-scale natural features. The results of the experiments were only interpreted in terms of their relevance for processes in natural systems at comparable scales. However, by

investigation of the liquid behaviour at the grain-scale with novel methods, this study aimed to contribute to a better foundation for understanding the behaviour of liquid at all scales.

## 1.7 Published parts

Parts of this thesis have already been published or are under review for international journals. These parts were included as the Chapters 4, 5, and 6 in the thesis. These Chapters have not been changed from the original manuscripts, only the lay-out and the figure numbers have been brought in line with the rest of the thesis. These parts are:

Walte, N.P., Bons, P.D., Passchier, C.W., Koehn, D., 2003. Disequilibrium melt distribution during static recrystallization. *Geology* 31, 1009-1012. (Chapter 4)

Walte, N.P., Bons, P.D., Passchier, C.W., 2004. Evolution and significance of dynamic wetting angles in a polycrystalline solid–liquid system. *Journal of Geophysical Research*, submitted. (Chapter 5)

Walte, N.P., Bons, P.D., Passchier, C.W., 2004. Deformation of melt-bearing systems – insight from in situ grain-scale analogue experiments. *Journal of Structural Geology*, submitted. (Chapter 6)

The co-authors were my supervisors for the Ph.D. project. They introduced me to the experimental and analytical techniques, and reviewed and corrected the manuscripts.



## 2. The liquid distribution in ideal solid-liquid systems in textural equilibrium

The grain-scale distribution of a liquid in a polycrystalline aggregate is determined by the tendency of the system to minimise its total surface energy. The surface energy  $\sigma$  is the excess energy per unit boundary area between two solid grains ( $\sigma_s$ ) or between a grain and liquid ( $\sigma_{sl}$ ), that is formed due to bonding mismatches between phases or grains. The total surface free energy of a system  $\Sigma = \sum_i \sigma_i A_i$  is reduced by two general mechanisms: firstly, reorientation and rebalancing of solid-solid and solid-liquid interSections leads to an adjustment of solid-solid-liquid contact angles (the dihedral or wetting angle  $\theta$ ) and changes the ratio of the wet (solid-liquid) to the dry (solid-solid) surface area (e.g. by sintering). This process minimizes the total surface energy for a given mean grain-size. Secondly, the total grain boundary area of the system is reduced by surface energy driven static recrystallization and Ostwald ripening, which leads to a continuous increase of grain-size. The theory of the readjustment processes and the implications for liquid distribution and wetting angles is treated in the Sections 2.1–2.3. Static liquid-assisted recrystallization and Ostwald ripening are treated in Section 2.4.

### 2.1 The wetting angle concept

The dihedral or wetting angle ( $\theta$ ) is the angle which is formed at a junction between either three different phases (e.g. solid-liquid-vapour) or between two adjacent grains and a liquid (or vapour) phase (Fig. 2.1). The wetting angle in a polycrystalline system containing a liquid phase is an important property determining the tendency of the liquid to either disperse throughout the aggregate (at a “low”  $\theta$ , see below) or to segregate from the aggregate solely due to the minimisation of the total surface energy of the system (at a “high”  $\theta$ ). The reorientation of the three-phase line interSections between the liquid and the solid grains to achieve a minimum energy configuration results in an equilibrium wetting angle that is constant throughout an ideal system. The term “ideal system” is used here in accordance with other authors (e.g. Bulau et al., 1979) for a monomineralic crystalline system with isotropic solid-solid and solid-liquid surface energy between the liquid and the minerals that is independent of crystal lattice orientation. One consequence is that dispersed minerals surrounded by liquid assume a spherical shape like drops of oil in water, without developing crystal facets (Fig. 2.1d). The fundamental physical behaviour of C-O-H fluid equals the behaviour of melt in an ideal system with respect to liquid distribution (Bulau et al, 1979).

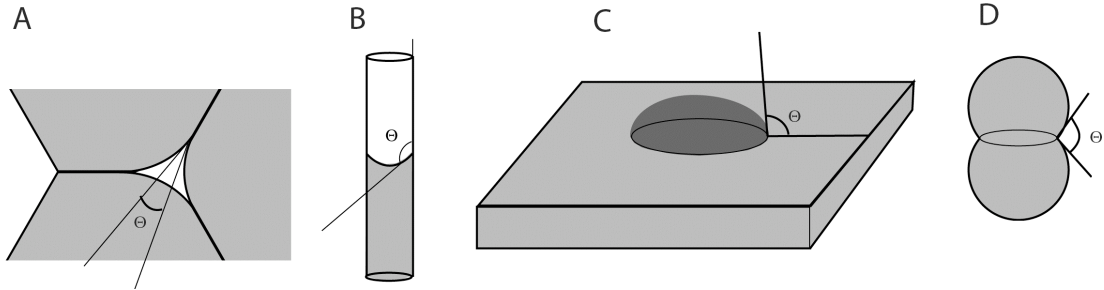


**Fig. 2.1.** Different examples for dihedral angles or wetting angles ( $\theta$ ). **A:** Solid-solid-liquid wetting angles in a polycrystalline aggregate between three grains and a triangular liquid pocket. **B:** Solid-liquid-vapour wetting angle at the meniscus of a capillary tube. **C:** Solid-liquid-vapour wetting angle of a drop on a planar surface. **D:** Solid-solid-liquid wetting angle at the contact of two isotropic grains surrounded by liquid.

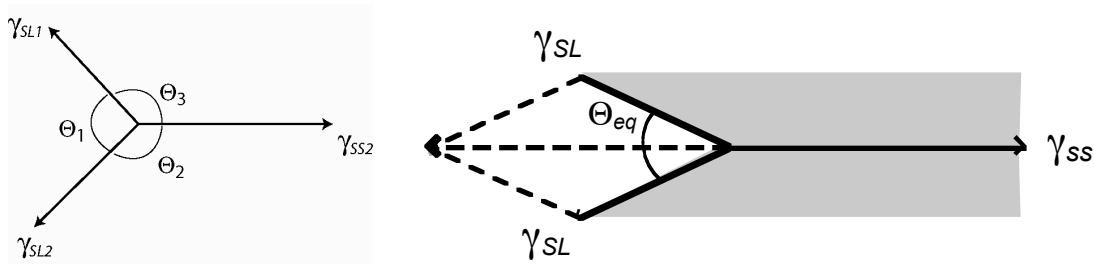


**Fig. 2.2.** Vector diagrams that balance the solid-solid and the solid-liquid surface tensions. The equilibrium wetting angle is formed as a result of the ratio between the surface tensions.

One way of deriving the wetting angle equation is by balancing the surface-tension forces that act along the three boundaries of a triple junction. Surface tension is a vector force per unit length of boundary interSection [1 N/m] that is numerically equivalent to the surface energy [1 J/m<sup>2</sup>] (e.g. Faul, 2000). In liquids and isotropic crystals the direction of the surface tension vector lies in the plane of the interfaces and acts perpendicular to the line interSection between the phases. A triple junction between two solid grains and a liquid is in mechanical equilibrium, i.e. it is stationary, if the **vector** sum of the three surface tensions equals zero (Fig. 2.2)

$$\sigma_S + \sigma_{SL1} + \sigma_{SL2} = 0, \quad (2.1)$$

with  $\sigma_S$ ,  $\sigma_{SL1}$  and  $\sigma_{SL2}$  as the vectors of the solid-solid, the first solid-liquid, and the second solid-liquid surface tension, respectively. Surface tension in Fig. 2.2 acts along each interface away from the interSection with a magnitude of  $\sigma$  for each unit of interSection length normal to the figure. Balancing the forces perpendicular to  $\sigma_S$ ,  $\sigma_{SL1}$ , and  $\sigma_{SL2}$  results in

$$\sigma_{SL1} \sin(180^\circ - \theta_3) = \sigma_{SL2} \sin(180^\circ - \theta_2),$$

$$\gamma_{SL1} \sin(180^\circ - \theta_3) = \gamma_{SL2} \sin(180^\circ - \theta_1) \text{ and}$$

$$\gamma_{SL1} \sin(180^\circ - \theta_1) = \gamma_{SL2} \sin(180^\circ - \theta_2),$$

with  $\gamma_{SL}$ ,  $\gamma_{SL1}$  and  $\gamma_{SL2}$  as the scalar magnitudes of  $\gamma_{SL}$ ,  $\gamma_{SL1}$  and  $\gamma_{SL2}$ . This can be rewritten as

$$\gamma_{SL} / \sin(180^\circ - \theta_1) = \gamma_{SL1} / \sin(180^\circ - \theta_2) = \gamma_{SL2} / \sin(180^\circ - \theta_3).$$

Since  $\sin(180^\circ - \theta) = \sin \theta$

$$\gamma_{SL} / \sin \theta_1 = \gamma_{SL1} / \sin \theta_2 = \gamma_{SL2} / \sin \theta_3. \quad (2.2)$$

If  $\gamma_{SL1}$  and  $\gamma_{SL2}$  is identical ( $\gamma_{SL}$ ) and  $\gamma_{SL}$  independent of the crystal lattice orientation as is the case for the ideal system, the equilibrium situation is characterized by only one angle  $\theta_{eq}$  and the equation can be simplified to

$$2\cos(\theta_{eq}/2) = \gamma_{SL} / \gamma_{SL} \quad (2.3)$$

(2.3) is the wetting angle equation and  $\theta_{eq}$  the equilibrium wetting angle for isotropic systems. The important point is that the wetting angle is solely determined by the ratio of the solid-solid to the solid-liquid surface energy. All solid-solid-liquid triple junctions in a polycrystalline system strive towards this angle by migration and readjustment. Wetting angles are not only found in polycrystalline systems but also for example in the shape of a droplet on a flat surface (a solid-liquid-vapor angle) or at a meniscus in a capillary tube (e.g. de Gennes, 1985, Léger and Joanny, 1992) (Fig. 2.1). The wetting angle in anisotropic systems varies according to the degree of anisotropy and the crystal lattice orientation of the adjacent grains. The derivation of the wetting angle for this case is much more complicated and can be found e.g. in Zhu and Hirth (2003) and in Laporte and Provost (2000b) for the simplified two-dimensional case.

## 2.2 The role of interfacial curvature

### 2.2.1 Dependence of pressure on the curvature

After deriving the wetting angle equation in the previous Section we have to consider the effect of curved grain and phase boundaries before we can attempt to put the ingredients together to understand the geometry of the grain-scale liquid distribution in isotropic systems

in equilibrium. There are two complementary ways to consider the effect of curvature: one considers the over- or under-pressure of a liquid in equilibrium with a solid, that is the direct result of the curvature and the surface tension of the boundary (the pressure inside a balloon is slightly higher than in the surrounding air as a direct consequence of its radius and of the tension in the fabric of the balloon). The other way goes one step further and considers the change of chemical potential of a curved surface relative to a flat surface of the same substance, that is the result of the pressure difference. The derivations presented here follow along the derivations of Bulau et al. (1979).

Consider a single isotropic crystal in thermodynamic equilibrium with a surrounding liquid in a hydrostatic stress state. The crystal assumes a spherical shape due to the single valued  $\gamma_L$  so that the surface area is minimized. The system is isobaric and the total volume can vary. The Helmholtz free energy variation  $dF$  and the Gibbs free energy variation  $dG$  are given by

$$dF = -dw + \sum \mu_i dn_i \quad (2.4)$$

with the work  $w$ , the chemical potential  $\mu_i$  and the change in moles  $dn_i$  of component  $i$ , and

$$dG = dF + d(PV)_{\text{total}} \quad (2.5)$$

with the pressure  $P$  and the volume  $V$ , respectively. Combining (2.4) and (2.5) and expanding results in

$$dG = -dw + d(PV)_{\text{total}} + \mu_s dn_s + \mu_d dn_d + \mu_l dn_l \quad (2.6)$$

with  $dn_s$  indicating material in the solid,  $dn_d$  dissolved material, and  $dn_l$  material of the solvent. The number of moles of the solvent is constant:  $dn_l = 0$ , material dissolved from the solid is added to the liquid and vice versa:  $dn_s = -dn_d$ , and in equilibrium the chemical potentials in the solid and the liquid are equal by definition:  $\mu_s = \mu_d$ . (2.6) therefore becomes

$$dG = -dw + d(PV)_{\text{total}}. \quad (2.7)$$

The work  $w$  consists of three parts: work for increasing the crystal surface area  $-\gamma dA$ , work to increase the volume of the solid  $P_s dV_s$ , and work to increase the liquid volume  $P_l dV_l$ .  $dV_l$  is separated into the change of liquid volume due to volume change of the crystal and the total volume change of the system ( $dV_l = -dV_s + dV_{\text{total}}$ ):

$$-dw = -P_s dV_s - P_l(-dV_s + dV_{total}) + \gamma dA \quad (2.8)$$

and

$$d(PV)_{total} = P_{total} dV_{total} + V_{total} dP_{total} \quad (2.9)$$

since the system is isobaric  $dP_{total} = 0$  and  $P_{total} = P_l$ ,

$$d(PV)_{total} = P_l dV_{total} \quad (2.10)$$

Substituting (2.8) and (2.10) in (2.7) results in

$$dG = (P_l - P_s) dV_s + \gamma dA \quad (2.11)$$

$dV_s$  of a sphere is  $4\pi r^2 dr$  and  $dA = 8\pi r dr$ . In equilibrium  $dG = 0$  and therefore

$$\gamma P_s = P_s - P_l = 2\gamma / r = 2\gamma^* k^s, \quad (2.12)$$

with the curvature  $k^s = 1/r$  of a sphere or in a two dimensional system. In a three-dimensional system the mean curvature has to be substituted  $k_{mean}^s = 0,5(1/r_1 + 1/r_2)$ .  $r_1$  and  $r_2$  are the radii of principal curvatures that are oriented perpendicular to each other at the point of interest. That means that  $k_{mean}$  can be zero if the principle radii are oriented in opposite directions (a saddle geometry). The equation for the solid over- or under pressure in a three-dimensional system therefore becomes

$$\gamma P_s = 2\gamma^* k_{mean}^s. \quad (2.13)$$

Equation (2.13) can be used to calculate a local under- or overpressure  $\gamma P$  exerted by the surface tension of curved grain- or phase-boundaries between adjacent phases or phase regions while in equilibrium.

### 2.2.2 The dependence of chemical potential on the curvature

Considering the effect of curvature for the chemical potential we start with the Gibbs criterion for equilibrium of a component  $i$  in a partially molten system

$$\mu_i^s = \mu_i^l \quad (2.14)$$

The standard thermodynamic identity is

$$\mu_i^s = \mu_i^0 + RT \ln a_i^k \quad (2.15)$$

$\mu_i^0$  is defined as the chemical potential of component  $i$  at a flat crystal surface (i.e.  $k_{\text{mean}}^s = 0$ ) at the temperature and pressure of interest,  $a_i^k$  is the activity of the component  $i$  due to the non-zero mean curvature  $k_{\text{mean}}^s$ . For a change of curvature at constant  $T$  and  $P_l$ ,  $P_s$  is changed and a new equilibrium is reached from (2.14)

$$(\partial \mu_i^s / \partial P_s)_{T, P, n_i^s, n_i^l} = (\partial \mu_i^l / \partial P_s)_{T, P, n_i^s, n_i^l} \quad (2.16)$$

Using the partial molar volume  $V_i^s = (\partial \mu_i^s / \partial P_s)_{T, P, n_i^s, n_i^l}$  and substituting (2.15) in (2.16) we get

$$V_i^s = RT (\partial \ln a_i^k / \partial P_s)_{T, P, n_i^s, n_i^l} \quad (2.17)$$

with the activity  $a_i^k$  of component  $i$  in phase  $k$ . If equation (2.13) is used in differential form  $dP_s = 2\gamma_{sL} dk_{\text{mean}}^s$ , and assuming that  $V_i^s$  is independent of  $P_s$ , we obtain

$$2 V_i^s \gamma_{sL} dk_{\text{mean}}^s = RT d \ln a_i^k \quad (2.18)$$

Integration from  $k_{\text{mean}}^s = 0$  to  $k_{\text{mean}}^s$  results in the Gibbs-Thomson equation (Gibbs, 1931)

$$\ln (a_i^k / a_i^0) = 2\gamma_{sL} V_i^s k_{\text{mean}}^s / RT \quad (2.19)$$

Using the fact that by definition  $a_i^0 = 1$  ( $k_{\text{mean}}^s = 0$ ) and substituting (2.19) in (2.15) results in

$$\mu_i^s = \mu_i^0 + 2\gamma_{sL} V_i^s k_{\text{mean}}^s \quad (2.20)$$

(2.20) is the equation for the chemical potential of component  $i$  as a function of the mean curvature  $k_{\text{mean}}^s$ . The higher the mean curvature of an interface, the higher is the chemical potential of the interface. From equation (2.20) follows, that the chemical potential difference is proportional to the mean curvature  $\mu_i^s \sim k_{\text{mean}}^s$  and therefore inversely proportional to the radius of spherical grains.

For questions of liquid distribution in a polycrystalline system, the mean curvature is usually defined with respect to the liquid pocket:  $k_{\text{mean}}$  is positive if the radii of curvature are oriented towards the liquid pocket and negative if oriented towards the grains ( $k_{\text{mean}} = -k_{\text{mean}}^s$ ). Additionally, under- or overpressure is usually defined with respect to the liquid  $\Delta P_l = -\Delta P_s$ . The equations (2.13) and (2.20) can therefore be rewritten to

$$\Delta P_l = 2\gamma_{l/s} k_{\text{mean}} \quad (2.21)$$

and

$$\Delta P_i^s = \Delta P_i^0 - 2\gamma_{l/s} V_i^s k_{\text{mean}}. \quad (2.22)$$

These definitions of curvature and over- or under-pressure with respect to the liquid phase are used throughout this work with the exception of Section 2.4.2 (Ostwald ripening).

### 2.3 Liquid distribution in two and three dimensions

The distribution of liquid in an ideal two-phase (one solid + one liquid) system in perfect equilibrium is fully constrained by the considerations of Section 2.1 and 2.2: the ratio of  $\gamma_{s/l}$  to  $\gamma_{l/s}$  that determines the wetting angle in equilibrium  $\Delta_{eq}$  and the dependence of pressure or chemical potential on interfacial curvature (Bulau et al. 1979, von Bargen and Waff 1986). Although the exact three-dimensional grain-scale geometry of melt in an aggregate has to be derived numerically even for idealized aggregates with a constant grain size (von Bargen and Waff 1986), especially when introducing anisotropic  $\gamma_{l/s}$  (see Laporte and Provost 2000b, Zhu and Hirth 2003), many important constraints for liquid distribution can be inferred by applying the results of Chapter 2.2.

#### 2.3.1 Equilibrium distribution in two dimensions

Consider a simple two-dimensional system with two triangular melt pools situated at three-grain interstices (Fig. 2.3). Since  $\Delta_{eq}$  is constant in an ideal system (equation (2.3)), the melt pools can only differ by their area and by their interfacial curvature. Three cases are distinguished in a 2-D system: at  $\Delta_{eq} < 60^\circ$  the curvature is always negative, at  $\Delta_{eq} = 60^\circ$  the curvature is zero, and at  $\Delta_{eq} > 60^\circ$  the curvature is always positive (Fig. 2.4a). The smaller the liquid-pool for the first case, the higher the negative interfacial curvature, and the smaller the pool for the latter case, the higher the positive interfacial curvature. This means that the liquid of the smaller triangle of Fig. 2.3a ( $\Delta_{eq} < 60^\circ$ ) has a lower pressure  $\Delta P$  with respect to the

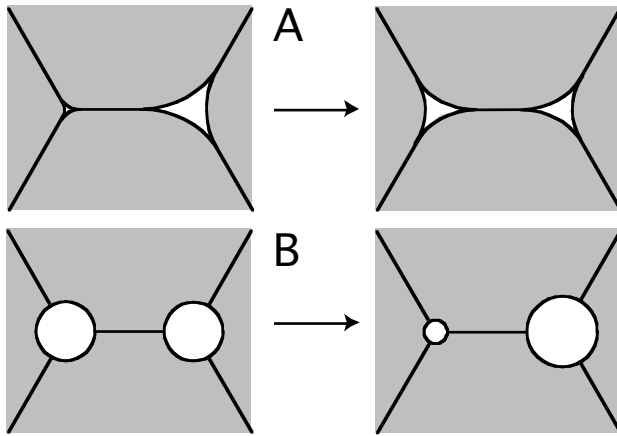


**Fig. 2.3.** Liquid distribution in two dimensions. **A:** If the wetting angle is  $<60^\circ$  the liquid in the smaller pocket has a slightly lower pressure than the liquid in the larger pocket. Liquid is drawn from the large into the small pocket and the sizes are equalized. **B:** If the wetting angle is  $>60^\circ$ , the liquid in the smaller pocket has a higher pressure than the liquid in the larger pocket. Small, initial size differences are thereby enhanced.

larger liquid pool (from equation (2.21)) and the curved grain boundaries have a higher chemical potential than the grain boundaries of the larger liquid pool (from equation (2.22)). If there is a connection between the liquid patches the system strives towards an equilibration of the areas (Fig. 2.3a) e.g. by dissolution-precipitation processes. The opposite effect happens at positive curvature ( $\varphi_{eq} > 60^\circ$ , Fig. 2.3b): the smaller the liquid pool, the higher the overpressure from (2.21) and the lower the chemical potential from (2.22). If connected, the liquid will segregate completely into the largest pool and finally out of the system, if that is possible (Fig. 2.3b). This is the first fundamental relation between wetting angle and liquid distribution in equilibrium:

*If the wetting angle is below  $60^\circ$  (below  $\sim 70,53^\circ$  in three dimensions, see below), all solid-liquid interfaces have a negative (mean) curvature. Initial liquid size variations are equalized and the liquid has the tendency to spread evenly throughout the granular matrix. If the wetting angle is above  $60^\circ$  (above  $\sim 70,53^\circ$  in three dimensions), the solid-liquid interfaces in three grain junctions have a positive curvature, any initial liquid patch size variation is enhanced and the liquid collects and segregates out of the three-grain junctions.*

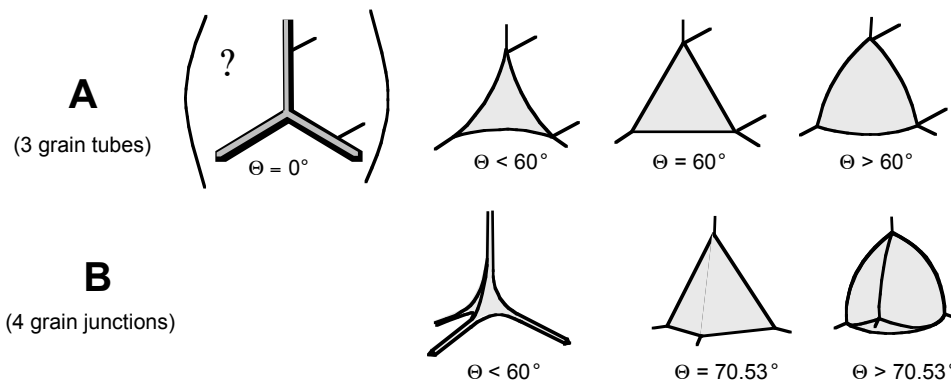


**Fig. 2.4.** Schematic representation of liquid-phase equilibrium geometry. **A:** Perpendicular to three-grain tubes. **B:** Four-grain junctions. An interconnected liquid network only forms at  $\varphi < 60^\circ$ . The case of  $\varphi = 0^\circ$  does not fulfill the requirement of a constant curvature and is therefore questioned.

This process has been proposed as a potentially important segregation mechanism for solid-liquid systems with higher wetting angles (Jurewicz and Watson, 1985).

### 2.3.2 *Equilibrium distribution in three dimensions*

In a three-dimensional system with a low liquid fraction, the liquid can occupy high-energy locations such as four-grain corners, three-grain junctions, and two-grain boundaries depending on the wetting angle (Fig. 2.4). In three dimensions the same general principles apply as in two-dimensional systems, i.e. a single equilibrium wetting angle is approached at all solid-solid-liquid junctions and, at a low wetting angle ( $\theta < 70.53^\circ$ , see below), all solid-liquid interfaces strive towards a uniform negative curvature throughout the system. However, in contrast to two-dimensional systems, where uniform curvature consists of circle segments with a single radius, the mean curvature  $k_{\text{mean}}$  in three-dimensional systems has two perpendicular principal radii (see Section 2.2.1). Finding the liquid geometry for a given liquid fraction and wetting angle is more complicated, because for a given mean curvature, the principal radii can be varied as an additional variable. For example, for a wetting angle  $< 60^\circ$  and at equilibrium, the interfacial mean curvature in the liquid-filled grain-edge tubes is identical to the mean curvature in the four-grain interstices. Consider the special case of a wetting angle of  $60^\circ$  in an ideal solid-liquid system to clarify the consequences of a constant mean curvature for the liquid distribution. At  $\theta_{\text{eq}} = 60^\circ$ , the solid-liquid interfaces in the three-grain tubes approach a mean curvature of zero, if the liquid fraction is very low (Fig. 2.4a). However, the interfaces of the four-grain junctions still have a negative curvature at  $\theta_{\text{eq}} = 60^\circ$ , because a tetrahedron with flat faces has a slightly higher wetting angle of  $70.53^\circ$  at its side (Fig. 2.4b). That means that the liquid in the four-grain interstices experiences a slight underpressure with respect to the grain tubes so that the grain tubes become unstable and the liquid collects in the four-grain junctions. Alternatively, one can also consider the pinch off to be the result of a lower chemical potential of the grain tube walls with respect to the four-grain junctions, so that material precipitates here and finally closes the tubes. If the wetting angle is below  $60^\circ$ , the mean curvature of the grain tubes can equilibrate with the curvature in the four-grain junctions by adjusting the tube perimeter. As the angle approaches  $60^\circ$ , the tube perimeter becomes very small and finally pinches off. A lowered wetting angle produces a wider tube perimeter at a constant liquid fraction. This is the second fundamental relation between wetting angle and liquid distribution in equilibrium:

*If the wetting angle is below  $60^\circ$ , a three-dimensional liquid network is established regardless of liquid fraction. At a wetting angle of  $60^\circ$  or above the liquid network breaks down at a low liquid fraction and the liquid is situated in the form of isolated droplets in four-grain junctions.*

A certain liquid fraction above zero is necessary to establish a fully connected liquid network. This is a function of the wetting angle: the higher the wetting angle, the higher the threshold for connectivity.

Based on the consideration above, four main areas of liquid distribution in a three dimensional system can be distinguished (Bulau et al. 1979) (Fig. 2.4):

1. At a wetting angle of  $0^\circ$ , liquid could theoretically spread between all grain boundaries, since  $\cos \theta \geq 2\cos \theta_i$ . A polycrystalline aggregate would thereby lose its cohesion even if a very small amount of liquid is added (see below).
2. At wetting angles above  $0^\circ$  and below  $60^\circ$  (for  $2 < \cos \theta / \cos \theta_i < \sqrt{3}$  from equation (2.3)) the liquid spreads along all three- and four-grain junctions, so that a fully connected network is formed regardless of liquid fraction. This was confirmed for non-ideal natural systems, such as quartz plus melt (Laporte et al. 1997).
3. At a wetting angle of  $60^\circ \leq \theta_{eq} < 70,53^\circ$ , the liquid is thermodynamically stable at the four-grain interfaces, where the solid-liquid curvature is negative. However, at a low liquid fraction no connected liquid network is formed.
4. At  $\theta_{eq} \geq 70,53^\circ$  the solid-liquid interfacial curvature is always positive, the liquid is thermodynamically unstable even in four-grain junctions, the highest energy sites. The liquid strives to segregate out of the system if that is possible, and thereby reduces porosity of the aggregate (sintering).

The effect of a wetting angle of  $0^\circ$  ( $\cos \theta / \cos \theta_i \geq 2$ ) on the distribution of liquid is interpreted controversially in the literature. Bulau et al. (1979) argue that, although theoretically fully wetted two-grain boundaries are thermodynamically stable, the requirement of a constant mean curvature is violated for a polycrystalline system with a low melt fraction. According to them, the liquid between the flat grain boundaries ( $k_{mean} = 0$ ) will always migrate into three-grain tubes or four-grain junctions because of their negative mean curvature so that the grain boundaries remain dry, as long as there is only a limited amount of liquid available. The line of evidence is similar to the considerations that lead to predict unstable three-grain tubes at  $\theta_{eq} \geq 60^\circ$ . However, nearly all later authors claim that a wetting angle of  $0^\circ$  results in fully wetted grain boundaries without, however, referring to the apparent contradiction to the work of Bulau et al. (1979) (e.g. Kohlstedt, 1992). This problem could possibly be solved with novel methods of numerical simulation that simulate solid-liquid systems at the grain-scale (Becker et al., 2003). Von Bargen and Waff (1986) used numerical computation methods to derive the detailed geometry of the liquid network as a function of liquid fraction and wetting angle.

### 2.3.3 Liquid connectivity at $\theta > 60^\circ$

At wetting angles above  $60^\circ$ , a connected liquid network only forms above liquid fractions where the initially isolated liquid-filled four-grain junctions get in contact with each other (von Bargen and Waff, 1986) (Fig. 2.5). This represents exactly the amount of liquid above which the laws of constant wetting angle and constant mean curvature can be fulfilled in an ideal system with a constant grain-size. There are two possible solutions for the constant curvature, depending on the liquid development in the aggregate (von Bargen and Waff, 1986). If the liquid fraction in an already connected liquid network is lowered, the pinch off boundary at which the network breaks down is lower than the connection boundary, at which an aggregate forms the liquid network if the liquid fraction is raised (Fig. 2.5). Above this liquid fraction, liquid migration at the grain-scale is theoretically possible. Liquid connectivity starts with a value of  $< 1\%$  at  $\theta_{eq} = 60^\circ$  and rises to about  $4\%$  at  $\theta_{eq} = 75^\circ$ . A high wetting angle liquid with a liquid fraction above the threshold could therefore segregate out of the system by porous flow until the liquid fraction drops below the threshold. Note that strictly speaking such a network is only stable at a wetting angle  $< 70,53^\circ$ . Above this wetting angle, the rule of constant curvature does not apply, i.e. although a network can be geometrically constructed, it is not stable because of a positive solid-liquid curvature (see Section 2.3.1). Although most silicate-melt systems have a wetting angle below  $60^\circ$  (Laporte et al. 1997, and references therein), the connection threshold is considered to be important for many grain-scale processes involving liquid with a potentially high wetting angle. Examples are fluid-flow, diffusion and metamorphic reactions in  $\text{CO}_2$ -rich environments and large-scale

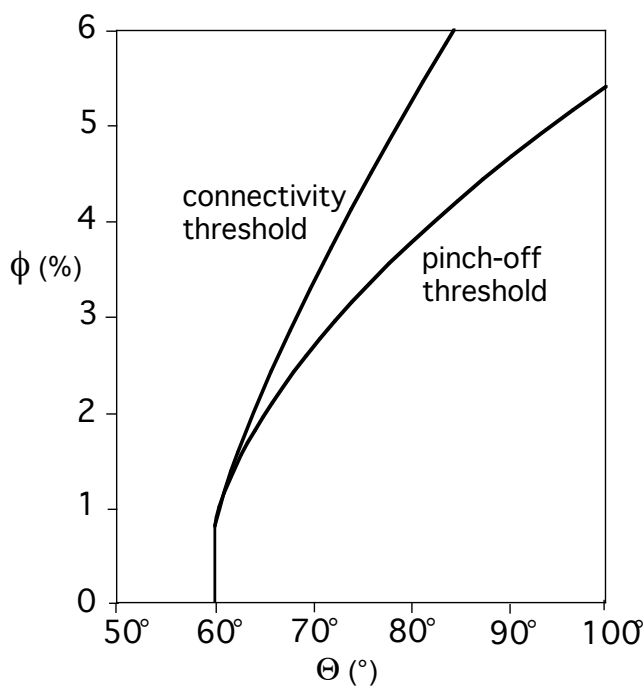


**Fig. 2.5.** Required melt fractions for a three dimensional liquid network in a solid-liquid aggregate with a wetting angle  $>60^\circ$ . The connectivity threshold is the amount of liquid above which a network is formed from originally unconnected pores. The pinch-off threshold is the liquid fraction below which a network breaks down. Redrawn from von Bargen and Waff (1986).

percolation of sulphidic and metallic melt through a solid silicate matrix, that possibly occurred during the early differentiation of the Earth (Laporte and Provost, 2000a, and references therein). It should be noted, however, that the equilibrium approach is especially questionable for complex processes such as liquid migration, since the hydraulic head along which liquid migrates is itself in contradiction with the required equilibrium for the quantitative simulations, so that the grain-scale liquid distribution might be significantly altered (see Section 7.4) (Waff, 1980, Obata and Takazawa, 2004, Bons et al., in prep.).

### 2.3.4 The equilibrium melt fraction (EMF)

For isotropic grains with a solid-liquid wetting angle above  $0^\circ$  suspended in a liquid it is thermodynamically favourable to form dry grain boundaries with their neighbours, thereby establishing the equilibrium wetting angle at their sides (Fig. 2.1d) (Stephensen and White, 1967). The higher the wetting angle, the larger the welding to grain size ratio so that a polycrystalline aggregate with equal sized grains strives towards a certain “ideal” porosity which minimizes the total surface energy of the system. This is called the equilibrium melt (or liquid) fraction (EMF) and is a function of the wetting angle (Fig. 2.6) (Jurewicz and Watson, 1985). If the initial liquid fraction is higher than the EMF, liquid is expelled from the matrix, this is called sintering in the material sciences, if it is lower and a liquid reservoir is available, liquid is drawn into the aggregate (Stephensen and White, 1967, Jurewicz and Watson, 1985). For example, the EMF for a wetting angle of  $0^\circ$  is ca. 26 vol.% in a face centred cubic packing, which is the porosity of the closest sphere packing. The spheres just touch, therefore having a welding to grain radius of one and forming the wetting angle of  $0^\circ$  at their sides. In three dimensional systems the EMF of 0 vol.% is reached at a wetting angle of  $70,53^\circ$ , which is just the angle at which the boundary curvature switches from concave to convex, i.e. the liquid changes from underpressure to overpressure and therefore segregates itself (Section 2.3.2). Both compaction and expansion of the aggregate are driven by surface energy without applied external stress. The EMF

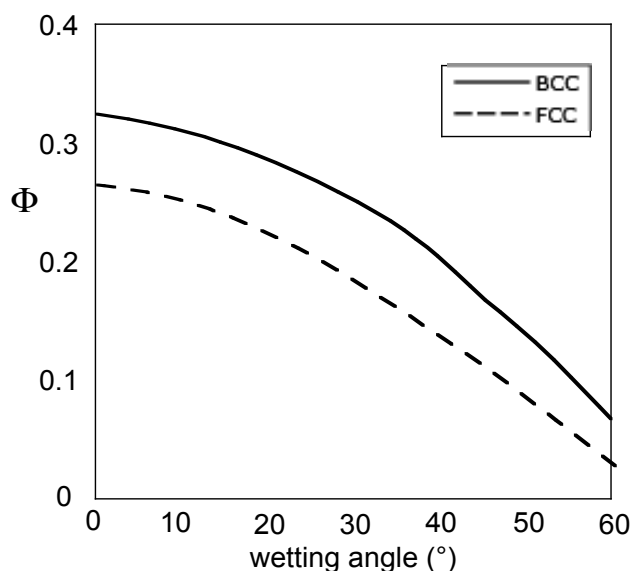


**Fig. 2.6.** The equilibrium melt fraction as a function of the wetting angle for a face centred cubic packing (FCC) and body centred cubic packing (BCC) of the grains. Redrawn from Jurewicz and Watson (1985).

concept has occasionally been proposed as a melt segregation mechanism during (slow) progressive melting either out of the system or into large multi-grain melt pools with high wetting angles close to  $60^\circ$  (Jurewicz and Watson, 1985). However, since the EMF is based on the concept of the ideal system, quantitative predictions from the EMF function should be taken with care. For example, Faul (2000) points out that a liquid-filled three-grain tube that is bordered by crystal facets of non-isotropic crystals is not confined to a certain ideal diameter, because the crystal facets have a local curvature of zero, which is independent of tube width.

## 2.4 Recrystallization and Ostwald ripening

Rocks as complex polycrystalline systems are always striving towards a configuration of minimum Gibb's free energy. In addition to the reorientation of the solid-solid and solid-liquid boundaries and the adjustment of dihedral (wetting) angles that was treated in the preceding Sections, the reduction of surface energy is achieved by recrystallization, if the grains of a system are in contact with each other and the system contains no or only a limited amount of liquid, or Ostwald ripening, if the grains are diluted in a liquid phase with no or little dry grain to grain contacts. Some authors apply the term Ostwald ripening to all grain coarsening processes that involve a liquid phase (e.g. Renner et al., 2002). Although the driving mechanism and theoretical coarsening functions for recrystallisation are similar (compare (2.23) with (2.26)), the consequences and application of both processes are different. Recrystallisation is very important for the distribution and behaviour of a low fraction of melt or fluid for example in the mantle as will be shown in Chapter 3 and 4, while high liquid-fraction Ostwald ripening is thought to be important for the development of large phenocrysts e.g. in a magma chamber (e.g. Higgins, 1999). It seems therefore appropriate to distinguish between low liquid-fraction (liquid-assisted) recrystallization with a high proportion of dry grain boundaries, and high liquid-fraction Ostwald ripening with no or only a limited number of dry grain boundaries throughout this work.

### 2.4.1 *Surface energy driven recrystallisation of polycrystalline aggregates*

Recrystallization can be driven by chemical reactions, i.e. metamorphism and the growth of new minerals (porphyroblasts), by stored elastic or strain energy (e.g. in the form of crystal defects), and by reduction of the total surface area of the system. This process has been called static recrystallization, grain growth (e.g. Urai et al., 1986), or grain boundary area reduction (GBAR, Passchier and Trow, 1996). Because GBAR occurs also in dynamic systems, static recrystallization or static grain growth can be viewed as a special case of GBAR (Passchier

and Trow, 1996). Although the first two driving processes are often dominating during deformation or changing PT conditions (Urai et al., 1986), GBAR recrystallization is the only process that always occurs in any system consisting of more than one crystal (McCrone, 1949, Smith, 1964, Weaire and Rivier, 1984, Anderson, 1988, Karato, 1989) (one hypothetical exception is a two-dimensional system with equal sized crystals, which forms a metastable hexagonal grid). GBAR recrystallization is therefore a potentially important mechanism acting in an ideal system with isotropic surface energy, which was considered above for the equilibrium liquid distribution. Static grain growth can be further divided into normal and abnormal grain growth. Abnormal grain growth is characterized by large grains that grow by sweeping over smaller matrix grains and is not treated here (see e.g. Evans et al., 2001). Normal grain growth is characterized by an increase of the average grain size, while the grain-size distribution remains similar in time (Atkinson, 1988). The surface tension acts to straighten up the grain boundaries while at the same time maintaining regular 120° angles at three-grain junctions (in a dry aggregate), or regular symmetric triangular or tetrahedral liquid pools in liquid-bearing systems (see Section 2.1-2.2). This leads to an ongoing grain coarsening which results in a "foam texture": Large, many-sided grains display outwardly concave grain boundaries and grow, while small, few-sided grains with outwardly convex grain boundaries shrink and finally disappear. This process leads to a continuously increasing mean grain-size. Results of experiments with statically recrystallizing aggregates have shown that the mean grain size can commonly be described by the equation (Atkinson, 1988, Evans et al., 2001)

$$|A|^n - |A|_0^n = k_g t, \quad (2.23)$$

with  $|A|_0^n$  and  $|A|^n$  as the mean grain area at the beginning and at time  $t$  of the experiment, respectively, and  $k_g$  as a temperature and material dependent parameter. However, this equation depends on the starting grain area  $|A|_0$  as a parameter, which is unfavourable if a general grain growth function for the investigated material is required (Bons et al., 2001). If it is assumed by theoretical considerations, that the mean area at normal grain growth obeys a power law function, experimental results can be expressed by the equation

$$|A| = k * t_0^G. \quad (2.24)$$

$k$  is a material and temperature dependent parameter,  $t_0$  is composed of the time elapsed from the start of the experiment plus a hypothetical time at which the mean grain size was zero:

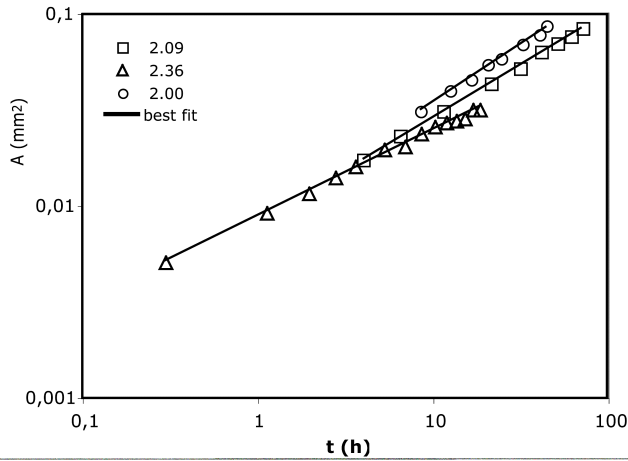


**Fig. 2.7.** Development of the mean area versus time in three statically recrystallizing aggregates.  $t_0$  was determined iteratively to form a straight line in the log-log plot.

$$t_0 = t_{\text{experiment}} + t_{\text{hypothetic}} \quad (2.25)$$

Since experiments start with a finite grain size greater zero, the time elapsed since  $t_0$  can be found by iteratively changing  $t_{\text{hypothetic}}$  to get a best least square fit to equation (2.24) with an  $R^2$  value closest to one (Bons et al., 2001). The exponent of equation (2.24) for ideally recrystallizing aggregates should be 1, i.e. the mean grain area should increase linearly with time. This has been confirmed by numerical modelling of surface energy driven grain growth in two-dimensions (Bons, 1993). In experiments, however, an exponent  $<1$  is usually detected (Glazier and Stavans, 1989), which is attributed to pinning by small amounts of a second solid or liquid phase (Evans et al. 2001). Recrystallization of a liquid-bearing aggregate is complicated by the introduction of new parameters, the liquid-fraction, wetting angle, dissolution-precipitation kinetics and diffusivity of dissolved matter through the liquid. Experiments showed that a low fraction of a wetting liquid phase significantly enhanced the recrystallization rate, while a higher liquid fraction reduces the recrystallization rate again (Renner et al., 2002). Similar observations were qualitatively made during the norcamphor-ethanol analogue experiments that were performed during this study: high liquid fraction (Ostwald ripening see Section 2.4.2) lead to a slow increase in mean grain size, low liquid fraction lead to fast increase in mean grain size. Fig. 2.7 shows the results of three norcamphor-ethanol *in-situ* grain-growth experiments in a log time versus log grain size plot. The sample formed a pseudo 2-D aggregate with a layer of one grain thickness with dispersed ethanol liquid (refer to Chapter 3 for experimental details and sample preparation). The results were iteratively fitted to equation (2.24) to form a straight line in log-log space as described, and are summarized in table 2.1. The resulting functions of the experiments are consistent with similar  $k$  values and exponents ranging from ca. 0.45 to 0.6. The differences in the growth functions could possibly be attributed to the different liquid fractions of the experiments as indicated above. However, although the lowest liquid-fraction experiment (No. 2.00 with 3.6 vol.%) has the highest exponent, the lowest exponent is found with the

intermediate liquid fraction (No. 2.36 with 5.8 vol.%). Since the experimental parameters in all three experiments were similar, and no disturbing factors such as pinning could be observed in the experiments, it is not clear why this is the case. More systematic studies of static grain growth are necessary to include the liquid fraction as a parameter in the norcamphor-ethanol grain growth function and to minimize potential sources of error such as friction or pinning to the grains at the glass slides. However, the exponents around 0.5 can possibly be explained by the behaviour of the liquid in these experiments. Although the grain boundaries are dry at their contacts, between the boundary and the lower and upper glass slide there is a small liquid-filled channel so that liquid is distributed between the liquid-filled triple junctions and the grain boundaries. Grain growth reduces the total length of solid-solid grain boundaries, so that the liquid fraction in the triple junction (or the disequilibrium features, see Chapter 4) increases, even if the total liquid fraction remains constant. The solid-liquid to solid-solid boundary ratio therefore slowly increases during an experiment. By assuming that the dissolution-diffusion-precipitation process of solid through a liquid patch is slower than the migration of a dry grain boundary (e.g. Renner et al., 2002), the exponent  $<1$  can be understood.

No.	$ A _{\text{start}}$ [mm <sup>2</sup> ]	$ A _{\text{end}}$ [mm <sup>2</sup> ]	$\square$ [%]	Function	R <sup>2</sup>	T (°C)
2.36	0.005	0.031	5.8	$ A  = 0.0087 * t_0^{0.448}$	0.997	25
2.09	0.0173	0.084	8.6	$ A  = 0.0083 * t_0^{0.5407}$	0.9993	25
2.00	0.031	0.086	3.6	$ A  = 0.0086 * t_0^{0.6026}$	0.9967	25

**Table 2.1.** Results of three grain coarsening experiments with norcamphor plus saturated ethanol liquid. The results were iteratively fitted to equation (2.24). See text and Section 3.1 for experimental details.

#### 2.4.2 Ostwald ripening

For grains of the same phase that are dispersed in a fluid or melt the same general considerations apply as for a dry polycrystalline system. The system reduces its total interfacial energy by reducing its total surface area. The driving mechanism can be understood by considering the dependence of chemical potential on the solid-liquid curvature (equation (2.23), Chapter 2.2.2). Small (ideally spherical) grains have a higher curvature and therefore a higher chemical potential than large grains. The difference in chemical potential drives dissolution of small grains and growth of the larger grains, so that the number of grains per volume liquid decreases and the mean grain size increases. This increase in mean grain size is called Ostwald ripening after the chemist Ostwald who first described this process (Ostwald, 1901). Since Ostwald ripening involves dissolution, diffusion through the liquid phase and precipitation, it can be either limited by the diffusion rate or the reaction rate of the

system. Theoretical studies resulted in the LSW model (Lifshitz and Slyozov, 1961) that predicted a stationary grain size distribution, and a growth function similar to equation (26)

$$ld^n - ld_0^n = k_p t, \quad (2.26)$$

$ld_0^n$  is the mean diameter at the beginning of the experiment,  $ld^n$  is the mean grain diameter at time  $t$ , and  $k_p$  is a temperature and diffusivity dependent coefficient. The exponent  $n$  is 2 for reaction controlled Ostwald ripening and 3 for diffusion controlled Ostwald ripening according to the LSW model. The same objections raised against equation (2.23) also apply to (2.26), it would be better to iteratively fit results of Ostwald ripening experiments to equation (2.24) to exclude  $ld_0$  as a variable. In this study no systematic investigation of Ostwald ripening was performed in high-liquid-fraction norcamphor-ethanol aggregates. However, qualitative observations showed that the increase in mean grain size is much smaller than during low-liquid-fraction recrystallization.

Ostwald ripening is considered to be important in geology for the growth of phenocrysts in a magma (e.g. large feldspar crystals in a granite) (e.g. Higgins, 1999). It has also been suggested that the growth and size distribution of porphyroblasts such as garnet is governed by an Ostwald ripening process (Miyazaki, 1991; but see Carlson, 1999).

Distribution and modification of the liquid distribution to minimize surface energy at a given mean grain-size (Section 2.1 to 2.3), and the reduction of total surface energy by grain growth and Ostwald ripening (Section 2.4) are the two most important processes that occur in static, high-temperature solid-liquid systems. In this Chapter the theoretical foundations of both processes were treated as if they occurred independently from each other. However, before the interplay between these processes with each other (Chapter 4 and 5) and with other processes such as deformation (Chapter 6 and 7) can be investigated, the analogue experiments and the analogue systems of this study have to be introduced. This is done in the next Chapter. These systems are the tools that allow to investigation the interplay of these complex processes.



### 3. Sample preparation and experimental setup

Presently, only few experiments have been reported that observed melt- or fluid-bearing analogue systems *in-situ*. The first such experiments were performed by Means and Park (1994) and Park and Means (1996) who used a partially-molten mixture of ammonium thiocyanate, diammonia terathiocyanato cobaltate, and ammonium chloride. Other experiments were performed with norcamphor plus water (Bauer et al., 2000), and with a partially-molten norcamphor–benzamid mixture (Rosenberg and Handy, 2000, 2001). The analogue system of Means and Park (1994) displays a strong surface energy anisotropy and the grains have a distinct crystal morphology with crystal facets in contact with melt. The melt phase and the crystals were easily observable *in-situ*, so that they provided well-suited analogues for a high to moderate melt-fraction systems e.g. for crystal mush in a magma chamber. Bauer et al. (2000) performed mainly deformation experiments with their analogue system. Bauer et al. (2000) reported a wetting angle of 42°, which suggests that the water is easily distributed in the sample. However, in my attempts to use the norcamphor-water system, the water did not disperse well throughout the grain aggregate and wetting angle measurements were not successful. Although simple and pure shear deformation experiments were successful in the norcamphor–benzamid system (Rosenberg and Handy, 2000, 2001), the melt is hard to recognize *in-situ*, so that the experiments had to be cooled down for close examinations of the melt microstructure (Rosenberg, 2003, pers. comm.).

Since the aim of this analogue study is to investigate the influence of different modifying factors such as recrystallization and deformation on the liquid distribution, with a special emphasis on details such as the wetting angle, the analogue solid-liquid systems above were not suitable. Three new analogue systems were therefore tested and used for the experiments of this study: norcamphor plus saturated ethanol liquid, norcamphor plus partially molten paraffin wax, and partially molten  $\text{KNO}_3\text{--LiNO}_3$ . Norcamphor–ethanol is a well constraint system that comes very close to the “ideal” solid-liquid system of Chapter 2 (see below) and the nitrate system was mainly used as a second analogue system for comparison.

#### 3.1 Norcamphor experiments

##### 3.1.1 *Norcamphor – ethanol*

Norcamphor ( $\text{C}_7\text{H}_{10}\text{O}$ ) is an organic crystalline compound with a hexagonal symmetry that is ideally suited for *in-situ* analogue experiments (Bons, 1993, Bons et al. 1993, Bauer et al. 2000, Herwegh and Handy, 1996, Rosenberg and Handy, 2000, 2001, Walte et al., 2003). Norcamphor belongs to a group that has been called “plastic crystals”, since the molecules

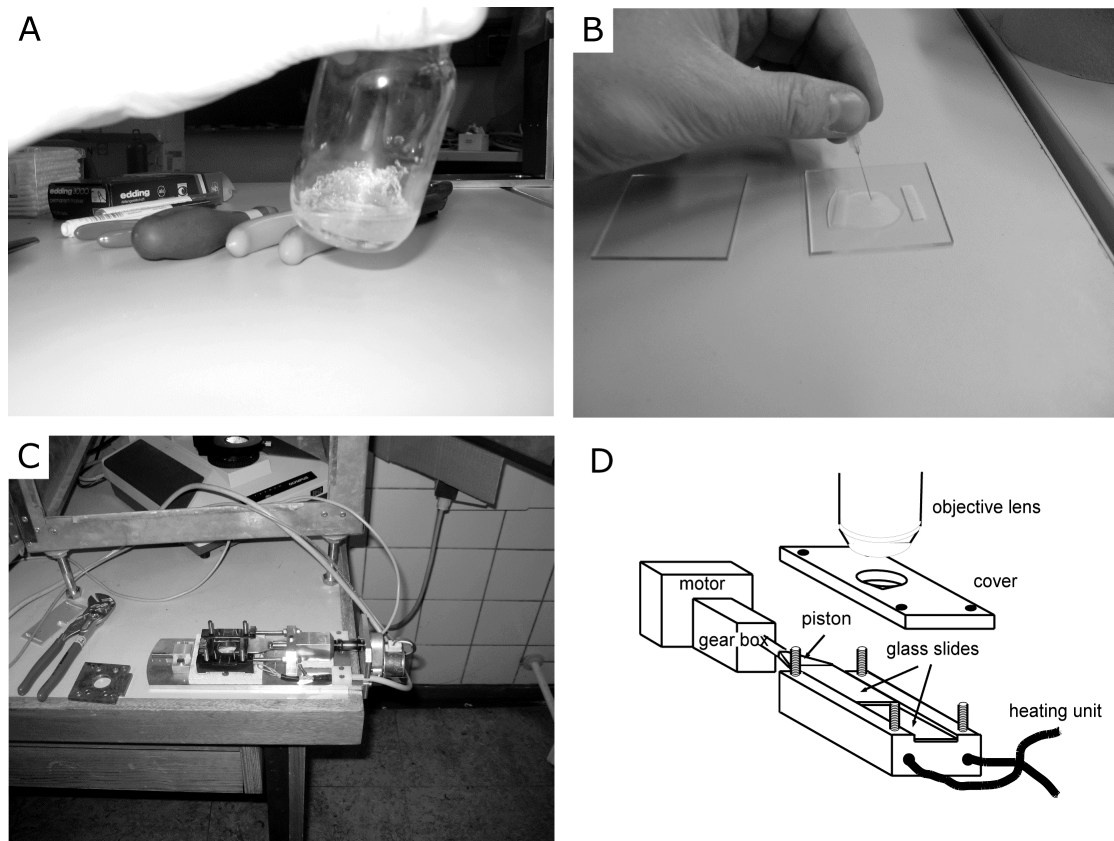


**Fig. 3.1.** **A.** Preparation of ethanol that is saturated with norcamphor. **B.** Sample preparation. Saturated ethanol is placed on a glass slide and stirred until the right amount of norcamphor grains has precipitated. This procedure also reduced the amount of air bubbles. **C.** The Urai-Means shear apparatus for the deformation experiments. The length is ca. 28 cm. **D.** Schematic presentation of the shear rig, redrawn after Passchier and Trow (1996).

occupy the positions of a regular crystal lattice, but are only weakly bonded by van der Waals forces so that they can undergo thermal rotations around their positions (Gray and Winsor, 1974, Bons, 1993). The melting temperature of norcamphor is therefore only 93°C (Bons, 1993) and high-temperature processes such as crystal plastic deformation and surface energy driven recrystallization that usually occur at temperatures in excess of 400°C in rock-forming minerals, can be observed at much lower temperatures between 20 and 80°C (Bons, 1993, Herwegh and Handy, 1996). At the same time, many high-temperature deformation features such as undulose extinction and the formation of subgrain boundaries occur in norcamphor in a similar way as observed in rock-forming minerals like quartz (Herwegh and Handy, 1996). Further information about norcamphor and other organic analogue substances can be found in Bons (1993).

To prepare an experiment for static grain growth or deformation with norcamphor plus ethanol liquid, a saturated ethanol-norcamphor solution has to be prepared first. Although norcamphor is not known to be poisonous, it is quite volatile and has a very strong smell, especially when diluted in ethanol. The whole sample preparation process should therefore be

done under a fume hood. Norcamphor is very soluble in ethanol, small amounts of ethanol should therefore slowly be added to a quite large amount of norcamphor grains, until the required amount of solution is formed (Fig. 3.1a). To prepare a sample with an initially regular small grain-size distribution that does not have large grains, the saturated ethanol should be precipitated on a glass slide at room temperature (under a hood), with no added norcamphor crystals and stirred e.g. with a piece of wire (Fig. 3.1b). As the ethanol evaporates during this process, the norcamphor slowly precipitates in the sample. This “stirring and waiting” procedure should be continued for a few minutes, until the sample has the required solid fraction. Getting the right liquid fraction requires some experience, and the liquid fraction has to be measured later with image analysis techniques (NIH image). Now, a second glass slide is placed on top of the sample. 10  $\mu\text{m}$  to 100  $\mu\text{m}$  thick pieces of aluminium foil or cover glass slides can be used as spacers, to set the required thickness of the sample. For deformation experiments, the sample thickness is determined by fixed pistons of cover glass or aluminium with a thickness of ca. 100  $\mu\text{m}$  that were glued to the glass slides. It is very important that the glue has properly dried before it gets in contact with the liquid, since the ethanol slowly reacts with the glue, thereby loosening the pistons. For static experiments, the two glass slides do not have to move relative to each other, so that they can be glued together, e.g. with epoxy glue, again making sure that the sample does not come into contact with the glue until it has dried. This barrier inhibits evaporation of the sample, so that long-term experiments over several weeks are possible.

The deformation experiments were performed with a transparent Urai-Means deformation rig (Urai, 1983, Means, 1989), that allowed *in-situ* observation of the sample during deformation (Fig. 3.1c, d). For these experiments the glass slides have to be mobile relative to each other, so that another way of inhibiting evaporation has to be used. Sealing is a problem in this case, and there is no ideal solution to this problem, yet. For the experiments of this study, a barrier of “Rhodosil Gum”, a silicone putty, was used. The problem is that the silicone putty is soluble in ethanol. If the sample gets into contact with the barrier, the liquid

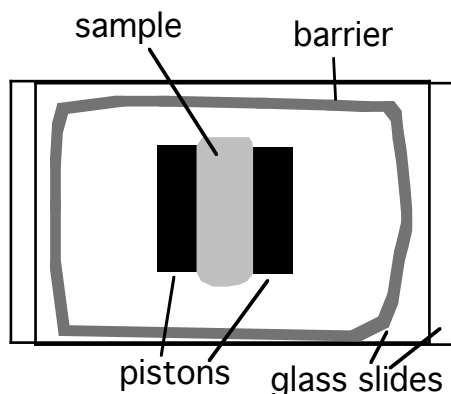


**Fig. 3.2.** Schematic representation of a sample for a norcamphor-ethanol deformation experiment. A 100  $\mu\text{m}$  thick sample is placed between two glass slides. Bulk pure shear deformation is induced by pushing the top over the bottom slide. The barrier of rhodosil gum inhibits evaporation. Width of view is ca. 5 cm.

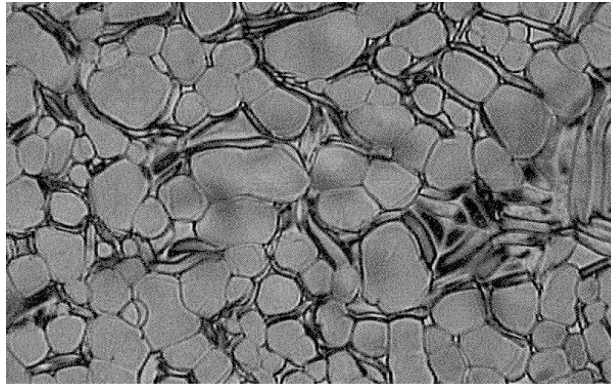


**Fig. 3.3.** Image of a three-phase experiment with norcamphor (round grains)–paraffin crystals (elongate grains)–melt at a temperature of 40°. The wetting angle between norcamphor and wax melt is similar to norcamphor-ethanol ( $\ll 60^\circ$ ).

spreads around the barrier and starts to dissolve it. It is therefore quite important to make sure that the sample is not in contact with the barrier at the beginning of the experiment. The sample was therefore unconfined at its sides during all deformation experiments of this study (Fig. 3.2). In this way deformation experiments of up to 10 days have been performed with only minor evaporation of the sample. Further details on the deformation experiments can be found in Chapter 6.

### **3.1.2 Norcamphor – paraffin wax**

To prepare a norcamphor–paraffin wax sample, the desired mixture is simply heated and completely molten on a hot plate and then placed between glass slides. Norcamphor–paraffin wax appears to form a eutectic system, so that norcamphor–melt, norcamphor–paraffin crystal–melt, and wax–melt experiments are possible. The latter was not investigated in this study. Norcamphor–melt experiments are very similar to norcamphor–ethanol experiments, and they only have to be performed in the deformation rig at raised temperature ( $>50^\circ\text{C}$ ). The recrystallization behaviour and melt distribution is very similar to those of the norcamphor–ethanol experiments even with a similar wetting angle, so that these experiments are not further treated in this study. If three phase (norcamphor–wax crystal–melt) experiments are performed, the temperature has to be lower depending on the softening point of the paraffin wax. A few three-phase experiments were performed at 35–45°C (Fig. 3.3). At these temperatures, grain growth of the norcamphor grains is very sluggish, so that it is advisable to use thin samples (10–20  $\mu\text{m}$ ) and start at a raised temperature in the norcamphor–melt field, so that the norcamphor achieves a reasonable grain size, before cooling down into the three-phase norcamphor–paraffin crystal–melt field.

## **3.2 Nitrate experiments**

The nitrates are a group of ionic crystals with a trigonal crystal symmetry, that have previously been used for analogue experiments by Tungatt and Humphreys (1981), mainly

because  $\text{NaNO}_3$  has the same crystal symmetry as calcite and is therefore a direct analogue for the deformation behaviour of carbonates. Compared to organic crystals such as norcamphor, the nitrates are quite rigid, deformation experiments were therefore performed at elevated temperatures of 150-250°C to observe crystal plastic deformation behaviour (Tungatt and Humphreys, 1981, 1984). For the partially-molten nitrate experiments in this study, the  $\text{KNO}_3$ - $\text{LiNO}_3$  system was favoured, because, in contrast to the  $\text{NaNO}_3$ - $\text{LiNO}_3$  system, it forms a simple eutectic system with an eutectic point at  $134\pm 1^\circ\text{C}$  (Guizani et al., 1998). The melt-fraction of the experiments can be varied by adjusting the temperature and the  $\text{KNO}_3$ - $\text{LiNO}_3$  starting mixture. The desired nitrate mixture (for a partially molten sample ca. 10 wt.%  $\text{LiNO}_3$  was added to 90 wt.%  $\text{KNO}_3$ ) is placed on a hot plate and completely molten at  $>200^\circ\text{C}$  and then quickly cooled e.g. by placing a cold cover glass plate on top. This should be done under a fume hood, since the nitrates might break down at high temperatures, producing poisonous  $\text{NO}_x$  gasses. The sample is placed in the deformation rig and heated to 150-200°C, until the required amount of melt is formed. The partially-molten aggregate is left to anneal for 24-48 hours until the required starting grain size is reached. One problem of the experiments was a temperature gradient between the middle of the observation window of the sample and the heated metal housing of the deformation rig, that was measured to be as high as 15-20°C. Since the solubility of a solid in a liquid generally increases with rising temperature, a melt pocket or a fluid inclusion will always migrate in the direction of the highest temperature, thereby causing segregation between liquid and solid (Leshner and Walker, 1988). This segregation can be observed in Fig. 3.4 and the movies on the enclosed DVD. It was possible to lower the temperature gradient by placing additional glass slides over the observation window in the metal housing. However, the temperature gradient with this experimental setup was still too high to perform static melt-present recrystallization experiments without a significant disturbance of the system. Nitrate deformation experiments on the other hand that took not too much time ( $< 1$  day) were performed quite successfully, despite the gradient. Chapter 6 gives details on these deformation experiments.

The norcamphor-ethanol system was used for most of the experiments that are presented in the following Chapters. The advantages of this system are, that there is no measurable thermal gradient, and an easily observable and a well constrained wetting angle within the range observed in rock forming minerals (ca.  $25^\circ$ , see Chapter 5), which make it ideal for the *in-situ* observation of the grain-scale liquid behaviour. The  $\text{KNO}_3$ - $\text{LiNO}_3$  system was used as a second analogue system for the deformation behaviour of partially molten systems (Chapter 6).

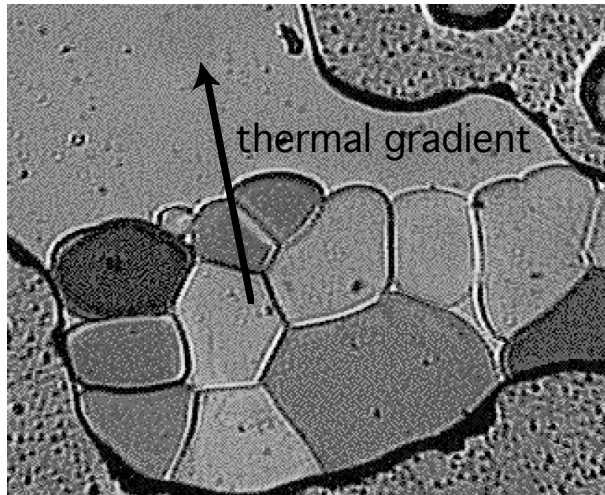


**Fig. 3.4.** Separation between grains and the melt in a thermal gradient of a partially-molten  $\text{KNO}_3\text{-LiNO}_3$  experiment. Because of the higher solubility of the solid at higher temperature, the melt migrates to the hotter side (top of the image) and the solid collects at the colder side (bottom) of the sample. Width of view is 0.4 mm.

## 4. Disequilibrium melt distribution during static recrystallization<sup>1</sup>

### Abstract

Melt migration and segregation, and the rheology of partially molten rocks in the upper mantle and lower crust, strongly depend on the grain-scale distribution of the melt. Current theory for monomineralic aggregates predicts a perfectly regular melt framework, but high-temperature experiments with rock-forming minerals + melt show considerable deviations from this predicted geometry. Disequilibrium features, such as fully wetted grain boundaries and large melt patches, have been described, these were mainly attributed to surface-energy anisotropy of the minerals. We present static analogue experiments with norcamphor + ethanol that allow continuous *in-situ* observation of the evolving liquid distribution. The experiments show that all previously reported disequilibrium features can form during fluid-enhanced static recrystallization when small grains are consumed. There is no need to invoke surface-energy anisotropy, although this might enhance the effect. All disequilibrium features are transitory and evolve back toward equilibrium geometry. However, because the system undergoes continuous static recrystallization, disequilibrium features are always present in a partially molten polycrystalline aggregate and therefore control its properties.

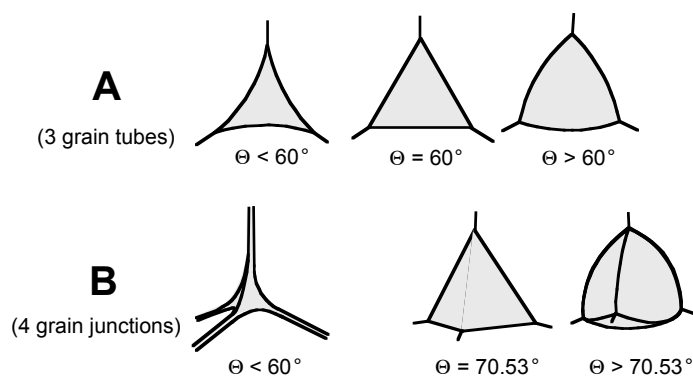
### 4.1 Introduction

Many properties of high-temperature systems that contain small amounts of melt or fluid depend on the liquid distribution at the grain scale. The presence of a three-dimensional melt network in partially molten rocks and its exact geometry determine permeability and therefore migration and segregation rates of melt in porous flow in the lower crust and upper mantle (McKenzie, 1984, von Bargen and Waff, 1986, Kohlstedt, 1992, Faul, 1997, 2001). At low strain rates, the melt-crystal microstructure is considered to be dominated by surface energy forces (McKenzie, 1984, Kohlstedt, 1992). Static experiments can therefore give insight into natural, slowly deforming partially molten rocks. Many theoretical and experimental studies have been performed for relevant geologic systems, more recently there has been an emphasis on the observation and description of nonequilibrium features that could have important consequences for rock properties (Faul, 1997, 2000, Cmíral et al., 1998, Wark et al., 2003).

---

<sup>1</sup> Walte, N.P., Bons, P.D., Passchier, C.W., Koehn, D., 2003. Disequilibrium melt distribution during static recrystallization. *Geology* 31, 1009-1012.

**Fig. 4.1.** Schematic representation of liquid-phase equilibrium geometry. A: Perpendicular to three-grain tubes. B: Four-grain junctions. An interconnected liquid network only forms at  $\theta < 60^\circ$ .



For a monomineralic system of equal-sized grains with an isotropic solid-solid and solid-liquid surface energy ( $\sigma_{SS}$  and  $\sigma_{SL}$ , respectively, Bulau et al., 1979) (Fig. 4.1a), the ratio of  $\sigma_{SS}$  to  $\sigma_{SL}$  determines the dihedral or wetting angle  $\theta$  between two crystals and the liquid by the equation

$$2 \cos(\theta/2) = \sigma_{SS} / \sigma_{SL} . \quad (4.1)$$

Theoretically, if  $\theta$  and the liquid fraction are known, the liquid distribution in this polycrystalline system in thermodynamic equilibrium is fully constrained by the requirement of a constant mean curvature of solid-liquid boundaries (von Bargen and Waff, 1986). Liquid pockets at four-grain junctions are isolated at low-liquid fractions when  $\theta > 60^\circ$  (Fig. 4.1b). When  $\theta < 60^\circ$ , a regular three-dimensional network is predicted, regardless of the liquid fraction, with four-grain liquid pockets that are connected by tubes along three-grain junctions (Fig. 4.1). Boundaries between two grains remain dry as long as  $\theta > 0^\circ$ , i.e.,  $\sigma_{SS} / \sigma_{SL} < 2$  (equation 4.1). This theory does not distinguish between melt and fluid and can therefore be applied to both partially molten and aqueous-fluid-bearing systems in textural equilibrium.

To confirm these theoretical predictions and to find the range of wetting angles for significant geologic systems, high-temperature experiments were performed with major rock-forming minerals such as dunite + mafic or ultramafic melt (Hirth and Kohlstedt, 1995, Faul, 1997, Cmíral et al., 1998) or quartz + felsic melt (Jurewicz and Watson, 1984, Laporte, 1994, Laporte and Watson, 1995). In these experiments,  $\theta$  is generally well below  $60^\circ$  (e.g., Laporte and Provost, 2000), and the liquid should therefore form a regular three-dimensional network of three-grain tubules. However, in experiments apparent disequilibrium features were described that deviated from the predicted regular melt geometry (Fig. 4.2): (1) fully wetted grain boundaries, (2) trapped melt lenses between grains, (3) strongly distorted, melt-filled triple junctions, (4) dry triple junctions, (5) large, multigrain-bounded, melt pools. It has been recognized that variety in grain size and crystal lattice-controlled surface-energy anisotropy modifies the actual liquid distribution in natural aggregates (e.g., Waff and Faul,

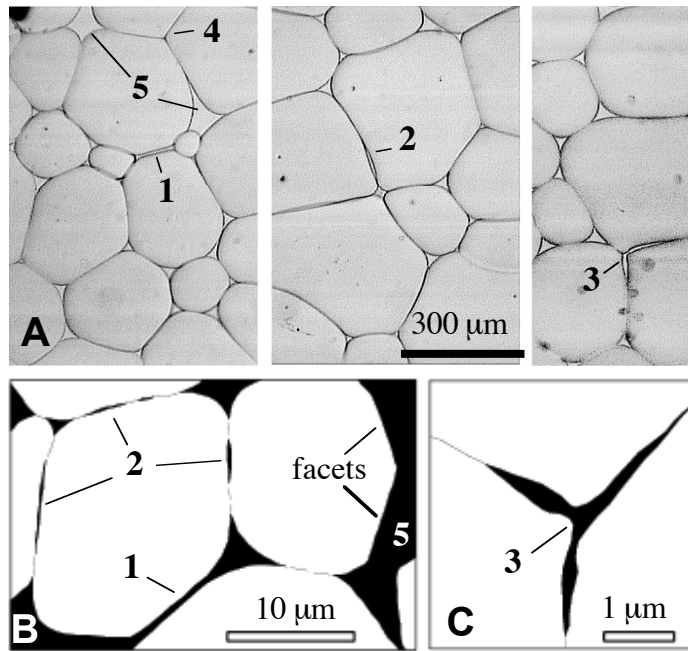


**Fig. 4.2.** Summary of disequilibrium features in a thin sheet of polycrystalline norcamphor with norcamphor-saturated ethanol. I—fully wetted grain boundaries; II—trapped liquid lenses; III—distorted triple junctions; IV—dry triple junctions; V—large liquid patches. See text for experimental details. Width of view is 2 mm. See also movie 2.05-3 on the enclosed DVD.

1992, Laporte and Watson, 1995, Jung and Waff, 1998, Wark et al., 2003). The frequent observation of straight crystal facets of grains in contact with melt supports the latter explanation for nonequilibrium melt geometries (Waff and Faul, 1992, Hirth and Kohlstedt, 1995, Jung and Waff, 1998, Faul, 1997, Laporte and Provost, 2000). However, features like melt lenses (2) and distorted triple junctions (3) can neither be explained by anisotropy nor by grain-size variations. For example, the lattice orientation next to a melt lens (2) or a distorted triple junction (3) has to be the same as the lattice orientation next to the dry part of the same grain boundary, therefore, either a fully wetted or a dry grain boundary should be favoured, not a melt lens. Although quartz is considered to be more isotropic than olivine, nonequilibrium features 1-5 were observed in quartz + melt systems as well (e.g., Laporte, 1994, Laporte and Provost, 2000).

Nonequigranular grain aggregates in nature are never in static textural equilibrium because of ongoing grain growth (i.e., static grain growth) driven by reduction of surface energy (Wearie and Rivier, 1984, Anderson, 1988). How much does this textural nonequilibrium influence melt distribution in natural systems? In order to answer this question we used static *in-situ* analogue experiments of a solid-liquid system. We continuously monitored the textural evolution of the solid-liquid system in order to shed light on the distribution and evolution of disequilibrium structures.

## 4.2 Experiments

The system norcamphor + ethanol was used to study the development of solid-liquid systems. Norcamphor is a hexagonal organic crystalline compound that exhibits crystal plastic

behaviour, analogous to minerals such as quartz, at room temperature (Bons, 1992, Herweg and Handy, 1996). We wedged 20–150- $\mu$ m-thick samples of norcamphor + norcamphor-saturated ethanol between glass plates. The assembly was placed on a microscope stage and photographed in regular intervals of 5–60 min. At room temperature the aggregate forms a two-dimensional foam texture with smoothly curved grain boundaries between the crystals (Fig. 4.2a).

The ethanol liquid, which is the melt analogue, is dispersed within the sample, mainly at regular equal-sized triple junctions with concave walls. The solid-liquid wetting angle is  $\sim 10^\circ$ – $15^\circ$ , and the fluid fraction in our experiments ranges between 2% and 8%, remaining constant during an experiment. Norcamphor crystals in contact with liquid show no crystal facets and are therefore considered to have an effectively isotropic  $\sigma_{SL}$ . Varying sample thickness had only minor influence on the microstructural evolution, we therefore conclude that the effect of the glass slides on our results is negligible.

The norcamphor + ethanol aggregate approaches the ideal two-phase model system of an isotropic crystal phase containing a well-wetting ( $\theta < 60^\circ$ ) fluid or melt phase. The absence of a crystal lattice-controlled anisotropy helps to keep the system simple so that the results are directly comparable to the predictions from equilibrium-based theory. The advantage of using fluid in the experiments, as opposed to using a melt phase, is that all experiments can be performed at room temperature (25 °C) held constant within 1 °C by air conditioning without additional heating. This approach avoids temperature gradients, which can have a strong effect on liquid distribution (Leshner and Walker, 1988). Although a few similar *in-situ* analogue studies involving partial melt or fluid have been performed (Park and Means, 1996, Bauer et al., 2000, Rosenberg and Handy, 2000), no previous experiment was specifically concerned with the effect of static grain growth on melt distribution.

### 4.3 Results

The norcamphor + ethanol aggregate coarsens by static grain growth, in which large, many-sided grains grow at the expense of small, few-sided grains. In areas of the aggregate where the local grain size is quite uniform, the liquid is distributed as predicted by the equilibrium theory (e.g., Figs. 4.2a, 4.3a). However, when neighbour switches occur or small grains disappear, the temporary high curvature of grain boundaries leads to an accelerated grain-boundary velocity, which creates a temporarily distorted liquid distribution. All previously described disequilibrium features (1-5, Fig. 4.2) are formed in our experiments because of these processes (Figs. 4.3–4.6). The experiments show that the features are transitory: a fully wetted grain boundary (1) forms because of a neighbour switch that is finally transformed

into a trapped melt lens (2) as the remaining grains merge (Fig. 4.3). Dry or distorted triple junctions (3, 4) form when a smaller, three- or four-sided grain disappears from between the surrounding grains (Figs. 4.4, 4.5). Large fluid patches (5) normally emerge when previous neighbour switches lead grains to disconnect from the surrounding grains and finally dissolve (Fig. 4.6). None of these features are stable, they revert back toward liquid equilibrium geometry once the small grains have disappeared (Figs. 4.3e, 4.4e, 4.5e).

Our results show that even in this simple static system, continuous *in-situ* observation is

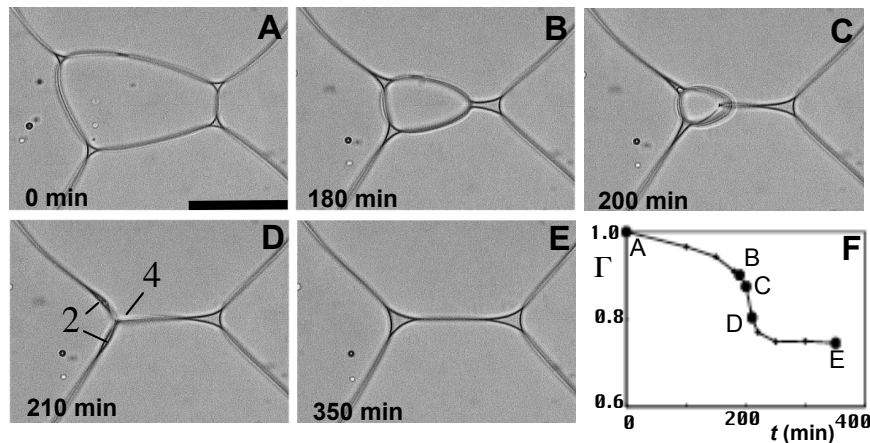


**Fig. 4.3.** A: Central norcamphor grain surrounded by regular, approximately equal-sized triple junctions. B–D: After a neighbour switch (in B), the merged fluid patch is pulled into a strongly elongate shape by the dissolving central grain (in C) until that grain disappears (in D). Initial triple junctions now form a strongly distorted cross shape. E: Relaxation of system toward an “equilibrium” fluid distribution. Note remaining fluid lens. F: Normalized total surface energy  $\square_{\text{total}}$  vs. time  $t$  plot. Dots represent conditions in images B–E. Length of scale bar represents 200  $\square\text{m}$ . See also movie 2.32-5 on the enclosed DVD.

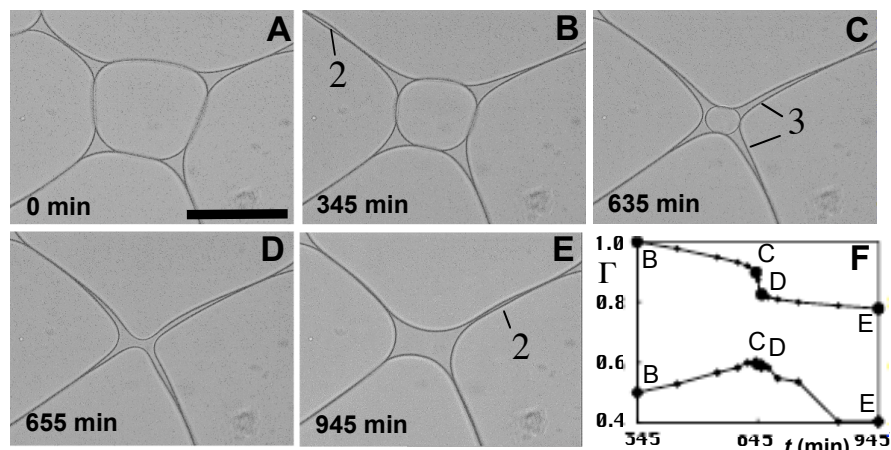


**Fig. 4.4.** A–C: A four-sided grain is shrinking. After 3 h, a neighbour switch occurs, and resulting three-sided grain disappears after 3.5 hours. D: Melt-filled triple junctions become elongated and turn into a lenticular shape when grain disappears. Notice that for a short time, result is a dry triple junction (IV) with two trapped melt lenses (II) nearby. E: Lenses merge and finally form an equilibrium melt triangle. F: Normalized  $\square_{\text{total}}$  vs. time  $t$  plot. Large dots represent conditions in images A–E. Length of scale bar represents 100  $\square\text{m}$ . See also movie 2.32-6+7 on the enclosed DVD.

essential to understand the complicated time-dependent processes. Snapshots at any time step, as in high-temperature experiments, would not have revealed the ongoing process but would instead have recorded the disequilibrium features shown in Fig. 4.2.

In order to understand what drives the fluid distribution first out of long-term equilibrium and afterward back toward equilibrium during and after the disappearance of a grain, the local surface energy for the grains in Figures 4.3–4.6 was calculated as a function of time. The lengths of solid-solid and solid-liquid boundaries were directly measured from the pictures,  $\Gamma_{\text{S}}$  per unit length was set to unity, and  $\Gamma_{\text{SL}}$  was calculated from equation 1, yielding  $\Gamma_{\text{SL}} = 0.5043$  per unit length for  $\theta = 15^\circ$ . The total solid-solid + solid-liquid surface energy  $\Gamma_{\text{total}}$  was normalized to the starting image to track the relative change in time.

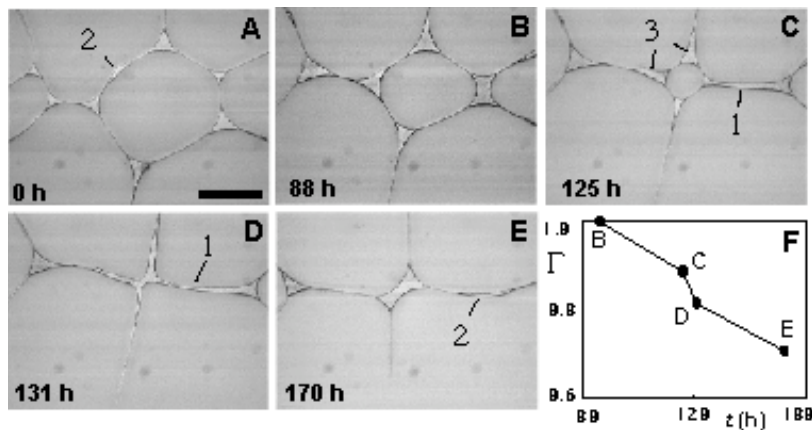


**Fig. 4.5.** A–C: Disappearance of a four-sided grain. D: Melt-filled triple junctions become a four-grain junction. Notice very low apparent wetting angle (C–D) that evolves during experiment. E: A fluid lens is left even some time after relaxation of system. F: Normalized  $\Gamma_{\text{total}}$  vs. time  $t$  plot (upper curve);  $\Gamma_{\text{S-L}}$  vs. time  $t$  plot is given for comparison (lower curve). Large dots represent conditions in images (B–E). Length of scale bar represents 100  $\mu\text{m}$ . See also movie 2.07 on the enclosed DVD.

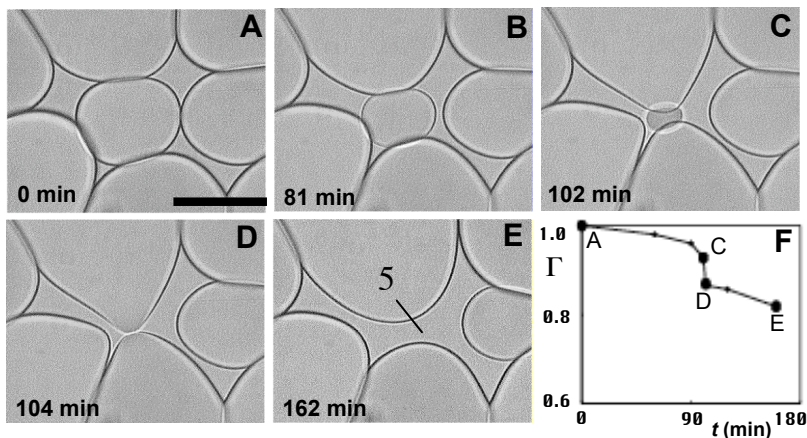


**Fig. 4.6.** Formation of a large liquid patch. A–E: Disappearance of central grain (A–D) leaves a large fluid patch bordered by several grains (E). Notice solid-solid grain boundary (D) that develops after disappearance of central grain and that is separated shortly afterward. F: Normalized  $\Gamma_{\text{total}}$  vs. time  $t$  plot. Large dots represent conditions in images A and C–E. Length of scale bar represents 50  $\mu\text{m}$ . See also movie 2.32-3 on the enclosed DVD.

The resulting energy vs. time plots show a uniform surface-energy development (Figs. 4.3f, 4.4f, 4.5f, 4.6f). Initially,  $\Delta_{\text{total}}$  decreases slowly, then drops very fast during the collapse of the grain. After the grain has disappeared, the surface energy decreases slowly again. The solid-liquid energy ( $\Delta_{\text{SL}}$ ) is plotted in Figure 4.5f for comparison. Although  $\Delta_{\text{SL}}$  rises because of the formation of a disequilibrium feature (Fig. 4.5f), the  $\Delta_{\text{SS}}$  gain by the disappearing grain is more than enough to compensate for this effect. The formation and stability of disequilibrium features can be summarized in two stages: (1) Collapse of small grains leads to *fast* creation of disequilibrium features owing to a fast drop of  $\Delta_{\text{total}}$ . (2) Solid-liquid surface tension leads to relatively *slow* healing of disequilibrium features owing to a slower  $\Delta_{\text{total}}$  decrease.

The process of grain coarsening is directly connected to the rate of grain disappearance for a polycrystalline aggregate. Disequilibrium features are therefore continuously created and, because of their slower disappearance, the chance of finding them is high. The resulting geometry can be envisioned as a three-dimensional liquid network consisting of regular triple-junction tubes and quadruple junctions of different sizes modified by continuously changing disequilibrium features (Fig. 4.2).

#### 4.4 Discussion

The similarities between the developing features in the norcamphor experiments and the results of high-temperature experiments are striking (Fig. 4.2). Static, surface-energy-driven recrystallization is a process that always occurs at elevated temperatures. In fact, to achieve a “steady state” microstructure with no inherited effects from the starting powder, most authors of high-temperature experiments took great care to ensure that grain coarsening occurred (e.g., Faul, 1997, 2000). We therefore suggest that our results are directly applicable to quartz-felsic melt aggregates because of the low crystal-lattice anisotropy of quartz. Because of the higher anisotropy of olivine and the regular occurrence of crystal facets, the consequences have to be evaluated carefully for this system. Fully wetted grain boundaries are often approximately parallel to low-index crystallographic planes (crystal facets) in olivine + ultramafic melt systems, according to Jung and Waff (1998). However, they also show many curved crystal surfaces, not crystal facets, that look very similar to our experiments (cf. their Fig. 1, p. 901, with our Figs. 4.3 and 4.5). Cmíral et al. (1998) found no preference of low-index crystallographic planes for fully wetted grain boundaries in the dunite + melt system. However, Wark et al. (2003) have pointed out the problem of interpreting the three-dimensional melt geometry from two-dimensional polished Sections. They proposed that most apparent disequilibrium features are explained by Sectioning

through an ideal melt network modified only by nonequal grain size. Although this Sectioning effect might explain some disequilibrium features, the melt lenses (2), distorted triple junctions (3), and large liquid patches (5) with more than four bordering grains are not explained. Note also that our thin-sheet experiments do not have Sectioning effects.

We observe a general increase in liquid fraction that is contained in disequilibrium features with overall increasing liquid fraction, as observed by Waff and Faul (1992), Faul (1997), Hirth and Kohlstedt (1995), and Laporte and Provost (2000). However, this result is not due to the higher chance of cutting a four-grain junction, as proposed by Wark et al. (2003), but is rather explained by a lower mean curvature of solid-liquid junctions for higher liquid fractions and, therefore, weaker capillary forces. Disequilibrium features will be more pronounced and last longer when capillary forces are relatively weak. Relatively high capillary forces oppose the formation and stability of disequilibrium features. Therefore, a regular continuous network due to a high mean curvature of solid-liquid junctions is expected for small liquid fractions. In experiments having higher liquid fractions and smaller mean curvatures, more liquid is pooled in disequilibrium features. The effect of developing crystal facets in olivine experiments is difficult to constrain at this stage, but it could help to stabilize the disequilibrium features such as large melt patches after their initial formation, possibly even at lower liquid fractions.

Two porosity-permeability models for high-temperature liquid-bearing systems have been proposed that lead to strongly contrasting interpretations for general questions of magmatism. The empirical model of Wark and Watson (1998) is based on direct permeability measurements on quartz-fluid aggregates. They report a continuous porosity-permeability function similar to that of von Bargen and Waff (1986), but about one order of magnitude lower in permeability for a given liquid fraction. On the other hand, Faul (1997, 2001) proposed a model based on percolation theory that predicts small liquid fractions (<2%) to be distributed in unconnected lenticular melt pools. If the liquid content is greater than 2%, the melt pools form a network, resulting in a sharp increase in permeability of approximately four orders of magnitude (Faul, 1997). Wark et al. (2003) questioned the assumptions and methods that led to this threshold model and argued that their continuous model is valid for both olivine-melt systems, as well as for quartz-melt systems.

Our results – a liquid network with few disequilibrium features for small liquid fractions and more disequilibrium features for higher liquid fractions – indicate a more “continuous” porosity-permeability function such as the empirical function of Wark and Watson (1998) rather than a threshold function like the model of Faul (1997). If liquid geometry in a given system and therefore the system’s permeability are strongly dependent on grain coarsening, as we suggest, average grain size, temperature, grain-boundary mobility, second phases, and

pinning play an important role in addition to  $\gamma$ , liquid fraction and surface energy anisotropy. Therefore, results of empirical studies have to be considered carefully before they can be applied to nature.

## 4.5 Conclusion

We conclude that nonequilibrium melt distributions in partially molten grain aggregates can be explained with the disappearance of small grains due to grain growth. This process may be coupled with and enhanced by crystal-lattice-controlled surface-energy anisotropy and formation of crystal facets, as described in olivine + melt systems. Our results support a gradual increase in permeability with liquid fraction (Wark and Watson, 1998) rather than an abrupt increase as in threshold models (Faul, 1997). The aim of this paper is to stress the importance of recrystallization as a major factor for the melt or fluid distribution in high-grade geologic systems.



## 5. Evolution and significance of dynamic wetting angles in a polycrystalline solid–liquid system<sup>2</sup>

### Abstract

Melt migration and the rheology of a partially molten rock depend on the grain-scale distribution of the melt, which is controlled by its wetting behaviour. This wetting behaviour is normally modeled using a constant equilibrium wetting angle. However, experiments with norcamphor plus ethanol, analogues for low-anisotropy solid-liquid systems such as quartz or olivine plus melt, reveal the frequent occurrence of dynamically altered wetting angles due to continuous static recrystallization. Our experiments indicate a correlation between the solid–solid-liquid triple junction migration rate and the dynamic wetting angle: a raised dynamic angle opens and wets the adjacent grain boundary, while a lowered angle closes and “dries” the adjacent boundary. In our experiments the junction velocity is an exponential function of the surface tension that acts perpendicular to the boundary of the two involved grains. Our results show that even in isotropic solid-liquid systems, continuous recrystallization results in a broad distribution of wetting angles. Both the mean and median values (22° and 20°) underestimate the actual equilibrium angle of ~25° for norcamphor–ethanol. Therefore, high-temperature experiments that were performed to determine wetting angles based on the assumption of a single-valued true wetting angle should be reconsidered. Mechanical extension or compression of welded grains is also expected to result in dynamically altered wetting angles that eventually lead to either disconnection or further welding of the grains.

*Index terms:* 5112 Physical properties of rocks: Microstructure, 5199 Physical properties of rocks: General and miscellaneous, 3630 Mineralogy and Petrology: Experimental mineralogy and petrology, 8434 Volcanology: Magma migration

### 5.1 Introduction

The presence and influence of melt or aqueous fluids (henceforth termed “liquid”) on high-temperature geologic systems such as the lower crust and the upper mantle is one of the key factors that initiate and control geological processes. Mass transport in liquid-bearing crystalline systems can be achieved by diffusion of dissolved matter in a stationary liquid, by

---

<sup>2</sup> Walte, N.P., Bons, P.D., Passchier, C.W., 2004. Evolution and significance of dynamic wetting angles in a polycrystalline solid–liquid system. *Journal of Geophysical Research*, submitted.

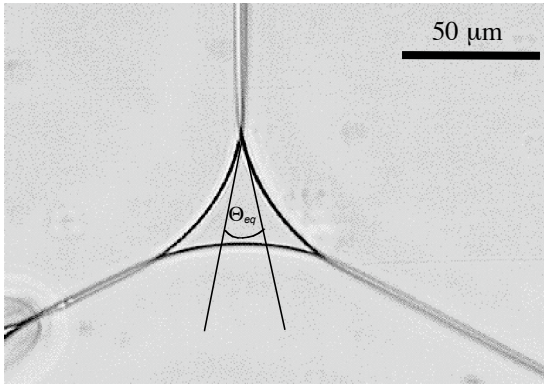


**Fig. 5.1.** Triangular liquid-filled three-grain junction in a semi two-dimensional norcamphor-ethanol analogue sample. Two tangents are drawn on the plane normal to the solid-solid-liquid junction to measure the true wetting angle  $\theta_r$  which is in this case the equilibrium angle  $\theta_{eq}$  of ca.  $25^\circ$ .

liquid advection relative to a solid matrix (percolation), or through ductile flow of the complete solid-liquid system (deformation). Important controlling parameters for all three processes, liquid connectivity, matrix permeability, and two-phase rheology, are functions of the overall liquid fraction (e.g. Arzi, 1978, Vigneresse et al., 1996), and of the grain-scale distribution of the liquid (e.g. Bulau et al., 1979, Jurewicz and Watson, 1985, von Bagen and Waff, 1986, Kohlstedt, 1992, Faul, 1997, Wark and Watson, 1998, Wark et al., 2003, Walte et al., 2003). The most important aspect of the grain-scale liquid distribution is whether a given small liquid fraction is dispersed in the crystalline matrix as isolated pores, in the form of a connected network along grain edges, or in the form of liquid films that fully wet grain boundaries. The main parameter determining this is the dihedral angle or wetting angle ( $\theta$ , Fig. 5.1) between the liquid and two solid grains (Bulau et al., 1979, von Bagen and Waff, 1986). The wetting angle is usually assumed to control the permeability-porosity relationship of a solid-liquid system (von Bagen and Waff, 1986), and is therefore of importance to models of melt flow, especially in the mantle (e.g. McKenzie, 1984, 1987, Wiggins and Spiegelman, 1995, Rabinowicz et al., 2001). Much attention has therefore been given to the determination of the wetting angle in geologically relevant systems (Laporte et al., 1997, and references therein, Holness, 1996, and references therein, Laporte and Provost, 2000, and references therein). Below we give a brief review of the principles of the wetting angle and its determination. We then show, using analogue experiments, that recrystallization is an important, but normally neglected process that modifies the wetting angle distribution. Incorporating the effect of recrystallization will both improve the determination of the equilibrium wetting angle, and the effective wetting angle (range) that determines the relationship between porosity and permeability in geological solid-liquid systems.

### 5.1.1 The equilibrium wetting angle and liquid distribution

The wetting angle in equilibrium ( $\theta_{eq}$ ) is determined by the ratio of the solid-solid ( $\gamma_{ss}$ ) to the solid-liquid surface energy ( $\gamma_{sl}$ ) between the two involved crystals and the liquid. The surface

energy  $\gamma$  can be either expressed as energy per unit surface area ( $\text{J/m}^2$ ), or as the surface tension, being the force per unit length of an interface ( $\text{N/m}$ ). A vector balance between the two solid-liquid surface tensions and the solid-solid surface tension at a solid-liquid triple point (in 2-D, in 3-D the solid-solid-liquid interSection is a line) (Fig. 5.2a) yields the equilibrium wetting angle equation:

$$2\cos\left(\frac{1}{2}\theta_{eq}\right) = \frac{\gamma_{SS}}{\gamma_{SL}}. \quad (5.1)$$

Solid-solid-liquid points at all times strive to move towards positions that satisfy the equilibrium wetting angle, because any other position would cause a non-zero tension on the triple point (Fig. 5.2b). A given solid-liquid system has a single  $\theta_{eq}$  if the solid phase has an isotropic surface energy. In crystalline materials,  $\gamma$  may be a function of the orientation of a boundary relative to the adjacent lattice(s). This would give rise to a range of  $\theta_{eq}$ , and possibly the development of faceted solid-liquid boundaries (Waff and Faul, 1992, Faul, 1997, Cmíral et al., 1998, Jung and Waff, 1998, Laporte, 2000).

An additional restriction for the melt distribution in a polycrystalline system is the dependence of the chemical potential of a solid-liquid surface on its mean curvature (Bulau et al., 1979). In equilibrium, all solid-liquid boundaries should therefore have identical curvatures. Von Bargen and Waff (1986) showed that a single  $\theta_{eq}$  and the requirement of constant curvature fully determine the liquid distribution. At  $\theta_{eq} > 60^\circ$  and a low liquid-fraction, liquid is located at grain vertices, where four boundaries meet (Fig. 5.3). These isolated vertices either have outward-curving surfaces at  $\theta_{eq} > 70.53^\circ$  or inward-curving surfaces at  $\theta_{eq} < 70.53^\circ$  (von Bargen and Waff, 1986). At  $\theta_{eq} < 60^\circ$ , liquid can spread to fully wet grain triple junctions, forming liquid tubules that connect the quadruple junctions. Liquid thus forms a connected, percolating network, allowing advection even at very low liquid

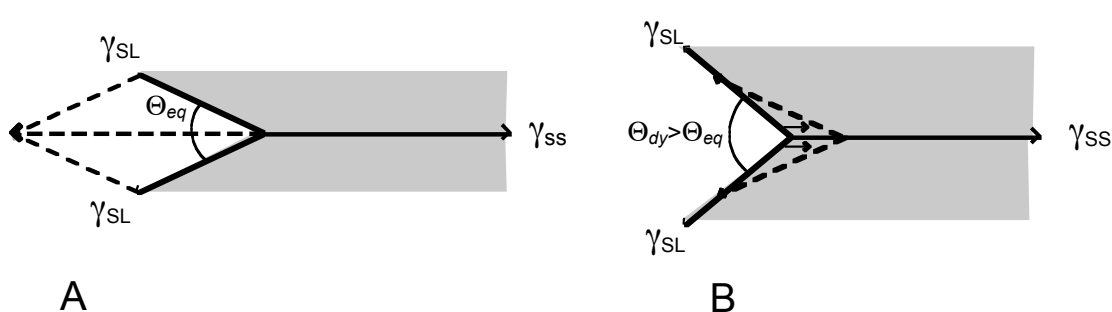


**Fig. 5.2.** Vector balance between the solid-solid ( $\gamma_{SS}$ ) and the solid-liquid ( $\gamma_{SL}$ ) surface tensions. **A:** In equilibrium the two s-l surfaces form the characteristic equilibrium wetting angle  $\theta_{eq}$ . **B:** When the surfaces are shifted, a transient dynamic wetting angle  $\theta_{dy}$  is formed. The resulting force vector will move the triple junction until  $\theta_{eq}$  is reestablished.

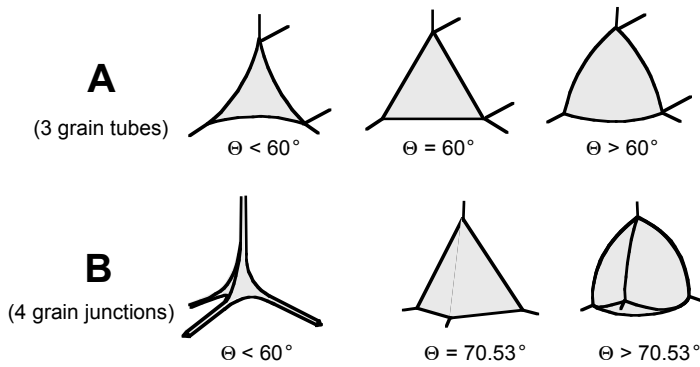


**Fig. 5.3.** Schematic representation of the liquid-phase geometry at equilibrium in an ideal solid-liquid system with no  $\Delta_{\text{ss}}$  anisotropy. **A:** Perpendicular to the three-grain pools. **B:** Geometry of the four-grain tubes. An interconnected liquid network forms at  $\theta_{\text{eq}} < 60^\circ$ . Below  $70.53^\circ$  four-grain junctions are concave outwards, above  $70.53^\circ$  they are convex outwards.

fraction. In perfect thermodynamic equilibrium, the liquid is homogeneously distributed throughout the rock and the liquid network geometry is solely determined by liquid fraction or porosity ( $\Delta$ ) and  $\theta_{\text{eq}}$  (Bulau et al., 1979, von Bargen and Waff, 1986). Based on the equilibrium models for liquid distribution, the permeability ( $k$ ) of partially molten rocks has been related to the porosity by the Blake-Carman-Cozony relation  $k \propto \Delta^n$  with an exponent  $n$  of 2 or higher (Carman, 1956, McKenzie, 1984, Scott and Stevenson, 1986, von Bargen and Waff, 1986, Wark and Watson, 1998, Ghods and Arkani-Hamed, 2000, Wark et al., 2003).

### 5.1.2 Determination of the wetting angle

Because of the fundamental importance of the wetting angle for liquid distribution in geological systems, high-temperature experiments involving common rock-forming minerals and coexisting melts and fluids have been performed to determine the range of wetting angles in nature. The results of different experiments indicate that  $\theta_{\text{eq}}$  is usually well below  $60^\circ$  for the major rock-forming minerals coexisting with melt so that a three-dimensional network is generally expected regardless of melt fraction (Laporte et al., 1997, and references therein, Holness, 1996, and references therein, Laporte and Provost 2000, and references therein). One problem of determining  $\theta_{\text{eq}}$  in high-temperature experiments is the fact that it has to be measured from two-dimensional Sections of an original three-dimensional solid-liquid system. The Sectioning effect means that only "apparent wetting angles" ( $\theta_{\text{ap}}$ ) can be observed, which may over- or under-estimate the "true wetting angles" ( $\theta_{\text{tr}}$ ). The equilibrium angle  $\theta_{\text{eq}}$  is usually considered to be close to the median of the  $\theta_{\text{ap}}$  distribution (e.g Laporte, 1994, Laporte and Provost, 2000, and references therein).

Interestingly, the same high-temperature experiments used to determine equilibrium wetting angles have revealed that the ideal liquid distribution, described above, is never truly reached. Disequilibrium features like large liquid pools, fully wetted grain boundaries or trapped liquid lenses between two-grain boundaries have commonly been reported in experiments (Fig. 5.4) (e.g. Waff and Faul, 1992, Laporte, 1994, Laporte et al., 1997, Faul,

1997, Cmiral et al., 1998, Walte et al., 2003). The disequilibrium features are important since they concentrate a proportion of the total liquid volume, so that less liquid is left to constitute the three-dimensional connected network, thereby reducing permeability. Based on these observations, Faul (1997) proposed an alternative porosity–permeability model for the mantle, which differs significantly from the Blake-Carman-Cozony equilibrium models, and which stresses the importance of a detailed knowledge of the melt network geometry. Three explanations are currently given for the formation of disequilibrium features. Most authors (Kohlstedt, 1992, Waff and Faul, 1992, Faul, 1997, Laporte, 1994, Laporte and Watson, 1995, Jung and Waff, 1998, Cmiral, 1998) explain their occurrence by a non-uniform equilibrium wetting angle in an anisotropic crystal system. The frequent occurrence of crystal facets in experiments, especially with olivine, confirms surface energy anisotropy, but the significance for the melt distribution remains uncertain. Wark et al. (2003) challenge the overall existence of disequilibrium features and explain their “apparent” occurrence by two-dimensional Sectioning effects of the original three-dimensional liquid network. An apparent large melt patch could, for example, be produced by cutting a liquid-filled quadruple grain junction. Wark et al. (2003) therefore favor an equilibrium liquid distribution that is only slightly altered by variable grain sizes in a natural aggregate. However, Walte et al. (2003) demonstrated that the same disequilibrium features develop in 2-dimensional *in-situ* analogue experiments that do not have Sectioning effects. They showed that all previously described disequilibrium features can form as a result of ongoing grain coarsening. For example, a fully-wetted grain boundary forms when a small grain disappears and distorts an originally regular liquid-filled triple junction (Fig. 5.4). Surface energy anisotropy can be an additional, but not a necessary factor for disequilibrium melt distribution (Walte et al., 2003). This is confirmed by grain-scale numerical modeling of static liquid-bearing systems, which are allowed to recrystallize (Becker et al., 2003).

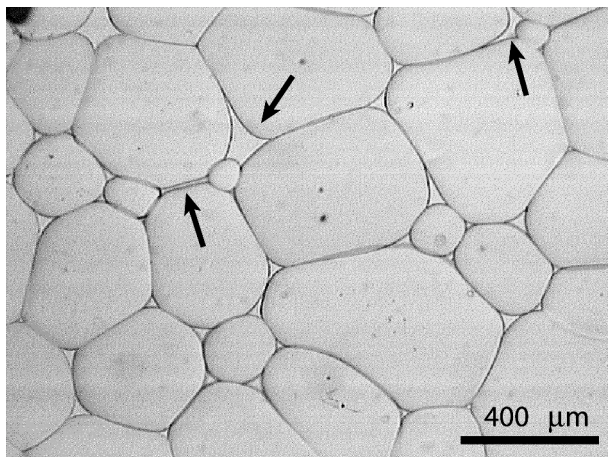


**Fig. 5.4.** Norcamphor plus ethanol liquid microstructure during grain coarsening. The aggregate displays a foam texture with smoothly curved grain boundaries. There is only one layer of norcamphor grains in the semi two-dimensional sample, so that the grain boundaries are oriented perpendicular to the glass slides. Note distortions of triangular liquid pockets and disequilibrium features (black arrows) near small grains. See also movie 2.05-3 on the enclosed DVD.

### 5.1.3 *Dynamic wetting angles*

This study concentrates on the detailed evolution of wetting angles in disequilibrium and evaluates their importance for geological liquid-bearing systems. Wetting angles can be temporally distorted under dynamic conditions, for example when they are forced to move as shown in Fig. 5.2b (e.g. de Gennes, 1985, Leger and Joanny, 1992). This effect is usually ignored in the geological literature, because a temporally changed wetting angle will quickly move the triple point back until  $\theta_{eq}$  is regained (Fig. 5.2b) (e.g. Laporte et al., 1997). However, this does only apply if the disturbing factor is temporary. If there is a mechanism available in geological systems that makes the triple junctions move continuously, the measured angles may represent dynamic angles, that might differ from the equilibrium angles ( $\theta_{dy} \neq \theta_{eq}$ ). Such a driving mechanism is static grain coarsening (recrystallization). Small, few-sided grains are consumed by larger many-sided grains so that the mean grain volume increases with time and total surface energy decreases (McCrone, 1949, Smith, 1964, Weaire and Rivier, 1984, Anderson, 1988, Karato, 1989). This means that the grain boundaries, and therefore the melt-filled three-grain triple junctions, are continuously moved and readjusted by the growing and shrinking grains nearby. Static grain growth is a significant process in the mantle (Karato, 1989, de Bresser et al., 1998) and in high-temperature experiments used to determine wetting angles (e.g. Faul, 1997, 2000). The systematic occurrence of dynamically changed wetting angles should therefore be taken into account. Unfortunately, high-temperature experiments only provide snapshots of the evolving microstructure, so that there is no easy way to know if the measured triple junctions were moving during the experiment or not. This leads to a number of questions: Is there a significant change of the effectively measured wetting angles in experiments due to ongoing static recrystallization? If yes, what is the relation between the dynamic wetting angle and the s-s-l triple junction velocity? What is the relation between the dynamic wetting angles and the formation of disequilibrium features? *In-situ* analogue experiments are well suited to investigate these questions because they allow the detailed observation of the evolving microstructure over time.

## 5.2 Experiments and Methods

### 5.2.1 *Experimental set-up*

The analogue system norcamphor + ethanol liquid was used to study the development of wetting angles over time in solid-liquid systems. Norcamphor ( $C_7H_{10}O$ ) is a hexagonal organic crystalline phase that exhibits crystal plastic behaviour at room temperature, analogous to minerals such as quartz or olivine (Bons, 1993, Bons et al., 1993, Herweg and

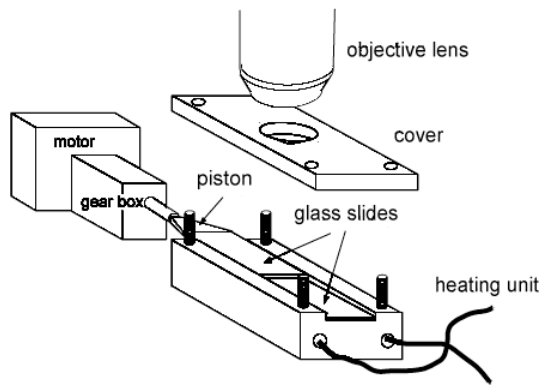


**Fig. 5.5.** Urai-Means transparent deformation rig with built-in heating unit and thermocouples that were used to control the temperature of the experiments. Redrawn after Passchier and Trouw (1996). Length of the apparatus is ca. 28 cm. Redrawn after Passchier and Trow (1996).

Handy, 1996, Bauer et al., 2000, Rosenberg and Handy, 2000, 2001). The ethanol, analogue for melt or high-temperature aqueous fluid, permits fast diffusion of dissolved norcamphor at room temperature so that continuous surface energy driven grain coarsening (liquid assisted recrystallization) takes place statically as in natural systems at high temperature conditions (Walte et al., 2003). The advantage of using this analogue system is that the norcamphor + ethanol aggregate approaches an ideal two-phase system of an isotropic crystalline phase containing a well-wetting ( $\theta_{eq} \ll 60^\circ$ ) liquid phase (Walte et al, 2003). The absence of a crystal lattice-controlled anisotropy is favourable for this study because it ensures that the system has a single valued  $\theta_{eq}$  regardless of the crystallographic orientation of adjacent grains (subgrain boundaries are an exception with a higher  $\theta_{eq}$ , but they can be easily identified in the experiments and were excluded for measurements). All wetting angle variations observed during an experiment can therefore be directly identified as  $\theta_{dy}$ , so that a systematic study of the  $\theta_{dy}$  evolution with time is possible. Using a fluid phase opposed to using a melt phase permits all experiments to be performed at room temperature (kept constant at  $25 \pm 1$  °C by air conditioning). This minimizes temperature gradients that can have a disturbing effect on liquid distribution (Leshner and Walker, 1988).

20–100- $\mu$ m-thick samples of norcamphor + norcamphor-saturated ethanol were wedged between two glass slides that were subsequently glued to each other to inhibit evaporation of the norcamphor-ethanol sample. The slides were placed in an Urai-Means transparent deformation rig with built-in thermocouples and a heating unit for an additional temperature control and regulation (Fig. 5.5) (Urai, 1983, Means, 1989). The apparatus was placed under a microscope which allowed continuous observation during an experiment. 756 x 512 pixel digital colour images were automatically taken with the image analysis programme “NIH image” (public domain software of the National Institutes of Health) at regular intervals from 10 seconds to 2 hours, depending on the duration and the required time resolution of the experiment.

The aggregate quickly forms a foam texture with smoothly curved grain boundaries between the crystals (Fig. 5.4). There is only one layer of norcamphor grains between the

glass slides so that a nearly two-dimensional solid-liquid texture is achieved with grain boundaries oriented perpendicular to the glass. The ethanol liquid is evenly dispersed within the sample, mainly in regular equal-sized three-grain triple junctions forming outward concave solid-liquid boundaries (Fig. 5.1). The liquid fraction in the experiments ranged between 2% and 13%, remaining constant during an experiment. Varying liquid fraction and varying sample thickness had no significant effect on the results.

### 5.2.2 Measurements

The aim of our experiments was to link the velocity of solid-solid-liquid triple interSections to their dynamic wetting angles. Wetting angle measurements were made directly from the image-stacks taken during the experiments. The velocity of the s-s-l triple junctions was calculated from their movement and the known time intervals between images of a movie. The largest uncertainty in the velocity measurements comes from the difficulty to determine the exact position of a triple point at each image, especially at low wetting angles.

Experiment	T (°C)	magnification	number of movies	measured triple junctions	number of measurements
2.07	25	200x	1	6	154
2.57	25	500x/200x	4	9	115

**Table 5.1.** Summary of the analysed experiments.

Wetting angles were determined by drawing tangents to the s-l-boundaries at the s-s-l-junction (Fig. 5.1). The angle can either be determined directly on the image (method used for Fig. 5.6), or by treating the two tangents as vectors and calculating the angle between them (all other reported angles). The visual estimation of the tangents to the curved boundaries is a source of some error. It has even been suggested that the result of wetting angle measurements depend mainly on the image magnification resulting in much lower angles measured from electron microscope images than from optical microscopy (Laporte, 1994). Although we cannot rule out similar overestimations of our wetting angle measurements, our results from optical images with 200x and 500x magnification are consistent, so that the systematic error in this magnification range is small. However, the problem of fitting tangents to the curved s-l-boundaries might be responsible for some of the variation between different experiments. We estimate our measurement precision to be about  $\pm 5^\circ$  within a single series of images. The development of two different static experiments were analyzed (table 1.). Triple junctions were chosen that showed a wide range of velocities and dynamic wetting angles

ranging from less than 0.1  $\mu\text{m/h}$  to 650  $\mu\text{m/h}$  and from  $5^\circ$  to  $120^\circ$ , respectively, to find the link between both parameters.

### 5.2.3 The calculation of forces acting on solid-solid-liquid triple junctions

Norcamphor-ethanol boundaries show no noticeable surface energy anisotropy (Walte et al., 2003), implying a single  $\gamma_{\text{SL}}/\gamma_{\text{SS}}$ -ratio and equilibrium wetting angle ( $\theta_{\text{eq}}$ ).  $\theta_{\text{eq}}$  was originally reported to be  $10\text{-}15^\circ$  by Walte et al. (2003), but is now revised upwards to about  $25^\circ$ , being the angle for immobile triple junctions (see below). Although absolute surface energies are unknown for our analogue system, we can use equation (1) to determine the  $\gamma_{\text{SL}}/\gamma_{\text{SS}}$ -ratio, which is 0.512 for  $\theta_{\text{eq}} = 25^\circ$ . When the unknown  $\gamma_{\text{SS}}$  is normalized to unity, 0.512 is the normalized  $\gamma_{\text{SL}}$ , to be used for the calculations below.

Two different approaches are possible to link acting forces to triple junction velocity. The first approach simply adds the three surface tension vectors, and the direction and length of the resulting force vector can then be directly compared to the measured triple junction velocity vector (Fig. 5.7a). With this approach, the triple junction is modeled as a physical entity that is directly moved in the direction of the acting force. The second approach envisions the s-s-l triple junction as a mere boundary point between the dry and the wetted portion of two adjacent crystals (Fig. 5.7b), similar to a migrating crack tip that is the boundary between the unfractured and the fractured part of a brittle material. Here, the migration of the triple junction is controlled by the perpendicular force component that differs

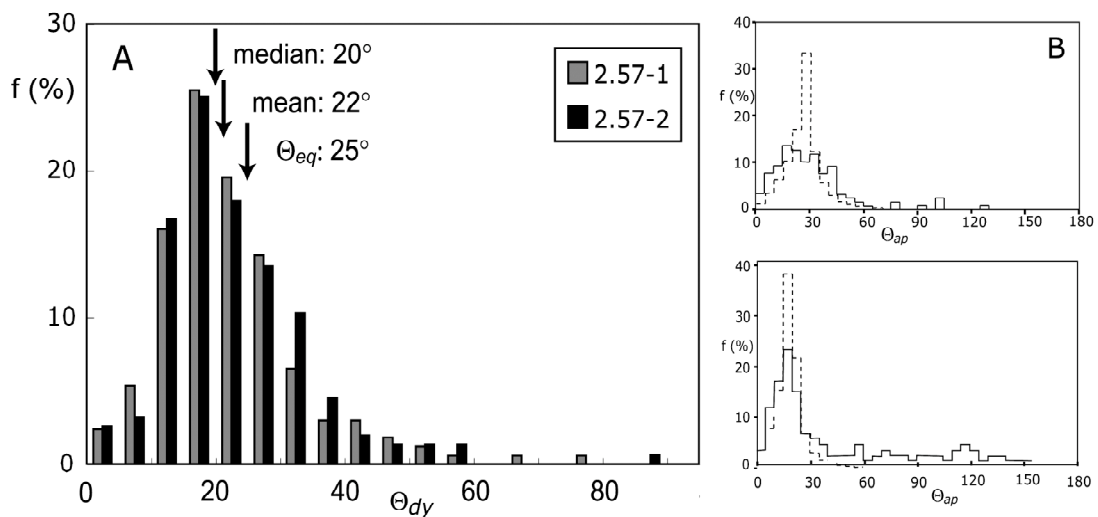


**Fig. 5.6. A:** Plot of true wetting angle variations versus frequency of two different norcamphor-ethanol experiments. Note that wetting angles were measured perpendicular to the solid-solid-liquid triple junction, i.e. these are not apparent variations due to Sectioning effects. Two different samples, 2.57-1 with  $\varphi \approx 4$  vol.%, 2.57-2 with  $\varphi \approx 13$  vol.%. Images taken with 500x magnification. **B:** Apparent wetting angle distribution in quartz + melt experiments for comparison, redrawn from Laporte et al. (1997). Distribution is wider than predicted for a single true wetting angle (stippled line).

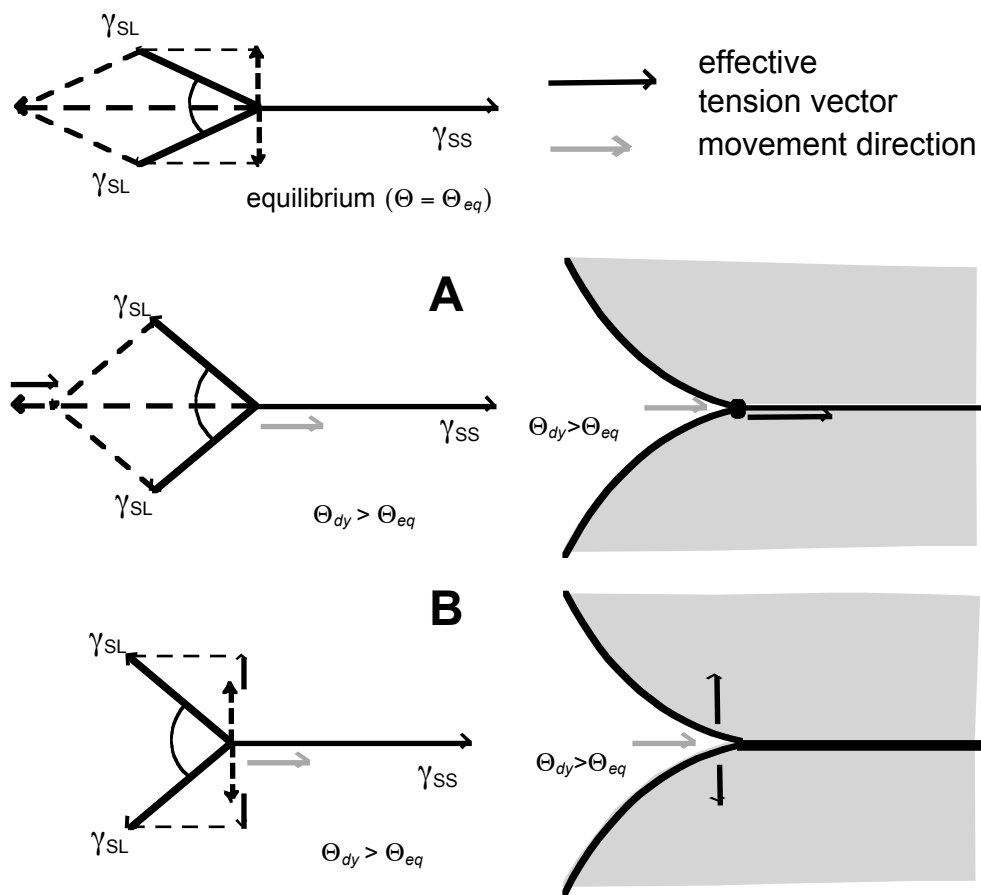


**Fig. 5.7.** Two models of driving forces for the migration of solid-solid-liquid triple junctions. Vector diagram on top shows the equilibrium case **A**: The junction velocity is linked to the net tension in the movement direction of the triple junction. **B**: The velocity depends on the tensional or compressional forces perpendicular to the solid-solid grain boundary.

from the force in equilibrium (at  $\theta_{tr} = \theta_{eq}$ ) (Fig. 5.7b, i.e. at  $\theta_{eq}$  the force is zero). This can be a pressing or tearing force component acting perpendicular to the s-s boundary surface, either pushing the s-s boundary together or pulling it apart. The instantaneous movement direction is therefore restricted by the orientation and movement of the opening or closing s-s grain boundary. If the s-s-l triple points are symmetric as in Fig. 5.7, the two suggested driving forces for triple point migration are as follows:

$$F_{//} = \gamma_{ss} \sin(2\theta_{SL}) \sin\left(\frac{1}{2}\theta_{dy}\right) \quad (5.2)$$

$$F_{\perp} = 2\gamma_{SL} \left\{ \cos\left(90^\circ - \frac{1}{2}\theta_{eq}\right) \cos\left(90^\circ - \frac{1}{2}\theta_{dy}\right) \right\} \quad (5.3)$$

Taking  $\theta_{eq} = 25^\circ$ , and normalizing  $\gamma_{ss}$  to unity, the normalized forces acting parallel ( $F_{//}$ ) and perpendicular ( $F_{\perp}$ ) to the triple junctions can be calculated as a function of the dynamic wetting angle (Fig. 5.8). Both forces cut the x-axis at  $25^\circ$ , as required by the definition of a

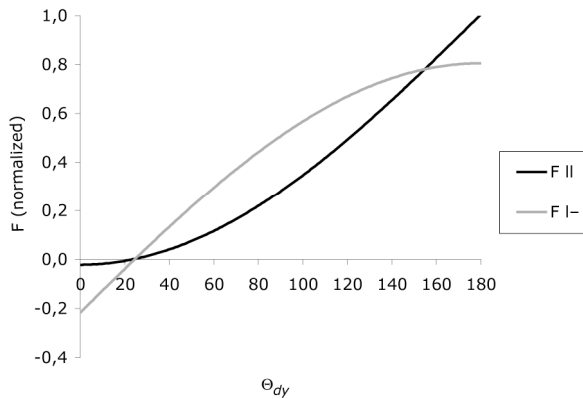


**Fig. 5.8.** Normalized forces per unit s-s-l junction parallel and perpendicular to the s-s grain boundary as a function of the dynamic wetting angle  $\theta_{dy}$ , calculated with equation (5.2) and (5.3), respectively.  $\theta_{eq} = 25^\circ$  and  $\Gamma_{ss}$  normalized to unity were assumed for the calculation.

static triple point at  $\theta_{eq}$ . Although the general trend of both curves is similar, it is evident that the curvatures are opposite and that at low  $\theta_{dy}$  higher negative forces are reached with the second model.

All perpendicular and parallel forces reported in the next Sections were calculated from the measured wetting angles with equations (5.2) and (5.3), i.e. the triple junctions were assumed to be symmetric as shown in Fig. 5.7. The simplification is justified because the determination of  $F_{\perp}$  and  $F_{||}$  is very sensitive to errors in the measurement of the orientation of the boundaries. Equations (5.2) and (5.3) are less sensitive to errors in these measurements.

## 5.3 Results

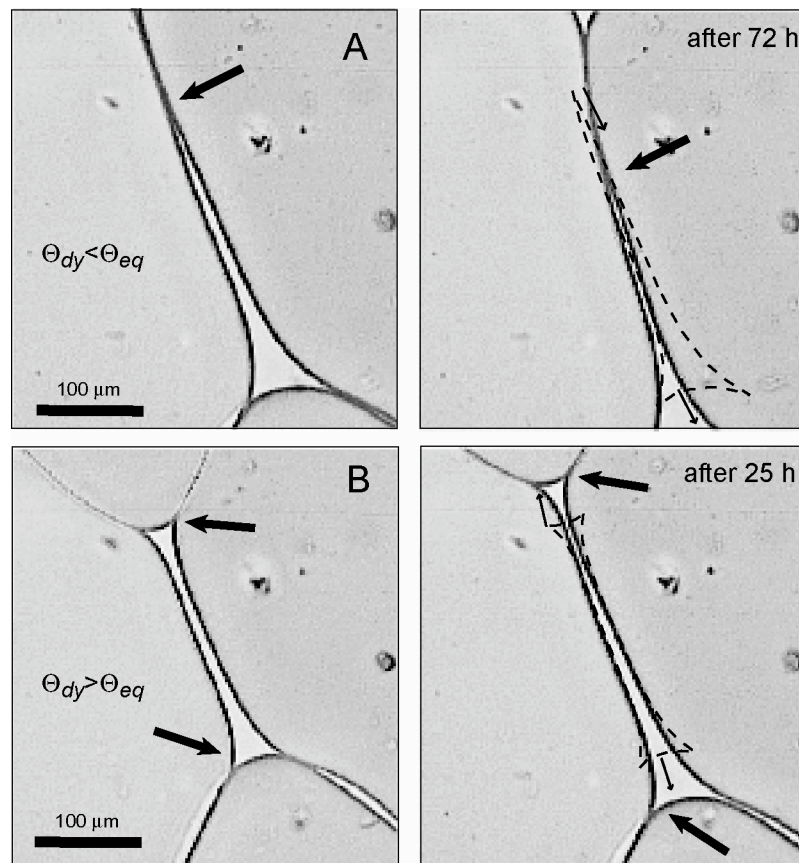
### 5.3.1 Variation of true wetting angles

Fig. 5.6a shows the variation of true wetting angles from two different experiments with a varying liquid fraction, 2.57-1 with  $\varphi \approx 4$  vol.% and 2.57-2 with  $\varphi \approx 13$  vol.%. The variation is large, bearing in mind the isotropic surface energy, and that these are *true* angles measured at  $90^\circ$  to the triple junctions. Both samples result in a similar wetting angle distribution, liquid fraction therefore appears to have no major influence on the distribution. The median and average of both distributions are  $20^\circ$  and  $22^\circ$  respectively. Interestingly, both values are underestimations of the equilibrium angle of  $25^\circ$ . Fig. 5.6b shows an *apparent* wetting angle distribution from literature (Laporte et al., 1997) for comparison. In the following Sections we will concentrate on the mechanisms leading to the wetting angle distribution in our experiments.

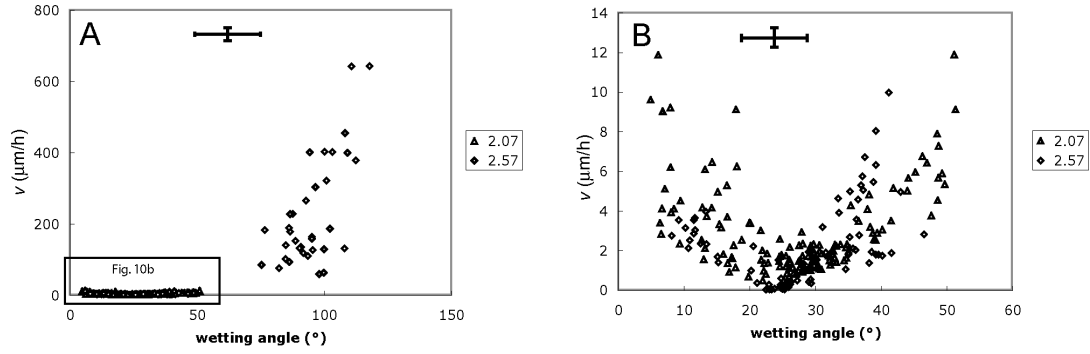
### 5.3.2 The correlation between dynamic wetting angle and triple junction velocity

Fig. 5.9 shows the qualitative connection between movement of an s-s-l triple junction and the dynamic wetting angle ( $\theta_{dy}$ ). If  $\theta_{dy}$  is smaller than  $25^\circ$ , the triple junction moves into the direction of the liquid phase, i.e. the s-s-boundary length increases (Fig. 5.9a). If  $\theta_{dy}$  is larger than  $25^\circ$ , the triple junctions move in the opposite direction (Fig. 5.9b), thereby opening and wetting the s-s-boundary (dynamic wetting). This behaviour is expected and in accordance with both suggested driving forces of tension acting parallel and normal to the junction. Fig. 5.10 plots absolute triple point velocity ( $v_{tp}$ ) versus  $\theta_{dy}$ . The minimum velocity occurs roughly at  $25^\circ$  (Fig. 5.10b), which is therefore assumed to be the actual equilibrium wetting angle for norcamphor-ethanol. The data distribution in Fig. 5.10b is approximately symmetric around  $25^\circ$ , i.e. a triple junction with a dynamic wetting angle of  $10^\circ$  has approximately the same velocity as a triple junction with a dynamic wetting angle of  $40^\circ$ , within error.

In the Figs. 5.11 and 5.12 the normalized parallel and perpendicular forces calculated with equations (5.2) and (5.3) of the measurements are plotted versus the velocity. Negative



**Fig. 5.9.** Two examples for the migration of s-s-l triple junctions where  $\theta_{dy} \neq \theta_{eq}$ . **A:** At lowered dynamic wetting angle ( $\theta_{dy} < \theta_{eq}$ ) the junction moves in the direction of the melt pocket, and the s-s grain boundary length increases. **B:** When the dynamic wetting angle is raised ( $\theta_{dy} > \theta_{eq}$ ), the junctions are pulled in the direction of the shrinking grains, and the s-s grain boundary is opened and wetted. See also movie 2.57-8 on the enclosed DVD.



**Fig. 5.10. A:** Plot of triple junction velocities versus the measured dynamic wetting angles. Note, that the highest velocities are only reached when is  $\square_{dy}$  raised . **B:** Enlargement of the marked part of A. The equilibrium wetting angle ( $\square_{eq}$ ) is the angle of minimal velocity at 25°. The graph appears approximately symmetric around  $\square_{eq}$ . Error bars show the estimated accuracy of the data.

forces are due to dynamic angles below 25°. Both curves qualitatively repeat Fig. 5.10, but Fig. 5.11a is asymmetric around the  $F_{//}=0$  axis while Fig. 5.12 is approximately symmetric around the  $F_{\perp}=0$  axis. To derive an empirical force–velocity function from our measurements, the absolute normalized perpendicular and parallel forces are plotted versus the absolute triple point velocity in Figs 5.13 and 5.14. This means that in these figures lowered or a raised dynamic wetting angle are not distinguished by their sign.

Fig. 5.13 plots triple point velocity versus perpendicular force (Fig. 5.7b) and Fig. 5.14 plots triple point velocity versus parallel force (Fig. 5.7a). The data points in Fig. 5.13 can be described with an exponential function that connects normalized perpendicular force to the triple junction velocity:

$$v_{(F_{\perp})} \square 0.75 \cdot \exp^{10.8 \cdot F_{\perp}} \quad (5.4)$$

The velocity  $v(F_{\perp})$  is expressed in  $\square$ m/h,  $F_{\perp}$  is the normalised force acting perpendicular to the s-s junction (Fig. 5.7b). Although the data spread at a low perpendicular force is quite large, Fig. 5.13b shows that most measurements lie on the curve within their uncertainty, no matter whether  $\square_{dy} < \square_{eq}$  or  $\square_{dy} > \square_{eq}$ . To compare the function to the parallel force ( $F_{//}$ )-velocity model (Fig. 5.7a), equation (4) was recalculated to the parallel force and drawn in Fig. 5.14. It can be seen that the function fits the data for  $\square_{dy} > \square_{eq}$  well, however, the measurements for  $\square_{dy} < \square_{eq}$  do not lie on the curve. A second function would be necessary to describe the parallel force-velocity relation for  $\square_{dy} < \square_{eq}$ . Using the normal component of tension as in Fig. 5.13 thus has the advantage that triple point velocity can be linked to a single parameter: the absolute normal component of the tension that deviates from equilibrium (Fig. 5.7b). From a physical point of view it is preferable if the velocity can be linked to a single parameter such as the normal tension for all dynamic angles, over the option that has to distinguish between

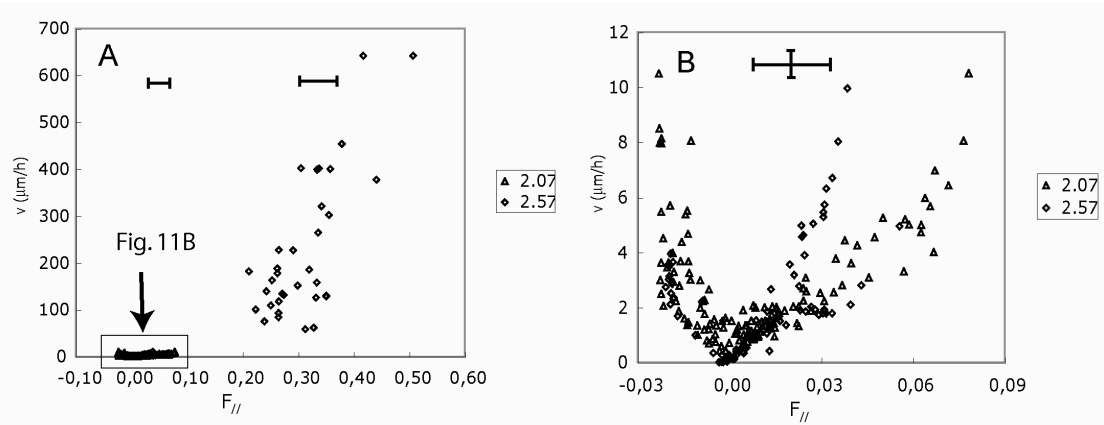


**Fig. 5.11. A:** Parallel force ( $F_{||}$ ) versus absolute triple junction velocity, calculated with equation (5.2) (model 1, Fig. 5.7a). Points lying at  $F_{||} > 0$  indicate raised  $\square_{dy}$ , points situated at  $F_{||} < 0$  indicate lowered  $\square_{dy}$ . **B:** Enlargement of the marked part in A. Error bars show the estimated accuracy of the data.

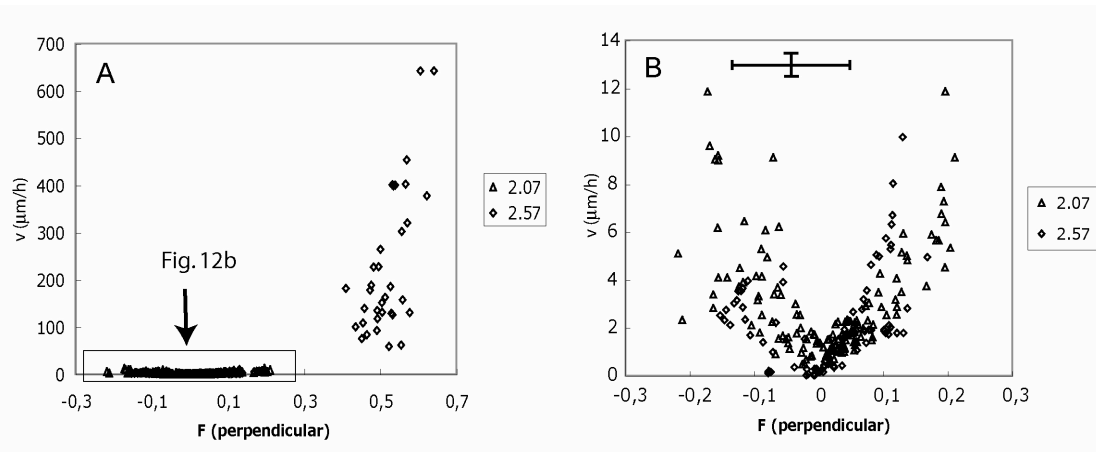


**Fig. 5.12. A:** Perpendicular force ( $F_{\perp}$ ) versus triple junction velocity, calculated with equation (5.3) (model 2, Fig. 5.7b). Points lying at  $F_{\perp} > 0$  indicate raised  $\square_{dy}$ , points situated at  $F_{\perp} < 0$  N/m indicate lowered  $\square_{dy}$ . **B:** Enlargement of the marked part in A. Note the more symmetric distribution of the data compared to Fig. 5.11b. Error bars show the estimated accuracy of the data.

two cases, raised and the lowered wetting angles, before it can be linked to the tension acting in the movement direction.

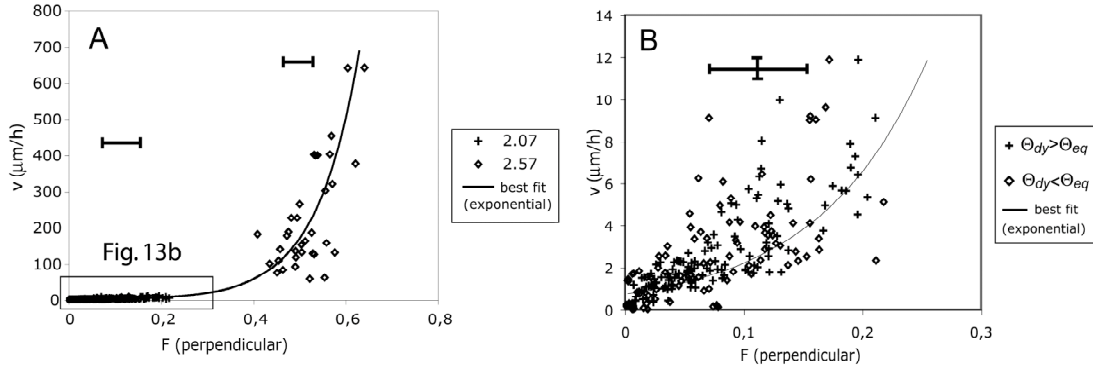


**Fig. 5.13. A:** Absolute perpendicular force ( $F_{\perp}$ ) versus absolute triple junction velocity, calculated with equation (5.2) (model 2, Fig. 5.7b). Raised and lowered  $\theta_{dy}$  are not distinguished. Best fit of the data by an exponential function (equation 5.4) is included. **B:** Enlargement of the marked part in A. The lowered  $\theta_{dy}$  measurements plot along the same exponential function as the raised  $\theta_{dy}$ . Error bars show the estimated accuracy of the data.

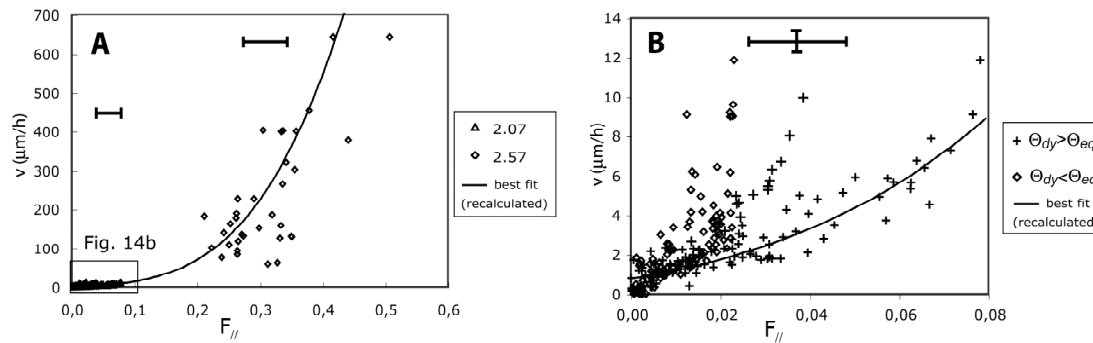


**Fig. 5.14. A:** Absolute parallel force ( $F_{\parallel}$ ) versus absolute triple junction velocity, calculated with equation (5.3) (model 1, Fig. 5.7a). Raised and lowered  $\theta_{dy}$  are not distinguished. Equation (5.4) from Fig. 5.13 was recalculated to  $F_{\parallel}$  and included as a trend line. **B:** Enlargement of the marked part in A. The lowered  $\theta_{dy}$  follow a different trend than the raised  $\theta_{dy}$  and are not described well by equation (5.4). Error bars show the estimated accuracy of the data.

### 5.3.3 The connection between disequilibrium features and dynamic wetting angles in solid-liquid systems

The formation of disequilibrium features, such as fully-wetted grain boundaries, has been explained with the influence of ongoing grain coarsening by Walte et al. (2003) and Becker et al. (2003). They showed that the temporal formation of disequilibrium features is energetically favourable during the disappearance of small grains. Our perpendicular tension–triple junction velocity function (equation (5.4) and Fig. 5.13) provides a more detailed understanding of the connection between  $\theta_{dy}$  and the development of a disequilibrium feature. Consider a typical starting configuration of a small dissolving grain surrounded by larger grains (Fig. 5.15a). The liquid-filled triple junction is slightly elongated with a lowered  $\theta_{dy}$  at s-s-l junction 1 and a raised  $\theta_{dy}$  at junctions 2 and 3 (Fig. 5.15a). Shrinking of the dissolving grain on the left raises  $\theta_{dy}$  at junctions 2 and 3, which move with

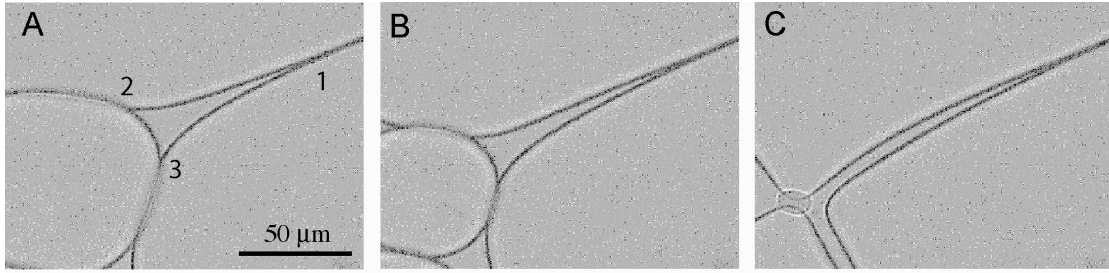


**Fig. 5.15.** Formation of a disequilibrium feature in norcamphor plus ethanol. As long as the shrinking velocity of the small grain is not faster than ca. 5-10  $\mu\text{m/h}$ , all s-s-l junctions move with a comparable velocity (**A**) determined by a lowered  $\theta_{dy}$  of junction 1 and raised  $\theta_{dy}$  of junctions 2-3. **B**: Migration velocity of junctions 2 and 3 continues to increase as their  $\theta_{dy}$  increases. Junction 1 lags behind as its  $\theta_{dy}$ , and therefore driving force, cannot be lowered further. **C**: A wetted grain boundary is eventually formed as the small grain has disappeared. See also movie 2.32-6+7 on the enclosed DVD.

increasing velocity. The smaller the grain, the higher the velocity becomes, and the higher the  $\theta_{dy}$  at junctions 2 and 3 ( $\theta_{dy}$  up to ca.  $120^\circ$  have been measured at very small grains with instantaneous velocities up to 0.6 mm/h, see Fig. 5.10a). Triple junction 1 moves much slower, as there is only a limited range of possible smaller wetting angles than  $\theta_{eq} = 25^\circ$  (the lowest angles measured in our experiments are usually 5-10°, therefore yielding normal surface force of ca. -0.18 to -0.13). The maximum possible velocity is therefore only about 5-10  $\mu\text{m/h}$  for the case of a lowered dynamic angle, which is the velocity that is reached at a junction with a raised  $\theta_{dy}$  of around  $40^\circ$  (Fig. 5.10b). Initially, all three junctions move with a comparable velocity. However, while junction 2 and 3 can continuously increase their velocity as their  $\theta_{dy}$  increases, junction 1 reaches a stable, slower velocity as its  $\theta_{dy}$  approaches a minimum. Junction 1 can therefore not keep up with the other two junctions to maintain an equilibrium shape of the liquid pocket (Fig. 5.15b). The result is a strongly elongated melt pool that can even become a completely wetted grain boundary (Fig. 5.15c) or a trapped liquid lens. A fully wetted grain boundary that is formed by a neighbour switch or more complex grain interactions that lead to large liquid patches can be explained in a similar way by the interplay of raised and lowered  $\theta_{dy}$  and the concomitant asymmetry in velocity. These processes should generally occur in all solid-liquid systems. The effect should be most pronounced in systems with a low  $\theta_{eq}$ , where the range in velocities for elevated  $\theta_{dy}$  is much larger than for reduced  $\theta_{dy}$ .

## 5.4 Discussion

This study is the first survey of the relation between dynamic wetting angles and the velocity of solid-solid-liquid grain junctions in a polycrystalline solid-liquid system. Existing studies on dynamic wetting angles in the physical literature usually concentrate on the special solid-liquid-vapor case, e.g. that of a liquid droplet on a flat solid surface (e.g. de Gennes, 1985,

Leger and Joanny, 1992). Their results are therefore not easily comparable to our case. The dynamic wetting angle of a moving droplet was shown to depend mainly on the roughness of the surface on which it migrates. In our experiments there is no rough surface that delays the three-phase junction by friction, and migration of our s-s-l triple junctions is driven by a complex interplay between growing and shrinking grains which is dependent on diffusion and reaction processes. Our two suggested relations between the resulting tension in the movement direction and perpendicular to the movement direction (Fig. 5.7a-b) mean that there is either work done to move the triple junction or to open or close the s-s grain junction during grain coarsening. The comparison of these two suggested relations shown in Figs. 5.11-14 reveal a better correlation of the empirical data with the force perpendicular to the s-s grain boundary regardless of lowered or raised  $\theta_{dy}$  with respect to  $\theta_{eq}$ . A s-s-l triple junction can therefore be modeled as a passive boundary between the dry and the wetted part of adjacent grains (Fig. 5.7b) that is opening or closing depending on the external geometry.

The significance of these results for geological systems is evident from Fig. 5.6. Contrary to the range of wetting angles reported from high-temperature experiments that are generally interpreted as a purely apparent wetting angle variation around a single  $\theta_{eq}$  (Fig. 5.6b-c), Fig. 5.6a shows that true wetting angles measured normal to the s-s-l junctions also show a wide distribution. The reason is that actual wetting angles are continuously being modified by ongoing recrystallization. For a system with isotropic surface energy like our analogue system, the true angle distribution depends on the recrystallization rate and the equilibrium wetting angle. A high recrystallization rate leads to a wide distribution of measured wetting angles, a lower rate yields a narrower distribution, and a single  $\theta_{eq}$  is expected for the hypothetical static case without recrystallization. Since grain coarsening is a process generally occurring in all synthetic and natural polycrystalline systems, we suggest that the reported range of apparent wetting angles in high-temperature experiments results partly from dynamic modification of wetting angles, exacerbated by Sectioning effects. This conclusion is supported by the reported  $\theta_{ap}$  distribution in high-temperature experiments, which is significantly wider than the expected theoretical distribution for Sectioning of a single true wetting angle (Fig. 5.6b) (Laporte, 1994, Laporte et al., 1997) (but note that these authors explain this by crystal anisotropy). Another somewhat surprising result of the measurements of Fig. 5.6a is that both the mean and the median of the wetting angle distribution underestimate the equilibrium angle. The occurrence and importance of this underestimation should be further investigated, e.g. by numerical simulations that combine the distribution of liquid with different rates of recrystallization and different wetting angles (Becker et al. 2003) before implications for the interpretations of high-temperature experiments can be drawn.

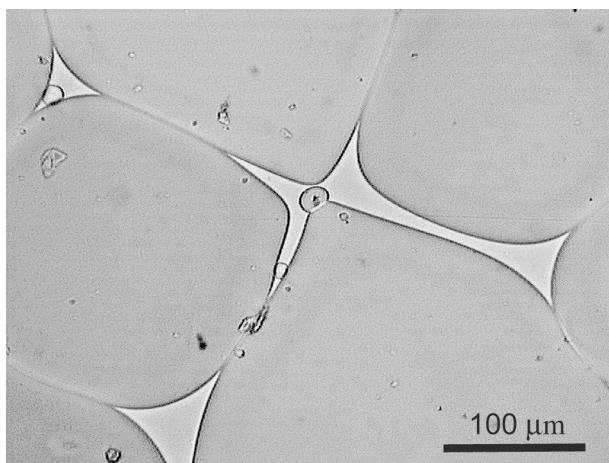


**Fig. 5.16.** Example for equilibrium and disequilibrium. Only the liquid triangle in the upper left fulfills both requirements for measuring wetting angles in equilibrium. The central liquid pocket can be identified as in non-equilibrium by the small grain in the center and the wetted grain boundary towards the right of the grain.  $\theta_{tr}$  measurements would yield too high (at the side of the small grain) or too low wetting angles. See also movie 2.57-9 on the enclosed DVD.

We currently cannot quantify the magnitude of systematic errors for reported equilibrium wetting angles, but suspect they may be significant, due to the specific conditions of HT experiments. To attain a thermodynamic “equilibrium“ (steady state) microstructure in reasonable experimental time (hours to weeks), the grain size in HT experiments is usually chosen much lower than in natural systems (μm vs. mm-cm in nature). The recrystallization rate is therefore high, probably resulting in a much wider wetting angle distribution than expected in natural rocks. Especially in cases where wetting angles were reported to be near the critically liquid connection threshold of 60°, small systematic errors could be important for the geological interpretation of the results. Ideally,  $\theta_{eq}$  should only be measured at static, non-moving triple junctions. To ensure this, however, continuously observable *in-situ* experiments are necessary, which have not been realized with rock-forming minerals, yet. However, two simple rules for the measurement of triple junctions can be formulated that help to find the true  $\theta_{eq}$  and minimize systematic errors by  $\theta_{dy}$  (Fig. 5.16):

1. Only triple junctions surrounded by “large” approx. equal sized crystals with rather straight s-s grain boundaries should be chosen for measurement. No melt pockets adjacent to small grains with highly curved grain boundaries should be used. This ensures that the grain boundaries and therefore the melt-filled triple junctions probably did not migrate rapidly before quenching.
2. Disequilibrium features such as large liquid patches, trapped liquid lenses, or fully wetted grain boundaries should be avoided for measurement. Regular, triangular melt filled triple junctions should be favoured (Fig. 5.16). Even if disequilibrium features are surrounded by large grains fulfilling requirement 1, it is very probable that a small grain has just disappeared or is not cut by the thin Section. This generally leaves strongly distorted, rapidly moving triple points (Walte et al., 2003).

We are aware that the second rule concerns the possible occurrence of “disequilibrium” features that were created by anisotropic surface energy, which leads to a variation of the true  $\theta_{eq}$ . We suggest to use crystal facets as an indication for real anisotropic  $\theta_{eq}$  (cf. Waff and Faul, 1992, Faul, 1997, Laporte et al. 1997, Faul, 2000). Real transient disequilibrium features, which should be avoided, are characterized by slightly or variably curved s-l boundaries that are different from the mean curvature and therefore indicate disequilibrium, which cannot be explained by crystal lattice orientation (Walte et al., 2003). When following these two rules when analyzing wetting angle experiments, the measurements should result in a lower variation in measured wetting angles, resulting mainly from Sectioning effects.

#### 5.4.1 Mechanical strength of grain boundaries in solid-liquid systems

For wetting angles above  $0^\circ$  it is energetically favourable for two adjacent crystals to form a dry solid-solid grain boundary. Two welded grains with a common s-s boundary form their  $\theta_{eq}$  at their side so that there is a characteristic welding to wetting ratio for each wetting angle (Fig. 5.17a) (Stephensen and White, 1967). Now consider a mechanical stress applied to the two grains (Fig. 5.17b-c). The result will be a raised or lowered  $\theta_{dy}$  at the s-s boundary, which depends on the mechanical stress applied, the equilibrium wetting angle  $\theta_{eq}$ , and the value of  $\theta_{sl}$ . The result is that the two triple junctions will start to migrate either towards each other in relative extension (Fig. 5.17b) or away from each other in relative compression (Fig. 5.17c). In extension the grains will eventually disconnect, which is equivalent to an intergranular fracture. However, this is a time dependent process. If the tension is low, it follows that  $\theta_{dy}$  is only moderately raised and according to Fig. 5.13 and equation (5.4) the disconnection will take more time than for high tension that forces a high  $\theta_{dy}$  upon the triple junctions. Since the stress-velocity function is exponential, high relative tensional stresses give the impression of a “catastrophic” failure expected for brittle processes. However, even very low stresses may eventually lead to intergranular failure. It follows that grains may “break” apart by a time dependent process, without yield strength, which might be of relevance for deformation mechanisms like grain boundary sliding that strongly depend on the mechanical strength of initially welded grain boundaries (Mecklenburg and Rutter, 2003, see Chapter 6). This might also be an explanation for the regularly observed elongated melt pools oriented roughly parallel to  $\theta_l$  in high-temperature experiments (e.g. Daines and Kohlstedt, 1997, Gleason et al., 1999). For s-s boundaries normal to  $\theta_l$  there is an effective compaction leading to a decreased dynamic angle and therefore increased welding, while s-s boundaries parallel to  $\theta_l$  experience an effective tensional stress, which leads to increased dynamic angles, dynamic wetting, and eventually to the disconnection of grains and formation of elongated melt pools. Note, that this explanation is different to the explanation given by Daines and Kohlstedt

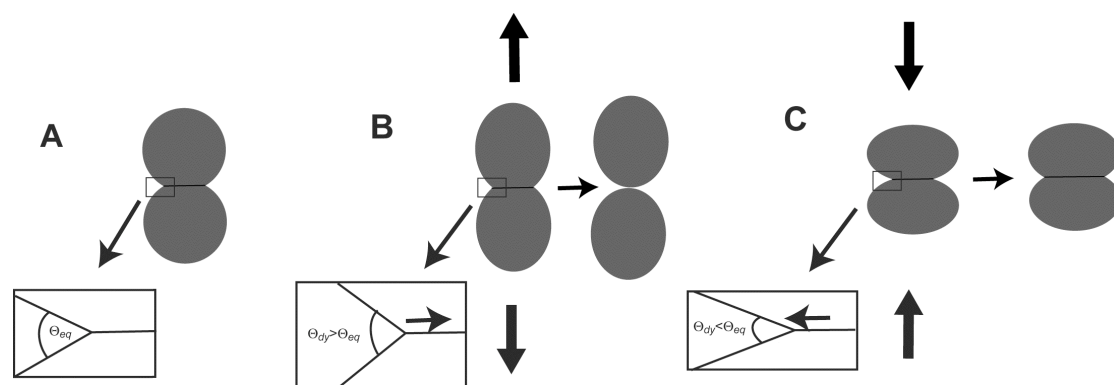


**Fig. 5.17.** The behavior of two isotropic grains surrounded by liquid subjected to mechanical stresses. **A:** If  $\theta_{eq} > 0^\circ$  the grains will form an aggregate with a wetting angle equaling  $\theta_{eq}$ . **B:** Extension normal to a s-s boundary raises  $\theta_{dy}$ , causing opening and wetting of the grain boundary until the grains disconnect. **C:** Compression normal to a s-s boundary lowers  $\theta_{dy}$ , causing the s-s-l junction to move apart and increasing the welded area.

(1997). They assume a locally *lowered* wetting angle to  $0^\circ$ , probably by a pressure difference between melt and solid and thereby dynamic wetting of the grain boundary, while our model assumes a *raised* dynamic angle ( $\theta_{dy}$ ) because of non-hydrostatic stress which leads to disconnection of grains ( $\theta_{eq}$  remains unaltered).

## 5.5 Conclusion

The migration path of an individual liquid-filled triple junction in an isotropic static polycrystalline liquid-bearing system is determined by the equilibrium wetting angle, the recrystallization rate, and the geometry of the adjacent grains. During a single experiment, such a triple junction can move into different directions changing direction and velocity over time, it can split (by a neighbour switch) or merge with other triple junctions (when grains disappear). When this happens, the triple junction is temporarily distorted (Walte et al. 2003), which means that the individual s-s-l triple points (or s-s-l triple lines and s-s-s-l quadruple points in 3-D) move independently with different velocities. The results of this study indicate that the velocity of a single s-s-l triple point in an ideal system is always expressed by a characteristic dynamic wetting angle. This means, that the three dynamic wetting angles of a triple junction contain the full information on the current velocity and tensional state of this junction. By measuring the dynamic wetting angles of an individual “disequilibrium” feature it should therefore be possible to predict its future development. The main results of the present study can be summarized as follows:

1. Ongoing surface energy driven recrystallization causes a widening of the wetting angle distribution even in systems with isotropic surface energy. This is important for the interpretation of HT experiments used to find equilibrium wetting angles. Our measurements indicate that both the mean and the median wetting angle of the measured wetting angle distribution underestimate the true equilibrium angle in the system.
2. There is an exponential relation between the tension acting normal to the s-s-l triple junction and its velocity.
3. Contrasting velocities between raised and lowered  $\gamma_{dy}$  compared to  $\gamma_{eq}$  at liquid filled three-grain triple junctions or during neighbour switches lead to the formation of disequilibrium features such as fully wetted grain boundaries.
4. Based on these observations it can be inferred that the welding strength of two adjacent grains is time-dependent. High tensional stresses lead to a fast intergranular “fracture“. However, even very low tensions are expected to eventually lead to disconnection of grains.

Polycrystalline solid-liquid systems are never in true thermodynamic equilibrium. Static, surface-energy driven and liquid-assisted recrystallization and its influence on the dynamic wetting angles has previously been largely neglected but is important for understanding the distribution and behaviour of liquid in partially molten or high-temperature aqueous fluid-bearing systems. Possible disequilibrium should always be taken into account when measuring wetting angles in geological relevant solid-liquid systems.



## 6. Deformation of melt-bearing systems – insight from *in-situ* grain-scale analogue experiments<sup>3</sup>

### Abstract

The deformation behaviour of partially molten rocks was investigated using effectively 2-dimensional analogue experiments with norcamphor + ethanol, as well as partially molten  $\text{KNO}_3 + \text{LiNO}_3$ . Three general deformation regimes could be distinguished in the experiments. In regime I, above ca. 8-10 vol.% liquid (melt) fraction ( $\varphi_{\text{bulk}}$ ), deformation is by compaction, distributed granular flow, and grain boundary sliding (GBS). At  $\varphi_{\text{bulk}} < 8-10$  vol.% (regime II), GBS localises in conjugate shear zones. Liquid segregation is inefficient or even reversed as the dilatant shear zones draw in melt to locally exceed the 8-10 vol.% liquid fraction threshold for GBS. At even lower  $\varphi_{\text{bulk}}$  (regime III), all grains form a coherent framework that deforms by grain boundary migration accommodated dislocation creep, associated with efficient segregation of remaining liquid. The transition liquid fraction between regimes II and III varies significantly between the two systems. It lies at about 4-8 vol.% for the norcamphor + ethanol experiments, and around 1 vol.% for the  $\text{KNO}_3 + \text{LiNO}_3$  experiments. Regime II behaviour can explain the frequently observed small melt-bearing shear zones in partially molten rocks.

**Keywords:** analogue experiments, norcamphor, magma segregation, granular flow, partially molten rocks, grain boundary sliding

### 6.1 Introduction

Liquid-bearing systems range from almost complete solid grain aggregates with minor amounts of liquid between grains to almost fully liquid magma in which isolated crystals are suspended. The amount of liquid is one of the primary parameters that determines the rheological behaviour of such composite systems. Three main types of behaviour can be distinguished:

---

<sup>3</sup> Walte, N.P., Bons, P.D., Passchier, C.W., 2004. Deformation of melt-bearing systems – insight from in situ grain-scale analogue experiments. *Journal of Structural Geology*, submitted.

1. High liquid fraction: crystals are suspended in the liquid. The mechanical behaviour is controlled primarily by the liquid viscosity and can be described as that of a dilute suspension (Einstein, 1906, Ryerson et al., 1988).
2. Intermediate liquid fraction: crystals form an aggregate, and the rheological behaviour is that of granular flow and grain boundary sliding (Rutter, 1997, Petford, 1998, Paterson, 2001).
3. Low liquid fraction: grains form an interlocking load-bearing framework, and the mechanics of the composite system are controlled by the rheology of the solid phase (Arzi, 1978, Vigneresse et al., 1996):
  - a) One possibility is that behaviour of the composite system is controlled by the (non-linear) viscosity of the solid, which deforms by diffusion or dislocation creep mechanisms (e.g. Hirth and Kohlstedt, 1995a, 1995b, Gleason et al., 1999, Mei et al., 2002).
  - b) Alternatively, brittle deformation by intracrystalline fracturing may occur (e.g. van der Molen and Peterson, 1979, Dell'Angelo and Tullis, 1988, Rutter, 1997, Renner et al., 2000, Holyoke and Rushmer, 2002).

Significant changes in strength and liquid transport are expected when liquid-bearing systems move from one type of behaviour to another, for instance during progressive melting, or during crystallisation of a magma (Arzi, 1978, van der Molen and Paterson, 1979, Vigneresse et al., 1996). Most attention has been paid to the rheological transition between melt-dominated behaviour (1+2) and flow dominated by the solid phase rheology (3) with its associated change in viscosity over many orders of magnitude. For this transition Arzi (1978) suggested a rheologically critical melt percentage (RCMP) that marks a sharp drop in strength. The RCMP is important to several systems, such as orogenic belts that contain partially-molten zones, like the Himalayas. If these partially-molten zones exceed the RCMP, they will constitute major zones of weakness that may mechanically detach the overlying crust from the orogenic root and mantle (Schott and Schmeling, 1998, Arnold et al., 2001). Exceeding the RCMP may also cause the wholesale mobilisation and diapiric ascent of partially molten rock (Weinberg and Podlachikov, 1994, Paterson and Vernon, 1995). Strong changes in rheology with changing melt fraction are also critically important for porosity waves. These are ascending zones of increased melt-bearing porosity, that are proposed as one of the mechanisms of melt ascent beneath, for example, mid-oceanic ridges (Barcilon and Richter, 1986, Scott and Stevenson, 1986, McKenzie, 1987, Kelemen et al., 1997, Holzman et al., 2003a). Even though the background melt percentage may be well below the RCMP, the

porosity waves themselves may contain enough melt to overcome the RCMP, which has to be considered for numerical models of these processes (Rabinowicz et al., 2001).

Despite the importance of the change in behaviour from melt-dominated flow to solid-phase-dominated rheology, there is still much uncertainty about the nature of this transition. Experiments have indicated either a dramatic change in rheology when the RCMP is crossed (Arzi, 1978, van der Molen and Paterson, 1979), or a gradual transition (Rutter and Neumann, 1995, Bagdassarov and Dorfman, 1998, Rutter, 1997, Renner et al., 2000, Rosenberg, 2001). High-temperature experiments on partial melts are normally restricted to measurement of stress-strain rate relationships and post-mortem analyses of the microstructure. Comparison of rheological data for different melt fractions are complicated by the fact that the melt fraction is most commonly changed by varying the temperature (e.g. Rutter and Neumann, 1995) or the water content of a sample (e.g. van der Molen and Paterson, 1979), both of which may significantly change the viscosity of the melt phase. The role of melt-enhanced embrittlement is also often unclear (Rutter and Neumann, 1995).

*In-situ* analogue experiments with partially-molten rock analogues provide a different approach to investigating these problems (Means and Park, 1994, Park and Means, 1996, Bauer et al., 2000, Rosenberg and Handy, 2000, 2001, Walte et al., 2003). Instead of focussing on the measurement of rheology, analogue experiments reveal processes on the grain-scale when a melt-bearing system is deformed. This study presents two sets of analogue experiments with a single crystalline phase (norcamphor or  $\text{KNO}_3$ ) plus a liquid phase with a well-constrained behaviour as a melt analogue (ethanol or  $\text{KNO}_3\text{-LiNO}_3$  melt) that is easily observable *in-situ* (Walte et al., 2003). These systems allow to continuously observe the microstructural processes and changes in deformation behaviour as a function of a varying liquid fraction within a single experiment. The experiments show the effect of the different deformation regimes on melt-segregation. They also show that the transition between the regimes is not only a function of melt percentage, but also of the strength of the solid phase, the strain rate, the melt pressure and the wetting behaviour of the melt.

## 6.2 Experiments

Two different sets of experiments were performed. In one set, norcamphor and norcamphor-saturated ethanol liquid were used as analogues for a monomineralic solid phase and melt, respectively (cf. Walte et al., 2003). Norcamphor ( $\text{C}_7\text{H}_{10}\text{O}$ ) is an organic crystalline compound with hexagonal symmetry and crystal-plastic rheology at room temperature, which has been used as an analogue for rock-forming minerals such as quartz or olivine (Bons, 1993, Bons et al., 1993, Herwegh and Handy, 1996, Bauer et al., 2000, Rosenberg and Handy,

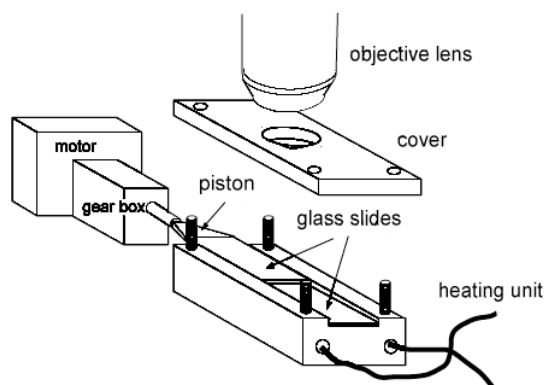


**Fig. 6.1.** Sketch of the Urai-Means linear deformation apparatus. The ca. 100  $\mu\text{m}$  thick sample is situated between the glass slides. Redrawn after Passchier and Trow (1996).

2000, 2001, Walte et al., 2003). The ethanol permits fast diffusion of dissolved norcamphor at room temperature so that continuous surface-energy driven grain coarsening (Ostwald ripening or liquid assisted recrystallization) takes place as in natural systems at high temperature conditions (Walte et al., 2003).

The second set of experiments was conducted with a mixture of 90-95 wt. %  $\text{KNO}_3$  and 5-10 wt. %  $\text{LiNO}_3$ . These nitrates have a eutectic point at  $134 \pm 1^\circ\text{C}$  (Guizani et al., 1998) and therefore are in the temperature range of *in-situ* analogue experiments. Nitrates such as  $\text{KNO}_3$  are similar to carbonates, such as calcite, in both crystallography and rheological behaviour (Tungatt and Humphreys, 1981).

Experiments were performed in a linear, Urai-Means see-through deformation apparatus (Fig. 6.1), which allows for continuous observation of the sample with a microscope during an experiment (Urai, 1983, Means, 1989). Approximately 100  $\mu\text{m}$  thick samples were wedged between glass plates and positioned in a brass housing, which contains two heating elements and holes to view the thin-Section-like sample. Pure shear deformation was induced by gluing one thin cover slip as piston on each glass plate, on opposite sides, and sliding the upper glass plate relative to the lower one. Sliding of the glass plate was driven by a motor at a constant displacement rate, resulting in strain rates between approximately  $10^{-4}$  and  $10^{-6} \text{ s}^{-1}$  depending on the motor used and the distance between the pistons. A barrier of silicone putty (“Rhodorsil gumme”) surrounded the sample to inhibit evaporation of the volatile norcamphor and the ethanol. At the beginning of the experiments, the barrier was not in contact with the sample, so that chemical interaction between the sample and the barrier was inhibited. The samples were therefore unconfined at the sides during the deformation. Liquid that was segregated during the experiments collected between the sample and the barrier. In long-term experiments, local dissolution and dilution of the silicone putty was observed by segregated liquid that came in contact with the putty barrier. However, no effect of the interaction between the silicone putty and the sample was noticed in the observed area. Some loss of liquid and norcamphor was only noticed in the longest experiment (> 1 week).

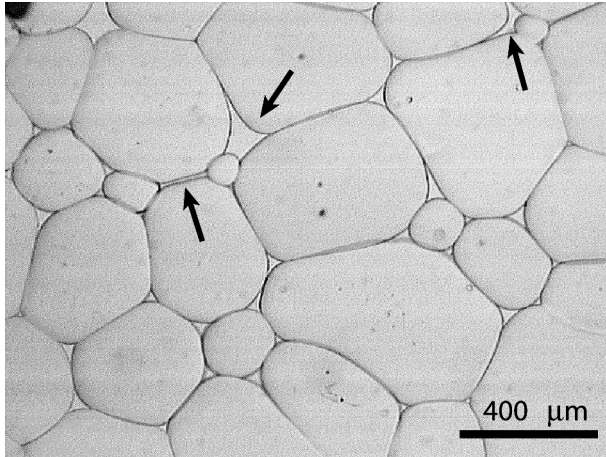


**Fig. 6.2.** Image of a statically recrystallizing norcamphor-ethanol aggregate. The grains form an equilibrated foam texture with smoothly curved grain boundaries. Liquid is situated in triangular three-grain triple junctions forming dihedral angles of approximately  $25^\circ$  with the norcamphor grains. Arrows point at disequilibrium features that form due to static grain growth. See also movie 2.05-3 on the enclosed DVD.

The whole apparatus was mounted on a microscope stage to observe the microstructural evolution in the sample. 756 x 512 pixel digital colour images were taken at regular intervals from 2 minutes to 2 hours, depending on the duration of an experiment, ranging from a few hours to more than 10 days. Liquid fraction was determined by directly measuring the liquid area with the image analysis software NIH image and is reported as vol. %.

## 6.3 Results

### 6.3.1 *Norcamphor-Ethanol experiments*

Samples were prepared by sandwiching the desired mix of fine-grained norcamphor and norcamphor-saturated ethanol directly between the glass plates and inserting the assembly into the apparatus. An effectively two-dimensional (only one layer of grains) equilibrated texture forms within a few hours of static annealing at room temperature. Grains have smoothly curved boundaries, perpendicular to the glass plates. At high (>10 vol. %) liquid fractions, grains that are surrounded by liquid are approximately spherical in shape without crystal facets. That indicates an effectively isotropic solid-liquid surface energy of the norcamphor (Walte et al., 2003). At lower melt fractions, the grains form a foam texture, with liquid mostly located at regular triangular inward-curving grain boundary triple junctions (Fig. 6.2). The geometry is close to the predicted equilibrium distribution with a low solid-liquid wetting angle of about  $25^\circ$  (e.g. von Bargen and Waff, 1986, Laporte 1994). However, occasional disequilibrium liquid pockets, such as larger patches or wetted grain boundaries, also occur as a result of continuous grain growth (Fig. 6.2) (Walte et al., 2003).

Experiments were prepared with an initially high liquid fraction of >10 vol. % (Fig. 6.3a). Norcamphor grains in contact with each other regularly form aggregates with welded grain boundaries (Fig. 6.4). This is energetically favourable for wetting angles above  $0^\circ$ , i.e., the ratio of solid-solid to solid-liquid surface energy is below two, so that aggregation of

grains lowers the total energy of the system (e.g. Stephensen and White, 1967, Jurewicz and Watson 1985).

During a single experiment the melt fraction always decreased within the observed area due to compaction of the sample and lateral extrusion of liquid that collected at the sides of the sample. This allowed for a continuous observation of the transition from high to low melt-fraction behaviour.

Experiments were conducted with “low” and “high” bulk strain rates of approximately  $10^{-6} \text{ s}^{-1}$  and  $10^{-5} \text{ s}^{-1}$ , respectively. Temperature was held constant at  $30 \pm 1 \text{ }^\circ\text{C}$  by room air conditioning, without additional heating or cooling.

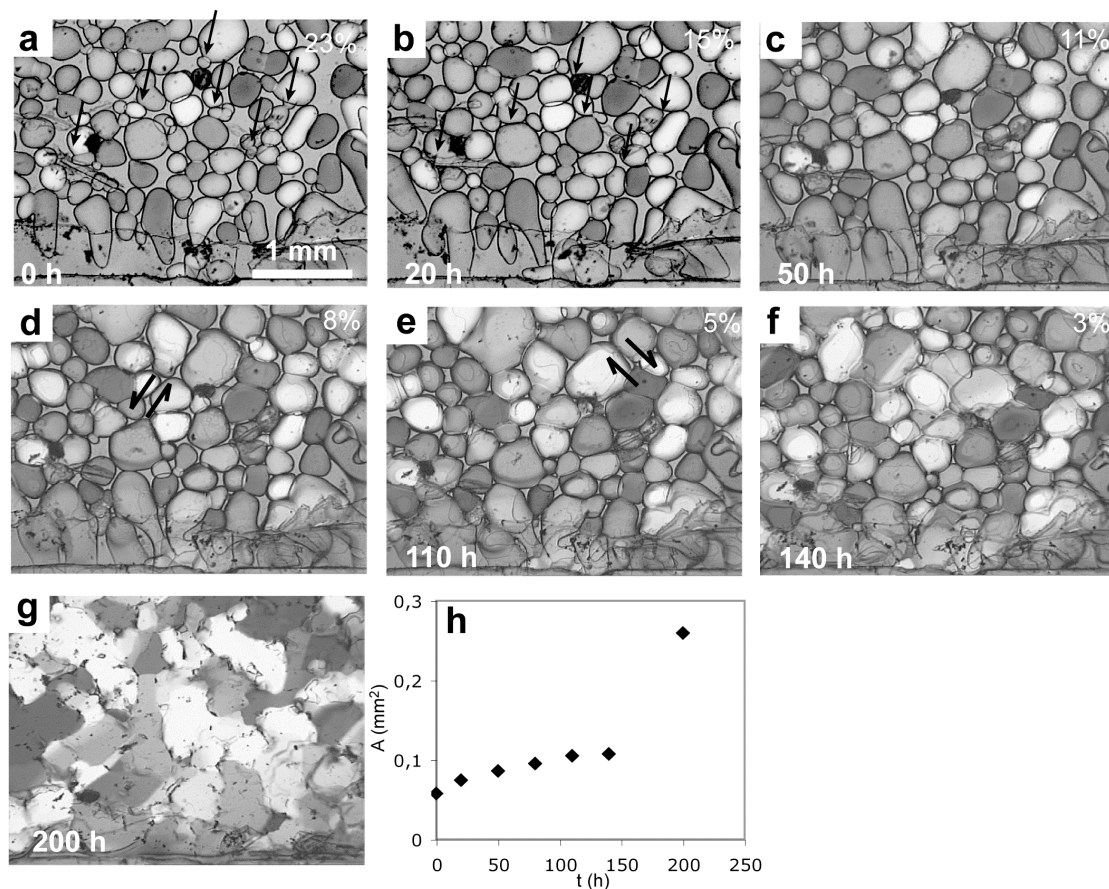


**Fig. 6.3.** Deformation of norcamphor crystals plus saturated ethanol liquid by bulk pure shear with a strain rate of  $\sim 2 \cdot 10^{-6} \text{ s}^{-1}$  (vertical shortening direction). **A-B:** Grain coarsening accommodated compaction with minor grain boundary sliding. Arrows indicate small grains that disappear and are replaced. **C:** Deformation is accommodated by granular flow. **D-E:** Localized grain boundary sliding in small shear zones while most of the grains are already locked. **F-G:** locking up of grain boundaries and grain boundary migration accommodated dislocation creep. The liquid fraction at this stage is nearly zero. Images were taken with partly crossed polarizers. **H:** Grain size versus time graph. See also movie 2.49-1-8 on the enclosed DVD.

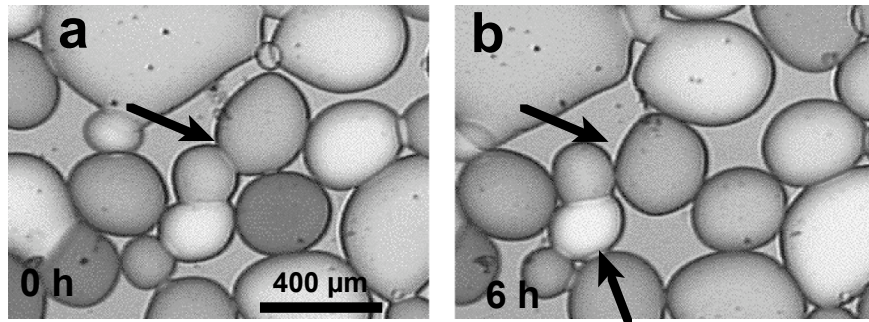


**Fig. 6.4.** Interplay of grain boundary welding and grain boundary sliding. The aggregate in the centre is destroyed as the upper grain is sheared off (see arrows). Notice the newly formed welded boundary in the lower part of **B** (lower arrow). Images were taken with partly crossed polarizers. See also movie 2.48-1-2 on the enclosed DVD.

### 6.3.1.1 “Low” strain rate deformation

The images of Fig. 6.3 represent more than 8 days of deformation at a strain rate of ca.  $2 \times 10^{-6} \text{ s}^{-1}$ . Initially, the sample deforms by grain compaction accommodated by a combination of grain boundary sliding–granular flow and grain coarsening (Fig. 6.3a-b). The grain coarsening is driven by the dissolution of small grains and simultaneous growth of large grains due to the differences in surface/volume ratio of different sized grains. This process is normally termed (liquid assisted) “static recrystallization” or “Ostwald ripening” (e.g. Evans et al., 2001). When a small grain disappears, a larger grain can slide into the remaining gap and occupy its space so that the static grain coarsening facilitates compaction (compare Figs. 6.3a-b). This mechanism, coupled with a complex grain rearrangement and minor grain boundary sliding, dominates the deformation in the beginning of the experiment. Dissolution–precipitation processes such as “contact melting” as reported by Means and Park (1994) were not observed and are probably of minor importance.

Grain boundary sliding is either distributed throughout the sample (granular flow) at a high liquid fraction exceeding ca. 8-9% or is localised in small, short-lived, often conjugate shear zones that occur at lower liquid fractions. During their activity, the shear zones have a locally stable liquid fraction as grains slide past each other (Fig. 6.3c-e). A de-activated shear zone often compacts by redistribution of the melt in the surrounding matrix. Welding of several grains into coherent clusters between the shear zones is another characteristic of this deformation/melt fraction stage (Fig. 6.3d-e, Fig. 6.4).

During progressive pure shear the liquid fraction decreases slowly due to an overall compaction of the grains and lateral expulsion of liquid towards the sides of the sample. The grain-scale liquid distribution at this stage is governed by opening and closing gaps between sliding grains, by liquid redistribution due to disappearing grains, and growing grains that

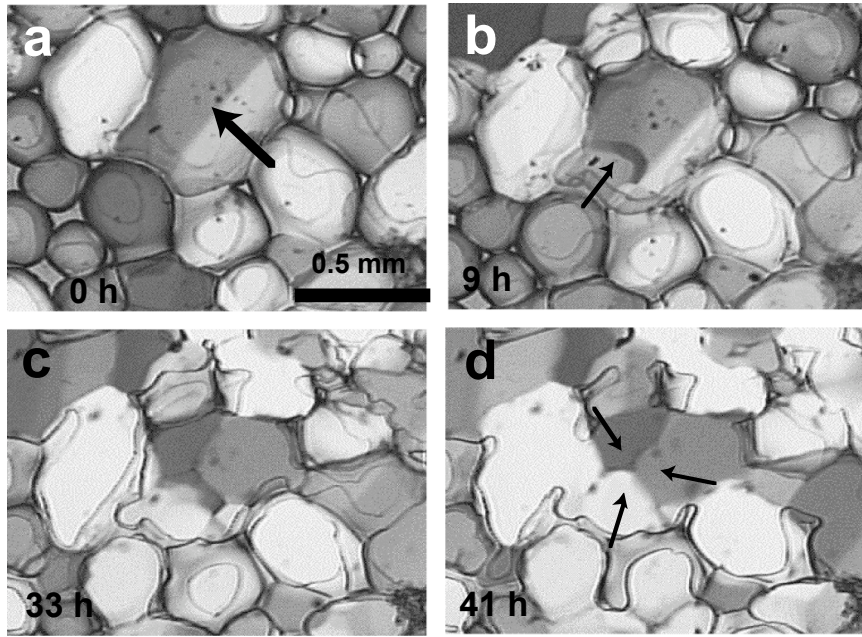


**Fig. 6.5.** Detail of the low strain rate experiment showing the development of a single grain (see arrow). Straight subgrain boundary in **A** migrates slowly outwards while a new curved subgrain boundary develops from below **B**. A second subgrain boundary develops (**C**) so that the grain eventually splits into three parts. The lower third becomes part of a larger bright grain. Images were taken with partly crossed polarizers. See also movie 2.49-1-8 on the enclosed DVD.

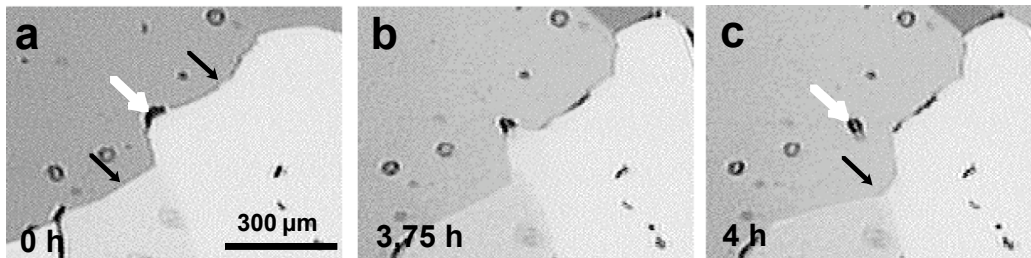


**Fig. 6.6.** "Regular pinning" in the grain boundary migration stage of a "low" strain rate experiment. **A-B**: A moving grain boundary (arrows) is pinned by a small liquid bubble. **C**: Eventually, the boundary detaches and leaves a round liquid inclusion (arrow). Images were taken with partly crossed polarizers. See also movie 2.33-1-4 on the enclosed DVD.

slide into cavities. As the grain size increases and the liquid fraction decreases, the relative effect of grain coarsening as an accommodation process for compaction decreases.

Below about 8 vol. % liquid fraction the deformation becomes more localized into shear zones and the grain boundary sliding is more and more inhibited by welded grain boundaries and the formation of larger grain clusters. Once the melt fraction falls below about 5 vol. %, there is a dramatic switch in microstructure and deformation mechanism (Fig. 6.3 f-g). Grain boundary sliding is absent as all grains are locked into one single framework. The grains are now deforming internally by crystal plastic deformation, probably dislocation creep (Bons, 1993, Herwegh and Handy, 1996). The grains develop undulose extinction, which regularly

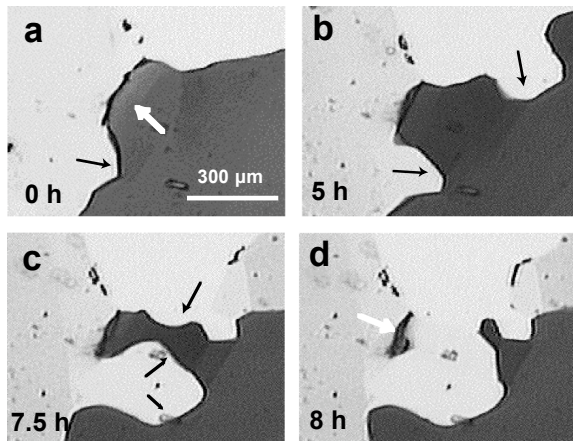


**Fig. 6.7.** "Irregular pinning" in a "low" strain rate experiment. The sweeping boundary cannot detach from a larger fluid patch as in Fig. 6.6. The sides swing around and leave a small island grain connected to a fluid inclusion (see arrows). Images were taken with partly crossed polarizers. See also movie 2.33-1-4 on the enclosed DVD.

localizes into newly formed subgrain boundaries usually oriented parallel to the axis of greatest compression (Fig. 6.5). Further rotational recrystallisation leads to the formation of new grains with high-angle boundaries (Fig. 6.5d).

At this stage, grain boundaries become very mobile, probably because grains are pressed against each other, possibly separated by a thin, mobility-enhancing liquid film. An unstable microstructure results as the grain boundaries begin to sweep other grains, and become irregular and amoebal in shape (Fig. 6.3g). The mean grain size increases rapidly (Fig. 6.3h). However, this fast grain boundary mobility is only reached once most of the liquid is expelled from the sample. As long as liquid is situated in triple junctions and between grain boundaries, the boundaries are prevented from migrating freely. Therefore liquid patches act as a pinning phase (c.f. Evans et al. 2001, Renner et al. 2002). Small remaining liquid pockets pin mobile grain boundaries for a limited time before the grain boundaries sweep over or around them and the liquid remains as round inclusions within grains (Fig. 6.6-7).

### 6.3.1.2 "High" strain rate deformation

The deformation behaviour and microstructure in the experiments with a "high" strain rate ( $\sim 10^{-5} \text{ s}^{-1}$ ) is generally similar to the "low" strain rate behaviour described above. We can also differentiate between compaction and granular flow at  $\square_{\text{bulk}} > 8 \text{ vol. } \%$  characterized by freely slipping grain boundaries and "low" melt-fraction grain boundary migration accommodated dislocation creep with welded non-sliding grain boundaries (Fig. 6.8). However, the transition between the granular flow regime and the grain boundary migration accommodated dislocation creep regime is more abrupt at about  $\square_{\text{bulk}} < 8 \text{ vol. } \%$ , compared to the low strain rate experiments, with less development of localized shear zones. Because of the higher strain rate, the surface energy driven grain coarsening is negligible for the high liquid-fraction deformation ( $\square_{\text{bulk}} > 8 \text{ vol. } \%$ ) compared to the low strain rate case. High liquid fraction

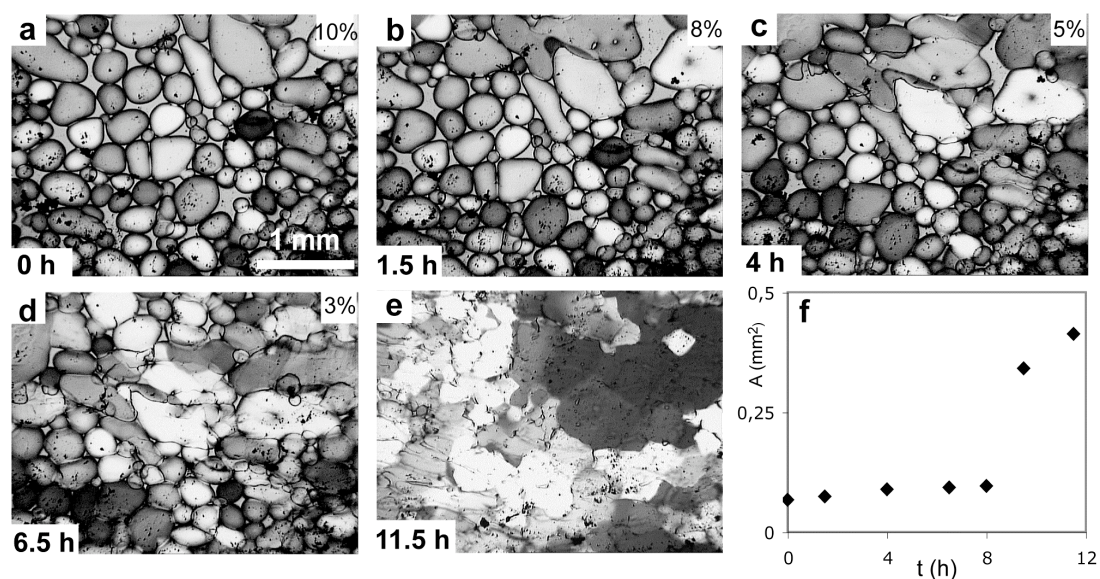


**Fig. 6.8.** Deformation of norcamphor crystals plus ethanol liquid by bulk pure shear with a “high” strain rate of ca.  $10^{-5} \text{ s}^{-1}$  (vertical shortening). **A-B:** Deformation is mainly by grain boundary sliding accommodated compaction. **C:** Onset of the locking stage of the grains into one coherent cluster (the GBS-L transition) suppressing GBS. Beginning of framework compaction. **D:** GBM starts in the melt-poor central region while remaining melt still pins the grain boundaries in the other parts. **E:** Further compression and liquid removal allows free grain boundary migration. The grain size is now significantly larger than during grain boundary sliding. Images were taken with partly crossed polarizers. **F:** Grain size versus time graph. See also movie 2.51-1 on the enclosed DVD.

deformation is therefore completely accommodated by grain rearrangement during compaction and grain boundary sliding (Figs. 6.8a-c).

### 6.3.2 $\text{KNO}_3\text{-LiNO}_3$ experiments

In the second type of experiment, the samples were prepared by complete melting of a  $\text{KNO}_3\text{-LiNO}_3$  mixture at  $300^\circ\text{C}$  and then letting it cool and crystallise between the glass plates, down to  $200^\circ\text{C}$ , at which temperature it was left to anneal for 24 hours. At this temperature all  $\text{LiNO}_3$  is completely molten and the solid phase is only composed of  $\text{KNO}_3$  grains. Due to a temperature gradient of about  $10^\circ\text{C}$  between the centre of the observation window (colder) and the metal housing (hot) most of the nitrate melt migrates out of the centre during static grain coarsening (Leshner and Walker, 1988) and collects at the side of the sample, so that the observed area of the sample has a very low starting melt fraction of approximately 1 vol. % (Fig. 6.9a). Because of the low melt fraction and the temperature gradient, the wetting angle is difficult to measure accurately but appears to be well below  $60^\circ$ .

Experiments were carried out in pure shear, at a “high” strain rate of about  $10^{-5} \text{ s}^{-1}$  and at a constant temperature of  $200^\circ\text{C}$ . At this temperature non-molten  $\text{NaNO}_3$ , a compound similar to  $\text{KNO}_3$  in its behaviour, displays rotational recrystallization and grain boundary migration recrystallization in the experiments of Thungatt and Humphreys (1981). However,

since the  $\text{KNO}_3$  grains in our experiments are comparably rigid, deformation is dominated by grain boundary sliding and internal deformation of the grains were only observed at a very low melt fraction (see below). During progressive deformation small conjugate shear zones develop throughout the sample (Figs. 6.9-6.11). Because of the initially very low melt fraction (<1 vol. %) the grain boundary sliding depends on a geometrical accommodation process. However, no diffusion or contact melting (cf. Means and Park, 1994) accommodation of the grain boundary sliding was observed but the sliding of grain boundaries was rather accommodated by local dilation and creation of new dynamic porosity in the shear zones. The newly created porosity is filled with melt that is drawn in from the matrix and from the edge of the sample. In this way the segregated melt originally located at the side is redistributed within the sample and the bulk melt-fraction of the sample is dynamically increased (Figs. 6.10, 6.12c). Shear zones rotate towards the shear plane and become inactive as new shear zones develop to take up the strain. The elevated porosity of an inactive shear zone is quickly destroyed by compaction and redistributed into newly formed shear zones (e.g. Fig. 10b-c). As the melt fraction rises during the experiment, the shear zones widen and deformation thereby becomes less localized and progress towards distributed granular flow (e.g. lower left region in Fig. 6.10d with a local melt fraction  $\phi_{\text{local}} \approx 9.5\%$ ). However, this progressive increase in melt fraction is only possible, if a sufficiently large melt reservoir is available at the side of the sample that can be sucked into the aggregate during deformation. If the melt fraction cannot increase freely, deformation stays localized in GBS shear zones and the undeformed regions are often characterized by a flattening of the crystals, possibly by diffusional creep, or by anomalous fast grain growth (Fig. 6.11). This stage of framework deformation at which grains lock and the onset of internal crystal plastic deformation is only observed in areas of the samples with a very low melt-fraction. This is because the low wetting angle of the melt inhibits grain welding and clustering, and because the dilatant shear zones counteract compaction and complete liquid expulsion.

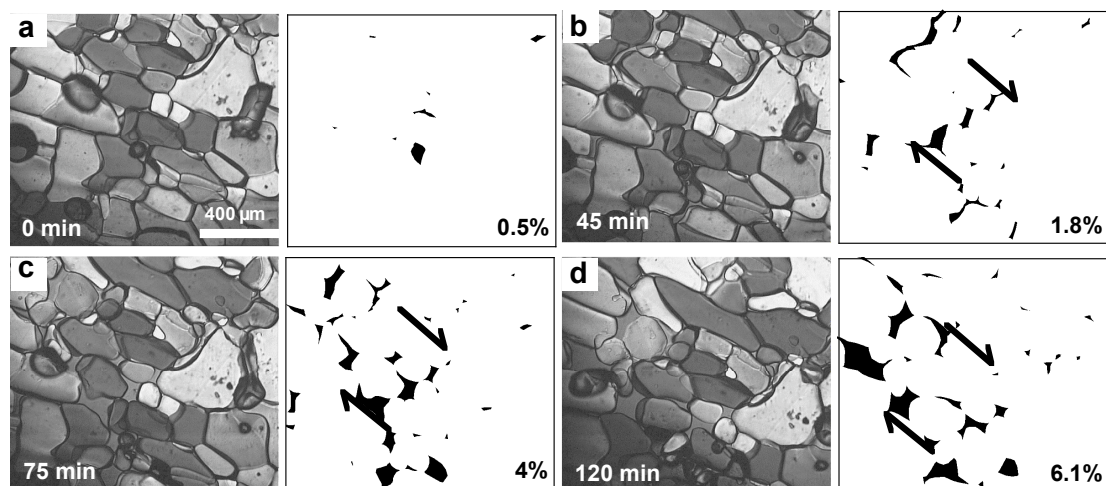


**Fig. 6.9.** Nitrate deformation experiment with a bulk pure shear of approx.  $10^{-5} \text{ s}^{-1}$  (vertical compression) Binary images trace the liquid evolution, numbers give the melt vol.%. **A:** Potassium nitrate aggregate before deformation with very low porosity. **B-D:** Deformation localizes into a small shear zone that deforms by GBS. Opening gaps are filled with melt that is drawn in from the outside. The dynamic porosity in the shear zone has now significantly increased to approximately 10%, while the matrix has retained a low porosity. Images were taken with partly crossed polarizers. See also movie 2-3 on the enclosed DVD.

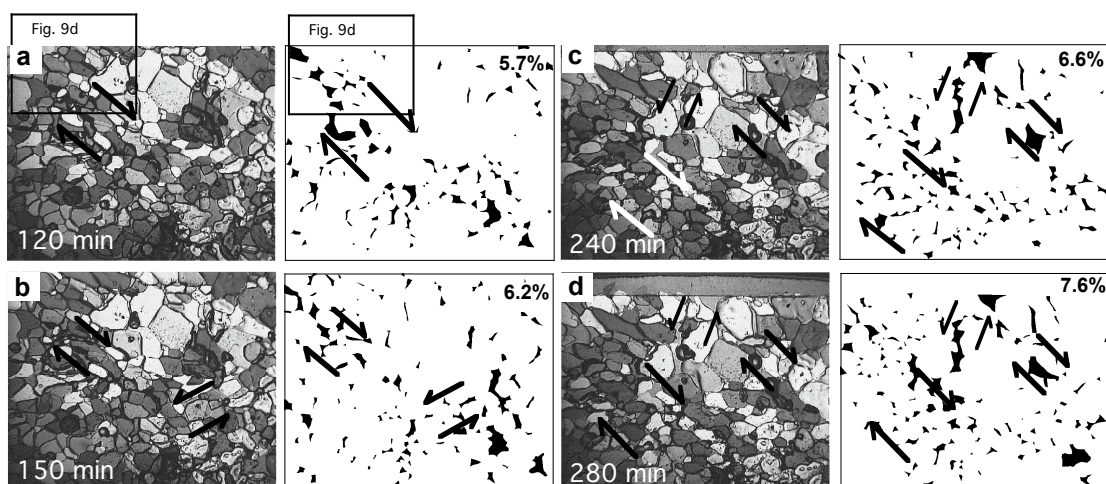


**Fig. 6.10.** Nitrate deformation experiment, continued from Fig. 9 with a lower magnification. Observed area of Fig. 9 is marked in **A**. Binary images trace the liquid evolution, numbers give the melt vol.%. Aggregate deforms by conjugate GBS shear zones. The melt-fraction in the observed area rises during progressive deformation, and the deformation develops from localized shear zones towards distributed granular flow. See also movie 2-4 on the enclosed DVD.

### 6.3.3 Evolution of the liquid-fraction in the analogue experiments

Figure 6.12 shows the evolution of the liquid fraction as a function of the bulk shortening of the norcamphor-ethanol experiments (Fig. 6.12a-b) and the  $\text{KNO}_3\text{-LiNO}_3$  experiments (Fig. 6.12c). For the analysis of the norcamphor experiments starting images were chosen that contain similar liquid fractions of  $\sim 10 \text{ vol. } \%$  and the shortening was calculated in relation to these starting images. The curves of the low strain rate (Fig. 6.12a) and the high strain rate

(Fig. 6.12b) experiment show a very similar liquid versus strain evolution in the norcamphor-ethanol system. In the beginning, deformation is dominated by compaction, until at around 8.5 vol. % liquid fraction (10% shortening) the deformation is dominated by liquid assisted granular flow. The subsequent flattening of the liquid curve until a bulk shortening of 30-35% represents temporary inefficient liquid segregation during granular flow. At that stage, below a liquid fraction of ca. 8 vol. %, liquid segregation picks up again, when norcamphor grains reach complete locking (high strain rate) or partial locking combined with localised grain boundary sliding (low strain rate) (Fig. 6.12a-b).

The liquid evolution and the microstructural evolution of the nitrate experiments display the opposite trend during progressive pure shear deformation compared to the norcamphor-ethanol experiments. While the latter evolve from high to low liquid-fraction with granular flow to localized GBS and framework deformation (Fig. 6.12a-b), the nitrate experiments evolve from low to high liquid-fraction with localized GBS deformation in the beginning towards a high liquid-fraction with granular flow. However, although the systems behave so differently, the liquid-fraction of the transitions from localized GBS deformation to distributed GBS deformation (granular flow) is in both systems between 8-10 vol. % liquid.

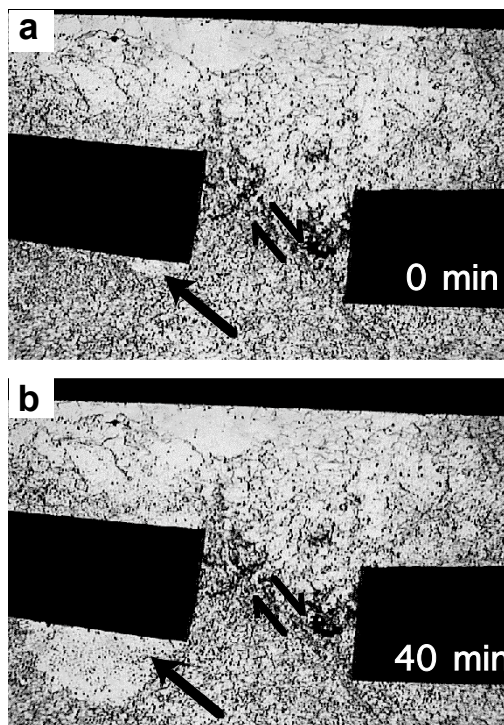


**Fig. 6.11.** Nitrate deformation experiment with a low bulk melt fraction (estimated to be < 3 vol. %). Black bodies are rigid “micro boudins” made out of 0,1 mm thick metal foil. Deformation is by localized GBS with a small shear zone that separates the two “boudins”. Melt fraction in the shear zone is raised, while the matrix compacts, probably by dislocation creep. Fast, anomalous grain growth (see arrow) overgrows large parts of the fine-grained matrix. Width of view is approx. 1 cm. See also movie 38-B on the enclosed DVD.

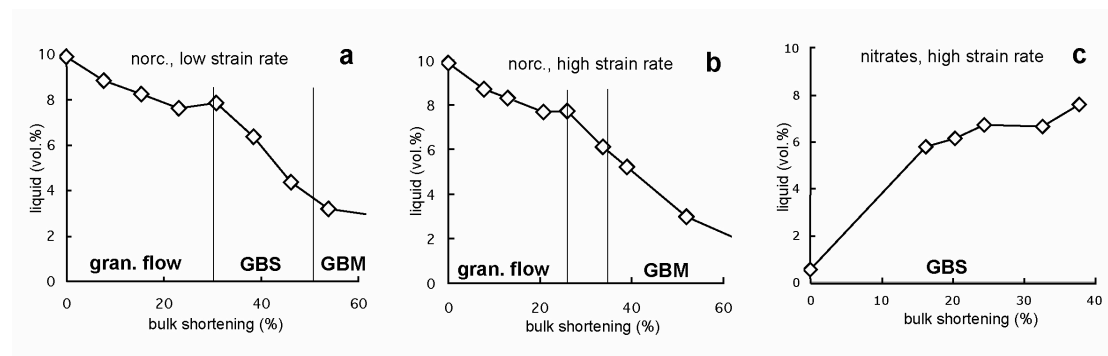


**Fig. 6.12.** Evolution of the liquid fraction in the norcamphor–ethanol experiments and the  $\text{KNO}_3$  –  $\text{LiNO}_3$  experiment versus bulk strain. **A:** Development of the liquid fraction in the low strain rate experiment. Time displayed is 80 hours. **B:** Liquid evolution in the “high” strain experiment. Microstructural transitions are marked on the plot. The bulk shortening is calculated in relation to the initial stage at approximately 10% liquid. Time displayed is 5 hours. **C:** Melt-fraction evolution in the nitrate experiment shown in Figs. 9-10.

## 6.4 Discussion

### 6.4.1 The deformation behaviour of liquid bearing analogue experiments

The deformation behaviour of all described analogue systems can be summarized in three general modes of deformation: At “high” liquid-fraction ( $\varphi_{\text{bulk}} > 8-10$  vol. %) deformation is by distributed granular flow, at “moderate” liquid fraction ( $\varphi_{\text{bulk}} < 8-10$  vol. %) deformation is by localized GBS with compacting grain clusters in between, and at a “low” liquid fraction ( $\varphi_{\text{bulk}}$  varies strongly between different experiments) an interlocking granular framework is deformed. The following Sections discuss the occurrence and implications of these different deformation regimes and propose a classification for solid-liquid systems that helps to predict their deformation behaviour.

#### 6.4.1.1 Granular flow and localized grain boundary sliding

Grain boundary sliding (GBS) is used here to characterize the grain-scale deformation mechanism of grains moving relative to each other, which can be either localized in a sample, e.g. in shear zones, or distributed throughout the aggregate, which we call granular flow. The term granular flow originally comes from soil mechanics and sedimentology but has been applied previously for non-localized distributed deformation by grain-boundary sliding in *in-situ* experiments of partially-molten rock analogues (Park and Means, 1996). Granular flow and grain boundary sliding of partially-molten rocks is considered as a potentially important deformation mechanism in nature (e.g. Rutter, 1997, Paterson, 2001, Rosenberg, 2001, Mecklenburgh and Rutter, 2003). A rheological model for grain boundary sliding of partially-molten rocks was put forward by Paterson (2001). In this model, diffusion and reactions are

thought to solve the compatibility problems of grains sliding past each other, so that diffusion becomes rate-controlling. The rheological stress–strain rate equations therefore yield the theoretical stress exponent of  $n=1$  for diffusional creep. The other extreme is the unconstrained flow of granular material like sand, that ideally behaves elasto-plastically (e.g. Viggiani et al. 2001) with an undefined stress exponent. Experimental investigations of deformation by granular flow in partially molten granitic rocks and synthetic quartz aggregates (e.g. van der Molen and Paterson, 1979, Rutter and Neumann, 1995, Mecklenburg and Rutter, 2003) have resulted in intermediate stress exponents, such as  $\sim 3.5$  for quartz plus albite-quartz melt (Mecklenburg and Rutter, 2003), indicating that some other mechanism than diffusion is rate controlling. Mecklenburg and Rutter (2003) have suggested fracturing and intra-grain microcracking for higher strain rates and the destruction of welded grain boundaries (inter-grain microfracturing) for low strain rates as possible rate controlling mechanisms. The occurrence of the latter process has been confirmed by our observations. In our experiments, diffusional material transfer was not observed, and grain boundary sliding was enabled by local dilatancy and influx of liquid.

Grain boundaries are continuously welded and separated in our norcamphor-ethanol experiments (Fig. 6.4) and this process may be controlling the rate of GBS deformation. Deformation dominated by grain boundary sliding without diffusion accommodation ( $n > 1$ ) (Mecklenburgh and Rutter, 2003) can only be active if a freely moving liquid is present to provide the necessary geometric porosity for grains to slide past each other. Since the liquid is drawn from the surrounding matrix into the areas deforming by GBS, the bulk liquid fraction geometrically determines the degree of deformation localization: At a “high” bulk liquid fraction exceeding ca. 8-10 vol. % in our experiments and in the analogue experiments of Park and Means (1996), the whole aggregate can deform by granular flow without localization of the deformation. At lower bulk liquid fractions, GBS is localised into shear zones, separating low strain grain aggregates. Within the shear zones, the local liquid fraction is equal or higher than the 8-10% threshold for GBS, which is achieved by drawing liquid from the low strain aggregates. Spacing and size of shear zones is therefore determined by bulk liquid fraction and mobility of the liquid. The threshold liquid fraction for GBS, ca. 8-10% in our experiments, depends on grain shape. The threshold can be lower when grains are elongate and aligned, as in the experiments of Park and Means (1996). Because of the shape or geometric control, we call the threshold to enable GBS the **grain shape percentage (GSP)**. If the bulk liquid fraction of a liquid-bearing aggregate is larger than GSP ( $\square_{\text{bulk}} > \square_{\text{GSP}}$ ), flow is by pervasively distributed granular flow. If the bulk liquid fraction is lower than GSP ( $\square_{\text{bulk}} < \square_{\text{GSP}}$ ), GBS shear zones with a local liquid fraction  $\square_{\text{sz}} \geq \text{GSP}$  are formed. This dependence of the localization of deformation on the liquid-fraction is evident from our nitrate

experiments: The bulk liquid-fraction in Fig. 6.10e is 8 vol. %, just below  $\phi_{\text{GSP}}$ , the deforming regions accordingly take up most of the aggregate. At earlier stages  $\phi_{\text{bulk}}$  was lower and the deformation thus more localized.  $\text{GSP} \leq 10$  vol.% in 2-dimensional experiments. In 3-dimensional reality, GSP is expected to be much higher, probably around 25-30 vol. %. This can be derived from comparing the pore area fraction of a closest circle packing in 2-D to the pore volume fraction of closest sphere packing in 3-D which is ca. 9 vol. % and 26 vol. % respectively.

#### 6.4.1.2 Grain boundary migration accommodated dislocation creep

A common observation of both the norcamphor-ethanol and in the partially-molten nitrate experiments was the anomalous grain growth at a melt fraction below 5-8 vol. % and below  $\sim 1$  vol. %, which occurred during framework deformation and lead to a significant increase of the grain size. However, this increase of grain size during deformation appears to be different from previously described processes of abnormal or discontinuous grain growth (Atkinson, 1988, Evans et al., 2001, and references therein) or exaggerated grain growth (Vernon, 1976), in which single larger grains grow at the expense of smaller matrix grains, since the latter occurred during static recrystallization. The microstructures observed during grain boundary migration in the norcamphor experiments correspond to the dislocation creep regime 3 of Hirth and Tullis (1992) and the GBM regime of Stipp et al (2002a, b) that are characterized by grain boundary migration with only minor subgrain rotation recrystallization. Although these regimes have been defined for non-molten deforming quartzite, our observation that the strong grain boundary migration only starts when nearly all melt has been removed from the sample fits well with the description of regime 3, especially as a very low melt fraction  $< 1\%$  was reported for some of the experiments of Hirth and Tullis (1992). However, the very high mobility of the grain boundaries and the dramatic increase of the grain size are unusual for the unmolten GBM regime of Hirth and Tullis (1992). The sudden grain growth that was observed in some of the nitrate experiments was even more pronounced than in the norcamphor experiments. This grain size increase is also probably the result of grain boundary migration accommodated dislocation creep, since the temperature of deformation ( $200^\circ\text{C}$ ) in our experiments lies within the range of GBM recrystallization in  $\text{NaNO}_3$  reported by Thungatts and Humphreys (1981). The strong increase in grain size of both sets of experiments during framework deformation poses the question, whether such a dynamic increase of grain size can also be expected in natural systems deforming with a low percentage of melt. One possible indication for such a process was given by Stipp et al. (2002b). They reported a dramatic increase in grain size of a deformed quartzite adjacent to the contact of the Adamello pluton (Italian Alps), which they could not explain satisfactorily

(Stipp et al., 2002b). Although the quartzite layers do not contain visible traces of melt, the pluton and the surrounding rocks were partially molten during the deformation (Stipp pers. comm., 2004). It is therefore possible, that small traces of melt were present in the quartzite layers during deformation that lead to a similar dynamic grain-size increase as observed in our experiments. A very large grain size is also a characteristic of high-temperature quartz ribbon mylonites (e.g. Hippert et al., 2001), which could possibly also be connected to the presence of a melt or metamorphic fluid during deformation. Urai (1983) reported a high grain-boundary mobility of wet bischofite during GBM accommodated deformation, which he explained by a very thin liquid film between the grain-boundaries. A very high grain boundary migration rate and increase of grain size was also reported by Rosenberg and Handy (2001) in analogue experiments using norcamphor plus a norcamphor-benzamide melt in pure shear.

According to Mecklenburgh and Rutter (2003) melt-present dislocation creep is probably not very important in nature because of the relatively high strength of quartz crystals at natural temperatures and strain rates. However, the examples above show, that it would be very difficult to distinguish the microstructures between solid regime 3 deformation and originally melt present dislocation creep deformation at similar temperatures. Most studies on the deformation behaviour of partially molten rocks have also been performed on migmatites with a higher melt fraction that resulted in different deformation mechanisms such as cataclastic flow (e.g. Brown and Rushmer, 1997). An indication for melt-present dislocation creep could be an unusually large grain size in dynamically recrystallized rocks as reported by Stipp et al. (2002b) or the unusual grain size in high-temperature quartz ribbon mylonites. A promising approach is the search for monomineralic melt pseudomorphs, that have been found and described in natural rocks at the grain-scale, partly in dynamically recrystallized rocks, that present strong evidence for the former presence of melt (Rosenberg and Riller, 2000, Sawyer, 2001, Marchildon and Brown, 2002). More detailed fieldwork, especially in low-melt fraction rocks that deformed above the solidus, is needed to better constrain the importance of melt-present deformation in the GBM regime and the occurrence of an enhanced dynamic grain growth.

#### ***6.4.2 The grain boundary sliding – grain boundary locking (GBS-L) transition: A microstructural critical melt percentage***

Arzi (1978) suggested the existence of a critical threshold in partially molten systems, the rheological critical melt percentage (RCMP), that marks a transition between essentially solid behaviour to much weaker behaviour dominated by the melt phase. The RCMP concept predicts a sharp drop in strength at a bulk melt fraction of about  $\square_{\text{bulk}} \approx 20 \pm 10 \%$  melt.

Vigneresse et al. (1996) and Vigneresse and Tikoff (1999) extended and modified the concept by arguing that there is a difference between a progressively melting system (increasing melt fraction) and a crystallising system (decreasing melt fraction) and defined four thresholds by utilizing percolation theory. In the crystallising case they defined the rigid percolation threshold (RPT) at  $\phi_{\text{bulk}} \approx 45$  vol.% and the particle locking threshold (PLT) at  $\phi_{\text{bulk}} \approx 25-28$  vol.%. The PLT is analogous to the RCMP. All authors have in common that they based their theory on the consideration that once a geometric stress-supporting framework of rigid grains has been established, the rheology of the system should change dramatically. The melt-fraction at the transition between solid and liquid-dominated behaviour is argued to depend mainly on geometric considerations of melt fraction and particle shape.

Although the existence of a mechanical RCMP is controversial (e.g. Bagdassarov and Dorfman, 1998, Rosenberg, 2001, Renner et al. 2000, ), the microstructural transition between liquid dominated behaviour at a high liquid fraction (suspension flow, granular flow, GBS) and solid framework dominated behaviour (GBM accommodated dislocation creep, diffusion creep/"contact melting") is clearly taking place as a function of liquid fraction as has been observed in the *in-situ* analogue experiments of Park and Means (1996) and in this study. The granular-flow and localized GBS dominated behaviour in our experiments corresponds to the liquid-dominated regime that was predicted above the RCMP and the behaviour dominated by dislocation creep in our experiments corresponds to the solid-dominated regime predicted below the RCMP. The generally sharp transition in our experiments is marked by the locking of grain boundaries and occurs as a function of liquid fraction. To characterize this important microstructural change of behaviour, we propose a new microstructurally defined transition, the grain boundary sliding – grain boundary locking transition (GBS–L), that marks the transition between essentially liquid dominated behaviour and solid framework dominated behaviour. In the “grain boundary sliding” regime we include both the distributed granular flow and localised GBS deformation in shear zones, as long as the bulk strain is accommodated by sliding of grains past each other. The “grain boundary locking” regime includes all types of framework deformation processes such as GBM accommodated dislocation creep (norcaphor experiments) and diffusion creep where the grains are interlocking to form a coherent framework and GBS does not occur or plays only a minor role. The “GBS–L threshold” ( $\phi_{\text{GBS-L}}$ ) is defined as the bulk liquid fraction of the sample at which the microstructural transition occurs. Note that there is an important difference between the RCMP and the newly defined  $\phi_{\text{GBS-L}}$ . The RCMP is a rheologically defined threshold that marks a dramatic weakening above a certain melt fraction, while the GBS–L threshold marks an important transition in deformation mechanism and segregation behaviour (see below) at a certain liquid fraction, that may or may not coincide with a sharp rheological change of

behaviour (the rheology of *in-situ* analogue experiments cannot be measured, yet). Another important difference to the rheological threshold models, that generally assume an evenly distributed liquid fraction, is that the  $\varphi_{\text{GBS-L}}$  is not fixed, but can vary significantly between systems.  $\varphi_{\text{GBS-L}}$  is not system-independent. In the “high” strain rate experiments with norcamphor-ethanol  $\varphi_{\text{GBS-L}}$  is at about 8 vol. % liquid, while  $\varphi_{\text{GBS-L}}$  is around 5 vol. % in the “low” strain rate experiments. In contrast to that, our nitrate deformation experiments have shown that localized grain boundary sliding can be active even at a very low liquid fractions, with  $\varphi_{\text{GBS-L}} < 1$  vol.%.  $\varphi_{\text{GBS-L}}$  therefore depends on the system of interest and can even change within a single system depending on the conditions of deformation. The critical point for the GBS–L transition is whether a stable framework is established that can support the applied stress without or with only minor relative movement between the elements that constitute the framework. To better characterize the magnitude and variation of  $\varphi_{\text{GBS-L}}$ , we have to consider the different parameters of our analogue systems that determine and influence  $\varphi_{\text{GBS-L}}$ . In the norcamphor-ethanol GBS regime spontaneous welding and clustering between adjacent norcamphor grains is energetically favourable and probably acts as a rate limiting mechanism for GBS deformation. The total work necessary for continuous grain boundary sliding in addition to overcoming frictional forces is therefore the work necessary to locally break the solid-solid grain boundaries, which is the product of the work needed to separate one grain boundary times the number of boundaries. The number of welded grain boundaries and the ratio of the solid-solid to solid-liquid boundary area in a sample are directly dependent on the liquid fraction, so that the work per strain increment of granular flow increases with decreasing liquid fraction. Thus, the change in deformation behaviour from grain boundary sliding to framework deformation occurs at that liquid fraction at which the strain energy rate for maintaining GBS equals or exceeds the strain energy rate for framework deformation. Several parameters should influence the magnitude  $\varphi_{\text{GBS-L}}$ :

1. **Solid strength and liquid viscosity:** A strong solid phase with a relatively low viscosity liquid facilitates GBS and therefore lowers  $\varphi_{\text{GBS-L}}$  (e.g. nitrate experiments), compared to a system with a weaker solid phase with a relatively higher viscosity liquid which facilitates framework deformation and thereby raises  $\varphi_{\text{GBS-L}}$  (e.g. norcamphor experiments). The ratio of solid strength to liquid viscosity can change in a system as a function of strain rate (the strain rate sensitivity) and temperature, thereby changing  $\varphi_{\text{GBS-L}}$ .
2. **The bonding strength of grain boundaries:** This is probably a function of the solid-solid surface energy, the wetting angle, and the relative liquid pressure. A wetting liquid (= low wetting angle  $< 60^\circ$ ) will facilitate dynamic wetting and breaking of

grain boundaries so that  $\square_{\text{GBS-L}}$  is lowered compared to a similar system with a non-wetting liquid (= high wetting angle  $> 60^\circ$ ). Besides the wetting characteristic of the liquid, the relative liquid pressure is of importance for breaking of grain boundaries and creating dynamic porosity. Temporary liquid overpressure is expected to facilitate breaking of grain boundaries, thereby lowering  $\square_{\text{GBS-L}}$ .

3. **Grain size:** In grain size sensitive framework deformation (liquid-assisted diffusion creep),  $\square_{\text{GBS-L}}$  is raised by a decreasing grain size.
4. **Permeability and viscosity:** To create localized shear zones, liquid has to move a certain distance along a hydraulic head into the shear zones. This migration from the matrix into the shear zones is a function of liquid viscosity and matrix permeability (see Holtzman et al. 2003a)

In summary, our results indicate that although the geometric possibility of a rigid framework is necessary for a critical threshold, it is not sufficient. The RCMP at  $20 \pm 10\%$  melt (Arzi, 1978) and the PLT at 25-28% melt (Vigneresse et al., 1996) therefore represent an upper boundary for critical behaviour of partially molten systems. These geometric thresholds are comparable to our  $\square_{\text{GSP}}$  in three-dimensional systems, and therefore probably represent the transition between granular flow to either localized GBS (in most systems) or directly to framework deformation in special circumstances (e.g. in the “high” strain rate norcamphor–ethanol experiments, see below). The actual critical GBS-L threshold for a given system is a function of several parameters, which are given above.

### 6.4.3 Segregation of liquid

Efficient melt segregation at melt-fractions above the RCMP is predicted to occur by compaction and filter pressing, whereas only restricted segregation occurs below the RCMP once a solid framework is established (Arzi, 1978). Interestingly, our results indicate the opposite. The liquid-fraction evolution of the experiments show that segregation of liquid per strain increment is significantly slower or even reversed (in the nitrate experiments) in the granular flow regime, while liquid segregation is efficient in the dislocation creep regime (Fig. 6.12). This different segregation behaviour above and below the GBS-L transition can be explained by the peculiarity of grain boundary sliding. A key for enabling this deformation mechanism to operate without the geometrically necessary accommodation by diffusion is either the existence or the creation of sufficient porosity (liquid fraction) to allow the grains to slide past each other, i.e. the  $\square_{\text{GSP}}$  defined above has to be locally approached or overstepped. The bulk liquid fraction for GBS can be lower if deformation, and therefore porosity, is localized. A system like the molten nitrates will therefore keep the liquid in the deforming

regions (e.g. the shear zones) as long as  $\sigma_{\text{GBS-L}}$  is overstepped. Once a stress-supporting framework is established at  $\sigma_{\text{bulk}} < \sigma_{\text{GBS-L}}$ , the liquid is easily pressed out if there is a liquid sink available as in our experiments (the unconfined edge of the sample). In summary, the liquid or liquid will reside, or will be drawn to areas deforming *above*  $\sigma_{\text{GBS-L}}$ , and will be segregated from areas deforming *below*  $\sigma_{\text{GBS-L}}$ .

The described liquid concentration in GBS shear zones up to  $\sigma_{\text{GSP}}$  is a grain scale process depending on the grain shape and, possibly, the grain size of the solid-liquid system in question. It should be noted that this process can be expected to occur in nature at similar length scales as in our experiments depending on the grain size. Therefore, we do not expect our experiments to be an analogue for melt collection in large (crustal-) scale shear zones, that were suggested for large-scale melt transport in the crust (Handy et al. 2001) or in the mantle (Holtzman et al. 2003a, b).

#### **6.4.3 The behaviour of partially molten systems during deformation**

Combining the two concepts of the GBS-L threshold ( $\sigma_{\text{GBS-L}}$ ) and the liquid threshold for unconfined GBS deformation ( $\sigma_{\text{GSP}}$ ), we are now able to classify the behaviour of an ideal liquid-bearing system and attempt to explain the three deformation regimes observed in the experiments (granular flow, localized GBS, framework deformation). The “ideal system” is used here similarly to the definition of an ideal system used for considering the static liquid distribution in “equilibrium” situations (Bulau et al., 1979, von Bargen and Waff, 1986, Laporte et al., 1997, Becker et al., 2003). An ideal system consists of a single solid plus a single liquid phase, that display a uniform solid-solid and solid-liquid surface energy at grain and phase boundaries. It follows that the system has a single wetting angle at all solid-solid-liquid triple junctions (Bulau et al., 1979) and the grains approach a spherical shape when they are completely surrounded by the liquid. It has the further consequence, that these systems can be expected to have a single  $\sigma_{\text{GSP}}$  and  $\sigma_{\text{GBS-L}}$ , since the first is a function of the geometry of grains and the second a function of the parameters given above, which include solid strength and wetting angle. The norcamphor-ethanol system is an example of a near ideal system because of the circular shape of the crystals surrounded by ethanol, while the potassium nitrate forms crystal facets in contact with liquid like nearly all rock forming minerals and is therefore non-ideal. The deformation behaviour of an ideal system can be classified according to the relative magnitudes of the two thresholds and the bulk liquid fraction:

1.  $\varphi_{\text{GBS-L}} = \varphi_{\text{GSP}}$ :
  - a.  $\varphi_{\text{bulk}} \geq \varphi_{\text{GBS-L}} = \varphi_{\text{GSP}}$ : The system deforms by compaction and distributed granular flow
  - b.  $\varphi_{\text{bulk}} < \varphi_{\text{GBS-L}} = \varphi_{\text{GSP}}$ : The system deforms by a process of distributed framework deformation (dislocation creep, diffusion creep)
2.  $\varphi_{\text{GBS-L}} < \varphi_{\text{GSP}}$ :
  - a.  $\varphi_{\text{bulk}} \geq \varphi_{\text{GSP}}$ : The system deforms by compaction and distributed granular flow
  - b.  $\varphi_{\text{GBS-L}} < \varphi_{\text{bulk}} < \varphi_{\text{GSP}}$ : The system deforms by grain boundary sliding, that is localized into shear zones. Liquid is transferred from the matrix into the shear zones so that the shear zones have a *local* liquid fraction equal to the geometric threshold ( $\varphi_{\text{SZ}} \geq \varphi_{\text{GSP}}$ ) and the matrix has a *local* liquid fraction approaching  $\varphi_{\text{GBS-L}}$ . The width of the shear zones and the spacing between them is a function of  $\varphi_{\text{bulk}}$ . The clusters between the shear zones deform (compact) by minor framework deformation, but the bulk strain is dominated by the GBS shear zones.
  - c.  $\varphi_{\text{bulk}} < \varphi_{\text{GBS-L}}$ : The system deforms by framework deformation.

Note that the hypothetical case of  $\varphi_{\text{GBS-L}} > \varphi_{\text{GSP}}$  is impossible since the formation of a geometric framework is a prerequisite for framework deformation. An example for a “mode 1” system is the “high” strain rate norcamphor-ethanol experiment. The observation of a direct transition from granular flow at  $\varphi_{\text{bulk}} > \varphi_{\text{GBS-L}}$  (mode 1a) to framework deformation at  $\varphi_{\text{bulk}} < \varphi_{\text{GBS-L}}$  (mode 1b) with only limited localization in shear zones suggests that  $\varphi_{\text{GBS-L}} \approx \varphi_{\text{GSP}}$ . Examples for a “mode 2” system are the nitrate experiments and the “low” strain rate experiments with norcamphor-ethanol, that progress through the stages 2a-c with a decreasing liquid fraction.

The advantage of this classification is that the deformation behaviour of any system (granular flow, localized GBS, or framework deformation) can be directly inferred if  $\varphi_{\text{GSP}}$  and  $\varphi_{\text{GBS-L}}$  are known. As an example for the geological implications of the two different deformation paths, consider two hypothetical liquid-bearing systems with an initial equal bulk liquid fraction smaller than GSP, e.g.  $\varphi_{\text{bulk}} = 5\% < \varphi_{\text{GSP}}$ . The GBS-L threshold of system #1 is assumed to be higher than  $\varphi_{\text{bulk}}$  ( $\varphi_{\text{bulk}} < \varphi_{\text{GBS-L}}$ ), while the GBS-L threshold of system #2 is assumed to be lower than  $\varphi_{\text{bulk}}$  ( $\varphi_{\text{bulk}} > \varphi_{\text{GBS-L}}$ ). The difference in  $\varphi_{\text{GBS-L}}$  between the two systems can be explained, for example, by a greater strength of the grains of the first system. According to our classification, #1 is in the 1b or 2c deformation stage and system #2 is in the 2b deformation stage. Let us further assume, that the solid-liquid wetting angle in both systems is identical and below  $60^\circ$ , so that the appearance of the two systems before the

deformation is very similar with a static liquid distribution that is determined by the wetting angle and the grain coarsening rate (von Bargen and Waff, 1986, Walte et al., 2003). However, when the systems experience deformation, they behave very differently: System #1 is unstable. Small initial liquid fluctuations or stress inhomogeneities will be quickly enhanced into localized shear zones that deform by GBS leaving coherent clusters in between. The liquid fraction in the shear zones is raised to  $\varphi_{\text{local}} \geq \varphi_{\text{GSP}}$  (~8-10% in two dimensions), while the clusters compact slightly to transfer liquid to the shear zones (until  $\varphi_{\text{local}} \leq \varphi_{\text{GBS-L}}$ ). On the other hand, system #2 deforms from the beginning by distributed framework deformation (e.g. by dislocation creep) since  $\varphi_{\text{bulk}} < \varphi_{\text{GBS-L}}$ . Small initial liquid fluctuations are equalized during deformation as long as the fluctuations do not overstep  $\varphi_{\text{GBS-L}}$  (this could happen e.g. if the wetting angle is above 60° so that there is a surface energy driven liquid collection in large liquid batches (Jurewicz and Watson, 1985)). If there is no local liquid-sink available (such as the unconfined edge of our samples during deformation) there is no liquid localization. The interesting part of this *Gedankenexperiment* is, that there are no microstructural criteria to predict the behaviour of the two systems, if  $\varphi_{\text{GBS-L}}$  is not known at the specific conditions of deformation, i.e. the bulk strain rate, the temperature and the strength of the grains and the grain boundaries. It is therefore crucial to determine  $\varphi_{\text{GBS-L}}$  of natural partially-molten systems at the conditions of deformation (i.e. natural strain rate) to be able to predict the behaviour of these natural systems.

Examples of melt-bearing high-temperature experiments and of natural examples serve to indicate the occurrence and importance of mode 1 and mode 2 systems. Many deformation experiments with natural partially-molten rocks deformed by brittle processes like fracturing and cataclastic flow (e.g. van der Molen and Peterson, 1979, Dell'Angelo and Tullis, 1988) which is not treated in this study. However, the results of some experiments under ductile conditions appear to fit in well with our classification. For example, olivine-melt experiments by Hirth and Kohlstedt (1995a, b) and Mei et al. (2002) resulted in framework deformation processes (diffusion creep and dislocation creep respectively). One characteristic of these experiments is that the melt distribution after deformation was similar or only slightly different from the melt distribution in static experiments. This behaviour of homogeneous deformation and little melt redistribution indicates that  $\varphi_{\text{bulk}} < \varphi_{\text{GBS-L}}$ , so that the samples were deformed in the 1b or the 2c mode under the experimental conditions. However, Holtzmann et al. (2003a, b) presented olivine-melt and feldspar-melt deformation experiments that were performed with a torsion rig to a higher strain. Interestingly, deformation was heterogeneous in the feldspar system and also in the olivine system when oxides were added as a third phase. Shear bands developed during the deformation with an elevated melt-fraction, although the initial bulk melt-fraction was similar to the older experiments (ca. 2-6 wt. %). Holtzman et al.

(2003a) have related the spacing of the shear zones to the compaction length of the systems, however, they did not specify the deformation mechanism(s) in the shear zones. Tiling up of feldspar crystals in a small feldspar-melt shear zone (Fig. 3 of Holtzman et al. 2003a) and a similar or weaker CPO in a small olivine-melt shear zone compared to the surrounding less deformed matrix (Holtzman et al. 2003b) indicate that at least some of the strain in the shear zones has been accommodated by grain boundary sliding. This could, therefore, be an example for mode 2b deformation: Since ( $\phi_{\text{GBS-L}} < \phi_{\text{bulk}} < \phi_{\text{GSP}}$ ), GBS shear zones developed with a raised melt fraction and the matrix compacted by framework deformation. A similar switch in deformation behaviour between matrix and melt filled shear bands has also been reported by Rosenberg and Handy (2000) for analogue experiments (norcamphor-benzamide) during simple shearing. If norcamphor-benzamide melt behaves comparably to norcamphor-ethanol liquid, the reported melt fraction of 10-15% in the matrix (Rosenberg and Handy 2000) was already sufficient to overstep  $\phi_{\text{GBS-L}}$  and cause the reported shear zones with a further increased dynamic porosity that deformed mainly by GBS (Rosenberg and Handy, 2000, Rosenberg pers. comm. 2003). The fact that the comparable “high” liquid fraction of 10-15 vol. % did not induce granular flow by overstepping  $\phi_{\text{GSP}}$  (mode 1a or 2a behaviour) can possibly be explained by an uneven distribution of liquid at the beginning of deformation. For example, much melt was initially situated between the glass slides and the sample, which was due to melting of the sample after shearing had already started. Another possible example for the switch to mode 2b behaviour is the frequent observation of small melt-filled shear zones or shear bands in nature (e.g. Brown, 1994, Brown and Rushmer, 1997, Brown and Solar, 1998). Brown and Rushmer (1997) proposed melt induced local fracturing and cataclastic flow to explain the increased porosity. Alternatively, when the system had a bulk melt fraction above  $\phi_{\text{GBS-L}}$  and below  $\phi_{\text{GSP}}$  (2b mode) small initial melt fraction fluctuations would naturally cause the small shear zones without necessitating intracrystalline fracturing. The shear zones deform by localized grain boundary sliding which in turn creates new dynamic porosity and draws melt in from the matrix up to  $\phi_{\text{kz}} \approx \phi_{\text{GSP}}$  (notice that  $\phi_{\text{GSP}}$  in 3-D systems is expected to be higher than in our 2-D experiments). Another possible example for mode 2b deformation was presented by Sawyer (2001). His Fig. 2 (Sawyer, 2001, p. 294) traces melt pseudomorphs that were drawn from a thin Section of a molten metapelite. It shows an elongated region of connected melt pseudomorphs with an elevated melt-fraction of ca. 25 vol. % (region III in his Fig. 2) with two adjacent regions (I-II) with a lower melt-fraction that appears to be unconnected in the 2-D Section. The bulk melt-fraction of the whole Section shown is 12.5 vol.% (analysed with NIH image from Fig. 2 of Sawyer (2001)), which is probably below  $\phi_{\text{GSP}}$  in 3-D (Note, that although this is also an area measurement from a Section, the results represent true volume percentages, a method used e.g. in point

counting). This could possibly indicate that  $\square_{\text{GBS-L}}$  is between 12.5 vol.% and 6.4 vol.% (lower bracket is the melt-fraction of region I, Sawyer, 2001) in these naturally molten metapelites. These examples illustrate that switches between mode 2b and mode 2c/1b behaviour do occur in nature and experiments even at comparably low melt fractions below 10 vol. %, which occurs frequently in naturally molten rocks such as migmatites. The rheology of mode 2b systems (localized GBS deformation) cannot be simply approximated by measuring and extrapolating flow laws that were measured during framework deformation in 1b or 2c mode (framework deformation), even if the bulk melt fraction is similar. This is because the deformation mechanism is different (GBS versus dislocation or diffusion creep) and the local melt fraction in the deforming area is different (local shear zones with  $\square_{\text{local}} \approx \square_{\text{GSP}} > \square_{\text{bulk}}$  versus non-localized deformation with  $\square_{\text{local}} \approx \square_{\text{bulk}}$ ). Since the microstructural behaviour and the melt distribution at the grain-scale is strongly depending on such switches, further work is needed to constrain the mode of deformation of partially-molten, but maybe also fluid- or hydrocarbon-bearing bearing rocks at the temperature and strain rates of interest.

## 6.5 Conclusions

Experiments performed with the liquid-bearing norcamphor-ethanol system and the partially molten  $\text{KNO}_3 - \text{LiNO}_3$  system give information on a range of deformation mechanisms that potentially act in partially molten and fluid-bearing rocks from high to very low liquid fractions. The deformation behaviour of the analogue systems is characterized by three different deformation regimes (quoted liquid fractions are for 2-dimensional experiments, and are higher for 3-dimensional systems):

### *I. "High" liquid fraction $\geq 8-10$ vol. %: Compaction and granular flow*

At liquid fraction  $>10\%$  deformation is dominated by compaction. Strain is accommodated by grain rearrangement, GBS, and, at sufficiently low strain rate, by the disappearance of small grains due to grain coarsening, whose space is taken up by larger grains. At a liquid fraction between 8-10 vol. % ( $\square_{\text{GSP}}$ ) deformation of the norcamphor-ethanol and the  $\text{KNO}_3 - \text{LiNO}_3$  experiments is by distributed granular flow. In the norcamphor-ethanol experiments, liquid segregation is least efficient just at liquid fractions just above  $\square_{\text{GSP}}$ . In the  $\text{KNO}_3 - \text{LiNO}_3$  experiments, liquid segregation is even reversed by drawing in melt to enable GBS.

### *II. "Moderate" liquid fraction: Localized grain boundary sliding*

Below 8-10 vol.% ( $\square_{\text{GSP}}$ ) the "low" strain rate norcamphor-ethanol experiments and the nitrate experiments often exhibit conjugate shear zones that deform by GBS. The areas in between

form grain clusters that compact slightly and thereby loose liquid to the shear zones ( $\phi_{\text{local}} < \phi_{\text{bulk}}$ ), while the liquid fraction in the shear zones increases ( $\phi_{\text{local}} \approx \phi_{\text{GSP}} > \phi_{\text{bulk}}$ ). The degree of localization increases with a decreasing liquid fraction. The “high” strain rate norcamphor experiments do not exhibit this deformation stage but progress directly from regime I to III.

*III. “Low” liquid fraction: framework deformation by dislocation creep:*

The grains of the solid–liquid systems form a stress-supporting framework that deforms internally by a mechanism of framework deformation such as dynamic recrystallization accommodated dislocation creep (norcamphor–ethanol experiments). The grains recrystallize by very mobile grain boundaries that sweep highly strained areas of other crystals. Rotational recrystallization takes place with initial undulose extinction that concentrates into sub-grain boundaries, and finally the formation of new grains. These structures are similar to high-temperature deformation regime 3 in Hirth and Tullis (1992) and GBM regime of Stipp et al. (2002). The nitrate system exhibits anomalous grain growth.

In our experiments GBS deformation is not accommodated by diffusion creep as generally assumed (e.g. Paterson 2001), but is accommodated by an increased dynamic porosity through the influx of liquid. This requires that the liquid fraction locally exceeds a threshold, that depends on the grain shape (grain shape percentage,  $\phi_{\text{GSP}}$ ). If  $\phi_{\text{bulk}} \geq \phi_{\text{GSP}}$  all systems deform by granular flow and thereby completely loose cohesion. Since  $\phi_{\text{GSP}}$  is a geometric threshold, it can be expected to be similar in all solid-liquid systems with approximately equant crystals (8-10 vol. % in “two-dimensional” experiments). The transition between regimes II and III is called the grain boundary sliding–grain boundary locking threshold ( $\phi_{\text{GBS-L}}$ ). In contrast to  $\phi_{\text{GSP}}$ ,  $\phi_{\text{GBS-L}}$  varies depending on several parameters such as strain rate, strength of the grains, and the strength of welded grain boundaries. In our experiments  $\phi_{\text{GBS-L}}$  varied between ca. 8 vol.% (high strain rate norcamphor-ethanol experiment) and ca. 1% ( $\text{KNO}_3 - \text{LiNO}_3$  experiments). The interplay between the relative magnitude of  $\phi_{\text{GSP}}$  and  $\phi_{\text{GBS-L}}$  of a given system can possibly help to explain the regular occurrence of small melt-enriched shear zones or shear bands in nature and experiments.

## **7. The grain-scale behaviour of liquid in crystalline aggregates: A summary and outlook**

The previous Chapters have shown that the distribution and behaviour of liquid in artificial or natural polycrystalline aggregates (rocks) depends on many different parameters. The first and most important distinction to be made, before a more detailed understanding of the forces governing the liquid distribution is possible, concerns the size of the liquid batches investigated: liquid that is distributed as small droplets in grain interstices or that forms a tight grain-edge network with a size or tube diameter in the sub-micron to millimetre range behaves very differently from large-scale melt batches such as dykes, self-propagating lenses (hydrofractures), or plutons of metre to kilometre scale (see Section 1.4). Since this study is concerned with liquid distribution at the grain-scale, the main emphasis is laid on the most important small-scale effects, i.e. surface energy (Bulau et al., 1979) and of non-hydrostatic stress or strain (e.g. Daines and Kohlstedt, 1997, Holtzmann et al, 2003a, b). The central concept, which is generally applied to small-scale systems, is the wetting angle that is an expression of the ratio between the solid-solid and solid-liquid surface energy in the system of interest (see Section 2.1). The equilibrium wetting angle theory (Bulau et al., 1979, von Bargen and Waff, 1986) derives the hypothetical “equilibrium” liquid distribution by only considering the liquid fraction and the equilibrium requirements of a constant wetting angle and of a constant boundary curvature between liquid and crystals (see Section 2.3.2.). Because rock-forming minerals do not fulfil the requirement of an isotropic surface energy, several theoretical and experimental studies tried to incorporate the effect of a crystal lattice anisotropy on the wetting angle and predict the melt distribution and permeability for such systems (Faul, 1997, Laporte and Provost, 2000, Zhu and Hirth 2003). However, despite the complexities of these approaches, they still follow the original idea of Bulau (1979) of a perfect thermodynamic equilibrium liquid distribution in a polycrystalline system. However, in Section 2.4 and Chapter 4 and 5 it was shown, that a polycrystalline system can never be in a true thermodynamic equilibrium, because the same driving force that acts towards an even distribution of a wetting liquid, also results in continuous surface energy driven recrystallisation. In Chapter 6 the behaviour of solid-liquid systems during deformation was investigated. It is clear from the analogue experiments of Chapter 6 that stress and deformation can have a strong effect on the liquid distribution, e.g. by segregation of liquid from areas that deform by framework deformation, or by drawing liquid into areas that deform by grain boundary sliding. It can therefore be concluded from Chapter 4 to 6, that the liquid distribution at the grain-scale is continuously affected by a range of additional mechanisms, such as surface energy, strain, or chemical disequilibrium that to some degree

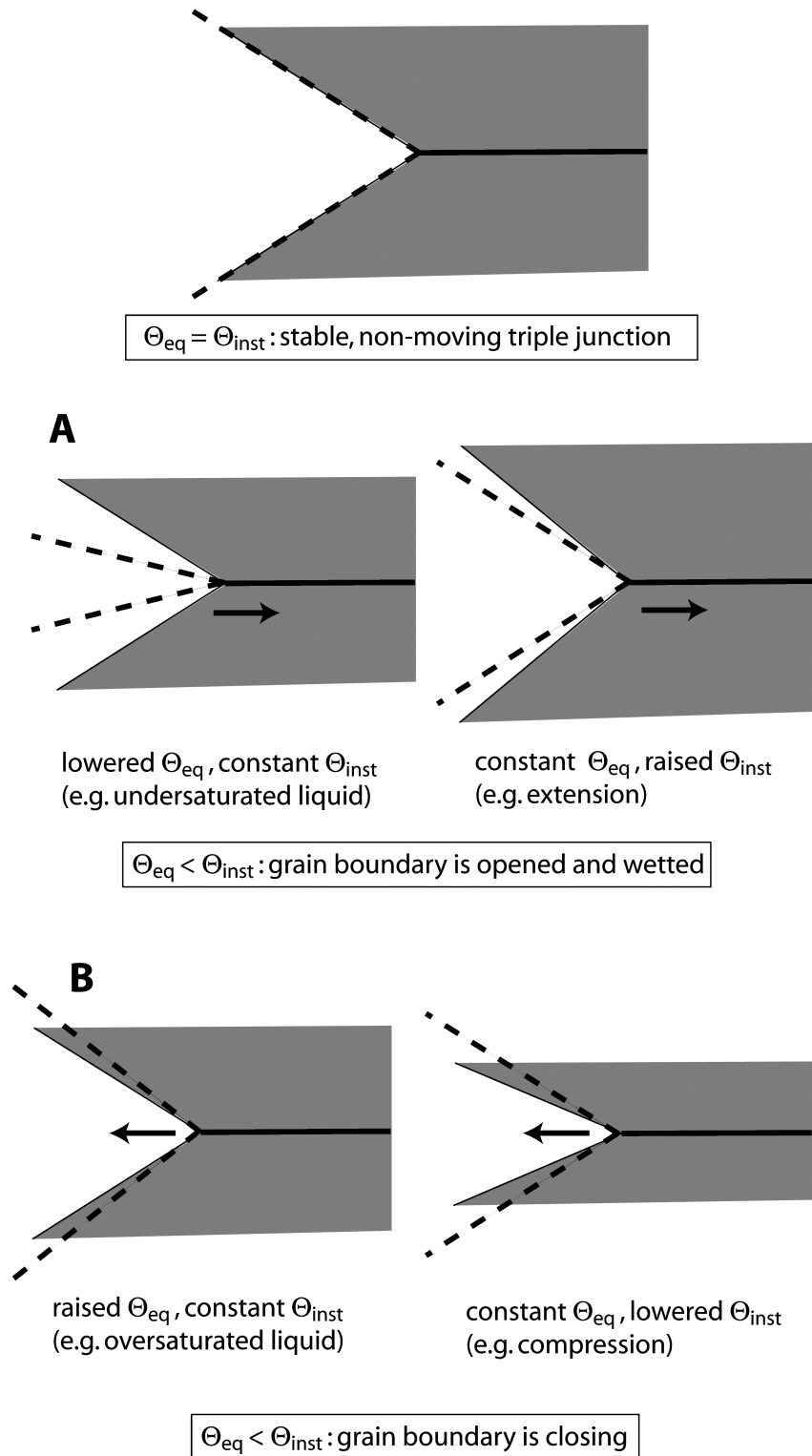


**Fig. 7.1.** The effect of altered wetting angles on a s-s-l triple junction. If the equilibrium angle and the instantaneous angle are equal, the triple junction is in equilibrium and does not move with respect to the grains. **A.** A lowered equilibrium or a raised instantaneous wetting angle lead to opening of the grain boundary. **B.** A raised equilibrium or a lowered instantaneous wetting angle lead to closing of the grain boundary.

modify the ideal equilibrium distribution (cf. Bulau et al., 1979). The next Sections aim to provide an outline and a summary of these modifying mechanisms and their effect on the

liquid distribution. The interpretations presented here are mainly based on the concept of altered dynamic wetting angles that was introduced in Chapter 5. In this study, the investigations were restricted to the case of “ideal” crystals that have no surface energy anisotropy. With the analogue system norcamphor plus ethanol liquid, an almost isotropic system has been found for *in-situ* investigations of the static and dynamic liquid distribution. Although rock-forming minerals usually have a significant crystal lattice anisotropy, the results derived from these simplifications may provide a basis for a more general theory on the liquid distribution at the grain-scale.

## 7.1 Response of a liquid to a change of the dynamic or the equilibrium wetting angle

In principle, most deviations from an equilibrium liquid distribution at the grain-scale (excluding brittle processes) can be explained by a readjustment of the liquid phase to either altered *dynamic* wetting angles (henceforth called the instantaneous wetting angle ( $\theta_{inst}$ ) to include the case of  $\theta_{inst} = \theta_{eq}$ ) or to a changed *equilibrium* wetting angle (see Chapter 5). Before moving to the mechanisms that may alter the dynamic or equilibrium angle, we have to consider the different responses of a liquid to a change of either.

Consider a starting configuration with an immobile triple junction, which forms an equilibrium wetting angle between two grains and a liquid (Fig. 7.1). If the *equilibrium* angle is **lowered** by some process (leaving the instantaneous angle unchanged), the triple junction adjusts by opening of the grain boundary until the new equilibrium angle is reached, or, if the new equilibrium angle is  $0^\circ$ , until the grains are separated by the liquid (Fig. 7.1a). If, on the other hand, the *instantaneous* angle is increased by some process (Fig. 7.1a), the triple junction is moving in the same direction, i.e. the grain boundary area shrinks, until the equilibrium angle is regained or the grains are separated. Thus, a lowered  $\theta_{eq}$  and a raised  $\theta_{inst}$  have a similar effect on the liquid distribution. This follows from the fact that in both cases the equilibrium angle is lower than the instantaneous angle. If on the other hand the equilibrium angle is higher than the instantaneous angle, the grain boundary area increases (Fig. 7.1b). Based on this idea, the liquid behaviour at a triple junction can be summarized with two general rules:

1. If  $\theta_{inst} = \theta_{eq}$ , the triple junction is immobile and in equilibrium, if  $\theta_{inst} \neq \theta_{eq}$ , the triple junction is mobile
2. If  $\theta_{inst} > \theta_{eq}$ , the adjacent grain boundary area decreases and the grains are wetted, if  $\theta_{inst} < \theta_{eq}$ , the grain boundary area increases.

These two rules have already been suggested and are further explained in Chapter 5. The consideration above shows, that they remain valid even if the equilibrium angle is altered. They can therefore be generally applied for all cases of wetting angle change.

### 7.1.1. *Equilibrium liquid distribution*

From the two rules above we have another way of looking at the perfect equilibrium liquid distribution of von Bagen and Waff (1986) (see Chapter 2). The equilibrium distribution is reached in an isotropic system, when  $\theta_{inst} = \theta_{eq}$  and a constant  $k_{mean}$  is true for the whole system at any time. As was shown in Chapter 2.4, this cannot be the case in a polycrystalline system with a non-uniform grain-size, with the exception of a 2-dimensional perfect hexagonal grid.

## 7.2 Driving forces for the change of $\theta_{inst}$ or $\theta_{eq}$

Four general driving mechanisms can be distinguished that potentially influence the liquid distribution by altering the instantaneous and/or the equilibrium wetting angle:

1. Surface energy driven liquid-assisted recrystallization. Recrystallization constantly moves the liquid-filled triple junctions and changes the *instantaneous* wetting angle.
2. Liquid over- or underpressure: In equilibrium, the pressure difference between liquid and solid is determined by the curvature of solid-liquid boundaries (equation (2.21) and Section 2.2). If the pressure difference is changed by external processes, the wetting angle and the curvature of the system is expected to be temporarily altered. It is not clear, yet, whether this changes only the instantaneous angle or also the equilibrium angle.
3. Chemical disequilibrium between the liquid and the matrix, i.e. the liquid is either under- or oversaturated with components of the solid matrix. Chemical disequilibrium changes the *equilibrium* wetting angle.
4. Non-hydrostatic stress and/or strain (dynamic wetting). Grain boundary sliding changes the *instantaneous* wetting angle. It is not clear, yet, what happens in detail during framework deformation.

Fig. 7.2 is a sketch that summarizes some of the complex interactions between the wetting angles and the different internal and external forces. In the following Sections, a short overview of the four mechanisms and the consequence for liquid distribution is presented.

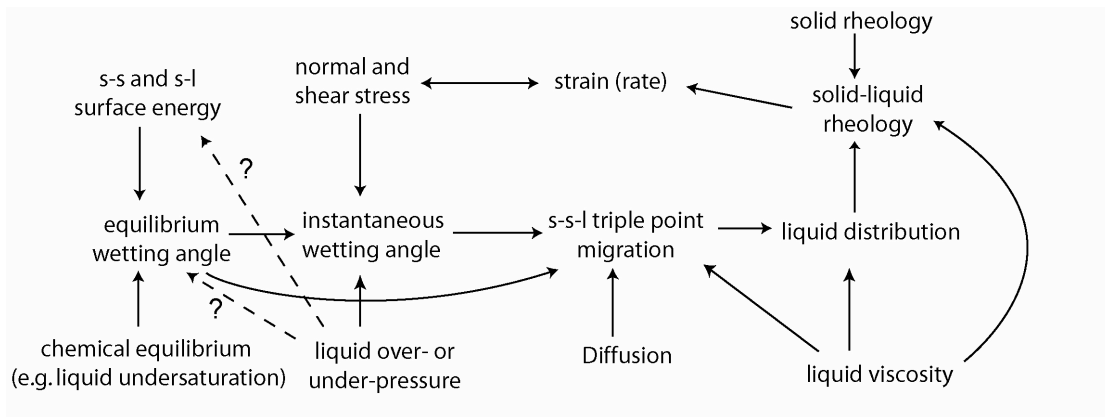


**Fig. 7.2.** Schematic representation of the most important mechanisms that determine the liquid distribution in a solid-liquid system at the grain-scale.

However, this is only a first approach based on simplified assumptions and further theoretical, experimental, and numerical work is necessary to constrain the hypotheses that are presented below.

### 7.3 Surface energy driven static recrystallization

This subject was treated in detail in Chapter 4 and 5. In summary, the continuous increase in mean grain-size causes movement of the melt-filled triple junctions, which constantly modifies the instantaneous wetting angles while leaving the equilibrium angle unchanged. The dissolution of small grains leads to the formation of disequilibrium features, such as fully wetted grain boundaries, large liquid pools, distorted triple junctions, and trapped liquid lenses.

### 7.4 Gravity and liquid overpressure

Waff (1980) considered the influence of gravity on the three-dimensional liquid distribution. He argued that in a stationary, interconnected column of liquid with  $\theta_{eq} < 60^\circ$ , the  $\Delta P$  between the liquid and the solid in textural equilibrium given by equation (2.21) of Section 2.2 can only be maintained at its base, because of the density contrast between solid and liquid. The actual pressure difference at height  $h$  above the base is according to Waff (1980)

$$\Delta P = 2\Delta\rho gh\gamma_{sl}k_{mean} \tag{7.1}$$

where  $\Delta\rho$  is the density difference between liquid and matrix,  $g$  the gravitational acceleration,  $\gamma_{sl}$  the solid-liquid interfacial energy, and  $k_{mean}$  the mean curvature, (7.1) is

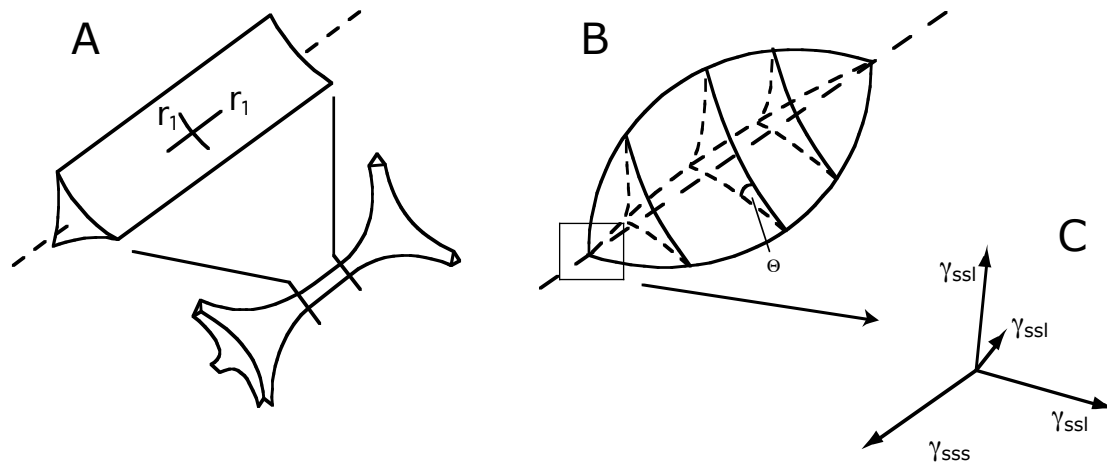


**Fig. 7.3.** **A.** Representation of a liquid tube between three adjacent grains for a liquid with a wetting angle  $<60^\circ$ . At a low liquid fraction the principle curvature parallel to the tube approaches zero. **B.** The effect of a liquid overpressure on the liquid geometry according to Waff (1980). If the equilibrium conditions are applied and the wetting angle is to remain constant, the curvature parallel to the tube has to become positive. This destroys the liquid network and reduces the permeability. **C.** Vector balance at the tip of the altered grain tubes. The tips are only stable if  $\sigma_{ss}$  is greater than  $3\sigma_{sl}$ . See text for discussion. A-B redrawn after Obata and Takazawa (2004).

simply derived by combining equation (2.21) (Section 2.2) with the equation for pressure as a function of depth at constant density ( $P = \rho gh$ ). The argument of Waff (1980) can be summarized as follows. In equilibrium the initial under-pressure of the liquid at the base of the molten zone rises to zero and even to positive values within the first few metres above the base according to (7.1) (Fig. 7.4). In order to stay in textural equilibrium, the mean curvature of the solid-liquid interfaces has to adjust to this pressure change from an initial negative curvature to a positive curvature (see Section 2.2 for discussion of the relation between pressure and curvature). If the wetting angle is to remain constant e.g. in the three-grain tubes, the principle axis of curvature that lies parallel to the tube direction (Fig. 7.3) has to change from nearly zero ( $r = \infty$ ) to positive values (a positive decreasing  $r$ ), because the principle axis of curvature perpendicular to the tube cannot change without changing the wetting angle. This would lead to a pinch-off of the tubes, which results in breakdown of the liquid network and a permeability reduction to zero (Fig. 7.3b). This model has been used by Obata and Takazawa (2004) to explain the compositional layering of the Horoman peridotite of Japan. If these considerations are valid, they would have a profound influence on all models for melt migration by porous flow e.g. by linear Darcyan flow (e.g. McKenzie, 1984) or by episodic melt transport by porosity waves (e.g. Rabinowicz et al., 2001), because they would strongly reduce the effective permeability over long distances (Waff, 1980, Obata and Takazawa, 2004). However, this model has not been verified by any experimental evidence, yet, and more importantly, it also contains several inconsistencies. Firstly, for the derivation of equation (7.1), the model assumes a static, interconnected column of melt which is

nevertheless assumed to be in textural equilibrium so that the rule of constant wetting angle and constant mean curvature is fulfilled. However, these two requirements of a perfect thermodynamic equilibrium and no melt migration along the hydraulic head exclude each other. Before the liquid can migrate upwards, thermodynamic equilibrium is not established in the system, and no simple equilibrium assumptions may be used for predicting the liquid geometry. However, as soon as the melt is allowed to migrate upwards along the hydraulic head, the liquid pressure gradient adjusts to the solid pressure gradient (Fig. 7.4b), and the equilibrium  $\Delta P$  for textural equilibrium can be regained. As long as a steady state, non-episodic flux of liquid migration along the hydraulic head is possible, the “equilibrium” liquid network geometry as suggested by von Bargen and Waff (1986) is possible (modified by the effect of grain growth as described above). Secondly, even if the liquid is overpressured with respect to the matrix (e.g. because of episodic liquid transport) the cigar shaped liquid distribution suggested by Waff (1980) can be shown to be unstable with a similar vector tension analysis that was used to derive the equation for the equilibrium-wetting angle in Section 2.1 (Fig. 2.2). For this, a “line-junction” energy is attributed to the solid-solid-solid and the solid-solid-liquid triple line junctions ( $\Gamma_{ss}$  and  $\Gamma_{sl}$  respectively), similar to the definition of the solid-solid and solid-liquid surface energy ( $\sigma_s$  and  $\sigma_l$ ).  $\Gamma_{ss}$  and  $\Gamma_{sl}$  is the excess energy per unit length [J/m] of solid-solid-solid and solid-solid-liquid line interSection. Similarly to the definition of surface tension in Chapter 2, this can be viewed as a line tensional force [N]. Considering the line tensions, it is now possible to balance the four line tensions at a solid-solid-solid-liquid quadruple junction, similarly to the vector diagram which was drawn at a triple junction to derive the wetting angle (compare Fig. 7.3c with Fig. 2.2). For this junction to be stable, the tension vector of the s-s-s junction has to be equal to or greater than the sum of the three s-s-l vector tensions combined (Fig. 7.3c):

$$\Gamma_{ss} \geq \Gamma_{sl} + \Gamma_{sl} + \Gamma_{sl} \quad (7.2).$$

However, this is only the case for a wetting angle  $\theta_{eq} \geq 60^\circ$ , and if the wetting angle is lower, the three-grain tubes are occupied by liquid. Since Waff (1980) assumes the wetting angle to be constant, the surface energies and the line energies have to be constant, too, because the wetting angle is derived from the surface energies, no matter whether  $\Delta P$  is positive or negative. The resulting non-zero vectorial forces would open the cigar shaped three-grain junction in the same way as described for the raised dynamic wetting angles in Chapter 5. Thirdly, it was shown in Chapter 5 that the wetting angle itself is the result of a force balance that can be raised or lowered dynamically by many processes such as recrystallization. It is therefore flawed to treat the wetting angle as a constant. This can be understood by

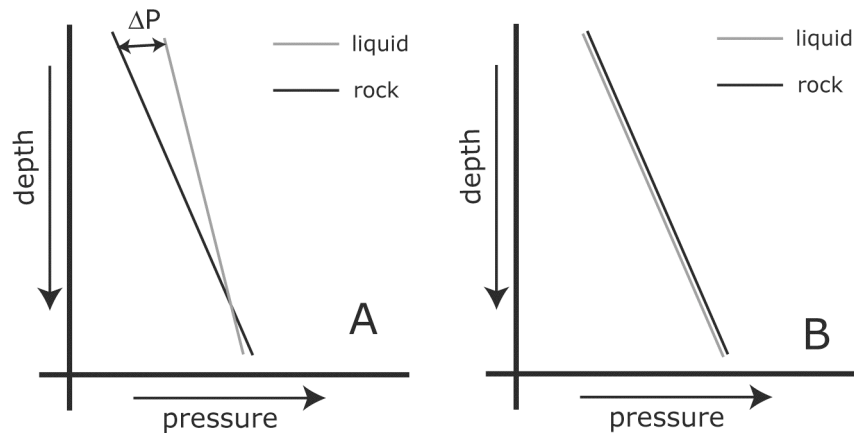


**Fig. 7.4.** Schematic representation of the pressure versus depth profile of a rock column that contains a connected liquid phase. **A.** If the liquid is not moving, the density differences between the rock and the connected liquid network causes an increasing liquid overpressure that depends on the height above the base. **B.** If the liquid is allowed to migrate upwards along the hydraulic head, the liquid pressure gradient adjusts to the lithostatic pressure in a steady state, and the solid-liquid pressure difference can be determined by the liquid geometry.

considering the shape of the four-grain pools. Here, the mean curvature would also have to adjust to the liquid overpressure as in the grain-tubes, however, any change of one of the principle radii would automatically produce a raised wetting angle. It is still unclear whether the equilibrium or only the instantaneous wetting angle is changed by liquid pressure differences. The detailed effect of fluid pressure changes on the wetting angle, the distribution of liquid, and the evolution of permeability in a liquid-bearing aggregate will be treated in a separate publication (Bons et al., in prep.).

## 7.5 Chemical disequilibrium between the liquid and the grains

The constant wetting angle concept only applies for chemical equilibrium conditions. During a chemical reaction, a change of surface free energy equal to the free energy change per unit area of the reaction occurs at the interfaces, so that the wetting angle is changed (Aksay et al., 1974). A simple example is the influx of a under- or oversaturated liquid in a crystalline system. Fig. 7.5 shows a norcamphor aggregate that is in contact with undersaturated ethanol liquid. Contrary to the effect of saturated liquid that only spreads through the triple junctions of the norcamphor with a wetting angle of ca.  $25^\circ$  (see Chapter 5), the under-saturated liquid completely surrounds the norcamphor grains, so that an effective wetting angle of  $0^\circ$  is indicated. The process starts with the formation of liquid filled triple junctions (Fig. 7.5 a) from which the liquid quickly spreads into the grain boundaries (Fig. 7.5 b-d). Notice the liquid lens in b (arrow) that grows until the boundary is fully wetted. The two sides of the lens form a dynamic wetting angle that is larger than the “equilibrium“ angle (which is  $0^\circ$ ,  $\theta_{inst} >$

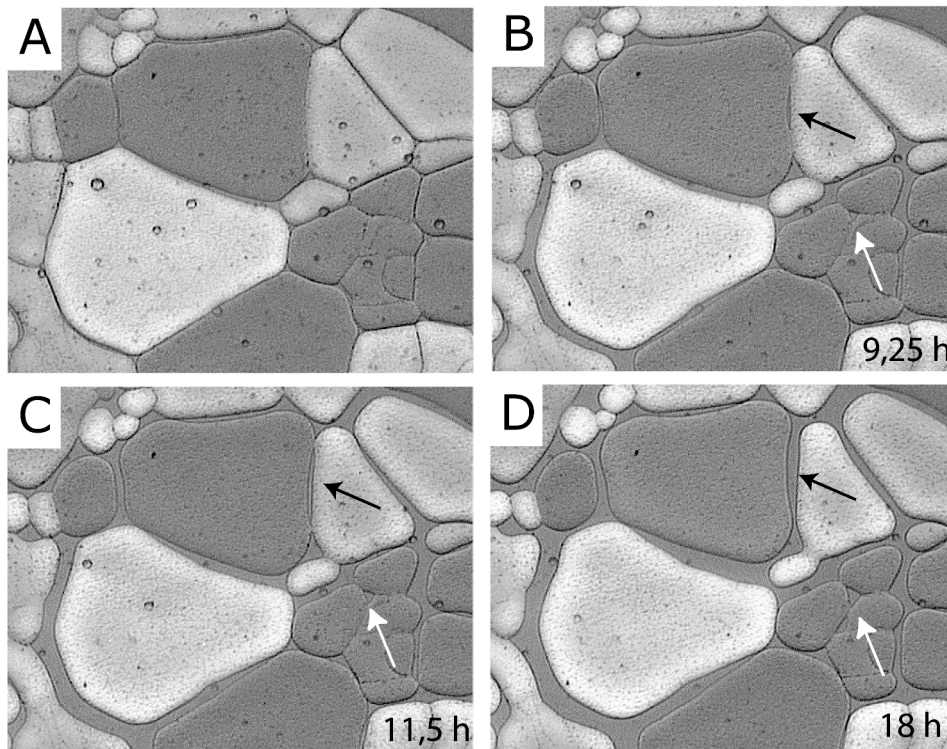


**Fig. 7.5.** Influx of under-saturated ethanol in an initially dry norcamphor aggregate. In the beginning the liquid is mainly situated in the triple junctions, from there the liquid spreads along all grain boundaries. Black arrow marks an opening liquid lens. White arrow marks opening triple junctions at subgrain-boundaries. Here, the instantaneous wetting angle is around  $60^\circ$ , however, since the equilibrium angle of subgrain-boundaries is  $>90^\circ$ , the opening requirement ( $\theta_{eq} < \theta_{inst}$ ) is fulfilled and the triple junctions grow. See also movie 2.19 on the enclosed DVD.

$\theta_{eq}$ ), the grain-boundary is therefore opened according to figure 7.1. For a saturated liquid the lens would close since the dynamic wetting angle would be lower than the equilibrium angle ( $\theta_{inst} > \theta_{eq}$ ) even if the instantaneous angle might be the same. A contrary effect is expected from an oversaturated liquid, which raises the equilibrium wetting angle.

## 7.6 Deformation

Chapter 6 dealt with deforming solid-liquid systems, but the main subject of that Chapter was the influence of the liquid on the deformation of polycrystalline systems. In this Section, the influence of stress and strain and the different deformation regimes on the liquid distribution will be considered. Because the behaviour of liquid during deformation is a very complex issue that is only partially understood yet, only some lines of thought are presented here, which mainly follow from the results of Chapter 4 to 6, especially using the concept of the instantaneous and the equilibrium wetting angle. Based on the total strain and the strain rate for the distribution of liquid, three cases of systems experiencing non-hydrostatic stress can

be distinguished:

1. Systems exposed to non-hydrostatic stress with only limited finite strain (e.g. high-temperature experiments)
2. Systems exposed to a very low differential stress deforming with a low strain rate compared to the rate of recrystallization and “textural readjustment”
3. Systems deforming with a higher steady state strain rate:
  - A high liquid fraction: granular flow
  - B moderate liquid fraction: localized GBS (above  $\square_{\text{GBS-L}}$ )
  - C low liquid fraction: framework deformation (below  $\square_{\text{GBS-L}}$ )

### 7.6.1 *Non-hydrostatic stress with limited finite strain*

Consider the case of a partially-molten system that experiences non-hydrostatic stress, but that has accumulated little strain, yet. Typical examples are high-temperature experiments that are rarely deformed to strains exceeding 0.3 and often remain below 5% finite strain (e.g. Kohlstedt 2004), with the exception of torsion experiments (e.g. Holtzman 2003a). Although this special case is probably not very important for nature, it is important to understand high-temperature experiments, and also allows to study the effect of stress on the distribution of liquid without having to consider the complicated geometrical changes during steady state deformation. In Section 5.4.1 the effect of mechanical stress on the wetting angle was already considered. A grain boundary is expected to develop raised dynamic wetting angles if it is oriented parallel to  $\square_1$ , and lowered dynamic wetting angles if it is oriented perpendicular to  $\square_1$  (Fig. 5.17, Section 5.4.1). Notice that the equilibrium angle remains unchanged in this case. The instantaneous angle is therefore higher than the equilibrium angle and lower than the equilibrium angle, respectively. The result of the altered dynamic angles are wetted grain boundaries that are approximately parallel to  $\square_1$  and dry grain boundaries perpendicular to  $\square_1$  as reported e.g. by Gleason et al. (1999) for a sample of quartz-feldspar-melt deformed to a strain of 0.26 and by Daines and Kohlstedt (1997) for olivine plus mafic melt. Note, that the wetted grain boundaries are probably **not** the result of a locally lowered equilibrium wetting angle as was suggested by Daines and Kohlstedt (1997).

### 7.6.2 *Low Non-hydrostatic stress and a low strain rate*

One important and unresolved question concerns the transition from an “equilibrium” solid-liquid system in which the liquid distribution is mainly determined by the wetting angle (and the recrystallisation rate), and a dynamic system where the liquid distribution is determined by differential stress and/or strain. In the mantle the strain rates were suggested to be

sufficiently slow that the liquid distribution can be treated to be static (McKenzie, 1984, Kohlstedt, 1992). However, this general assumption has not been quantified, yet. What exactly, is the differential stress or the strain rate, at which the liquid distribution can still be considered as static? It follows from Chapter 5 and Section 7.1, that the instantaneous and the equilibrium wetting angles simply have to be sufficiently close together for this assumption to be valid. With “sufficiently close” is meant, that the slight but *oriented* liquid redistribution due to the differential stress (see Section 7.6.1 above) cannot be statistically distinguished from the *randomly* oriented liquid modifications produced by the surface energy driven grain growth (Chapter 5 and Section 7.3). To quantify this effect, the connection between the stress tensor and the mechanical stress at the triple junctions has to be known as a function of the orientation, as well as the absolute s-s surface tension of the system of interest. This would have to be measured *in-situ* with experiments. When these parameters are known, the critical strain rate of transition could be calculated.

### 7.6.3 *Systems deforming with a higher strain rate*

In Chapter 6 three generally possible modes of solid-liquid deformation were introduced: granular flow, localized grain boundary sliding, and framework deformation. All three were shown to have a strong influence on the liquid distribution in the particular system. Only the liquid response to the two end-member cases of granular flow and dislocation creep is considered here, since the transitional localized grain boundary sliding stage is a combination of both mechanisms.

#### 7.6.3.1 *Liquid behaviour during granular flow and grain boundary sliding*

During granular flow or grain boundary sliding, the individual grains of an aggregate slide past each other. For the grains to be able to move independently, the initially dry grain boundaries have to be broken as described in Chapter 6, which leads to a thin layer of liquid that separates the grains. To investigate this process in more detail, the behaviour of air bubbles during deformation can be considered. Air has a very high wetting angle in contact with the norcamphor grains, and therefore forms round air bubbles within the aggregate, a behaviour which is predicted for high wetting angles close to  $180^\circ$  (see Chapter 2). However, when the aggregate deforms by grain boundary sliding, the distribution and “wetting” behaviour of air changes dramatically (Fig. 7.6). The air bubbles collapse, and the air spreads between the sliding grains. Once the deformation stops, the air slowly reassumes the original round shape. This spreading between the grains is a semi-brittle process, the air of the collapsing bubble seems to have a slight overpressure, that breaks the grain boundaries. According to the classification of Fig. 7.1, the mechanical stress at the boundaries or possibly

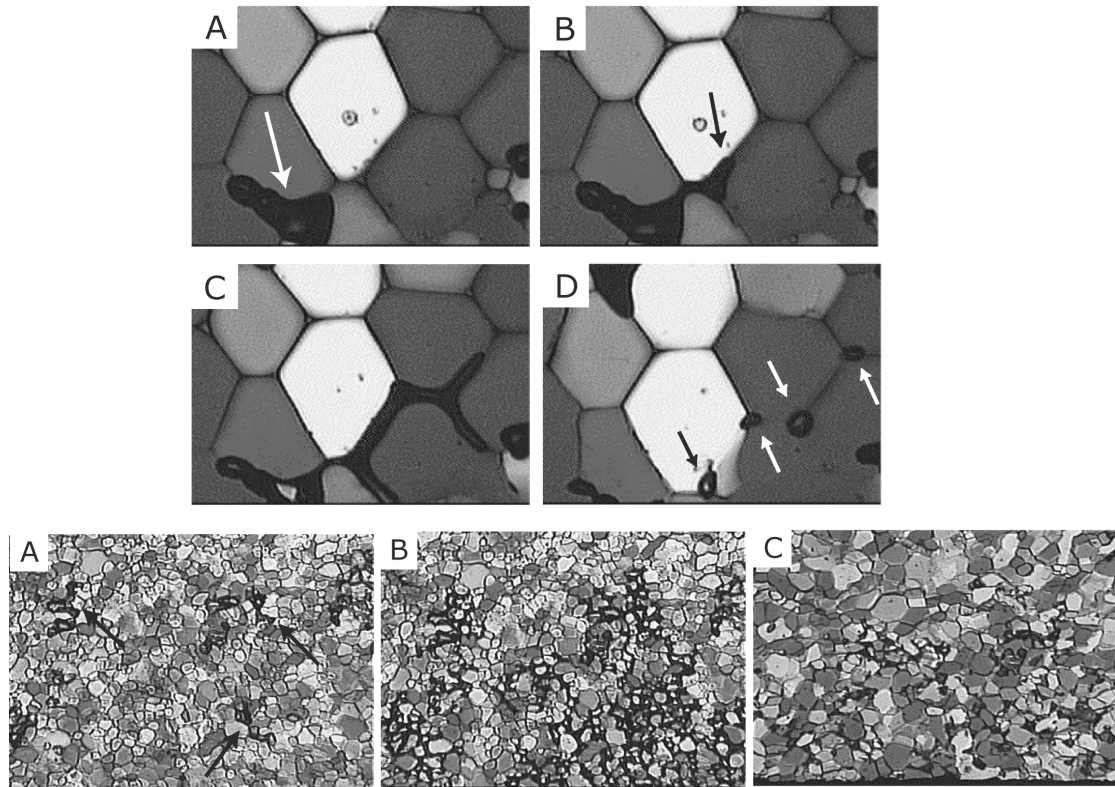


**Fig. 7.6.** The behaviour of air bubbles in a deforming aggregate. **Top:** In a norcamphor-ethanol experiment. During grain boundary sliding the bubbles collapse and spread through the aggregate. Once grain boundary migration recrystallization starts, the network is destroyed. See also movie 2.33-1-4 on the enclosed DVD. **Bottom:** Small air bubbles in a partially-molten  $\text{KNO}_3\text{-LiNO}_3$  aggregate spread along the grain boundaries and form a connected network during grain boundary sliding, that breaks down once a framework deformation process set in. See also movie 17-1 on the enclosed DVD. Note, that in both experiments very little strain is necessary to spread the air “liquid”.

the overpressure of the air “liquid” results in raised instantaneous wetting angles ( $\theta_{\text{inst}} > \theta_{\text{eq}}$ ), so that the grain boundaries are “wetted”. This leads to a quite remarkable possibility: solid-liquid systems with a high wetting angle, that are usually assumed to be immobile (Section 2.3.2) could temporarily form a three-dimensionally connected liquid network during GBS deformation and thereby become mobile. Important high-wetting angle systems are olivine + sulphide melt and eclogite plus certain metamorphic fluids, and the former system governs the early differentiation of the Earth (e.g. Laporte and Provost, 2000) and the latter system is important for the dehydration of the descending slab during subduction (Ono et al., 2002). However, the potential of GBS as a means for enhancing liquid migration has to be further investigated by experiments and numerical simulations to evaluate the occurrence and importance in nature.

### 7.6.3.2 *Liquid behaviour during framework deformation*

The behaviour of liquid during framework deformation is largely unclear. Urai (1983) reported a thin film of liquid between migrating grain boundaries in bishofite-water experiments during dislocation creep, which was, however, inferred indirectly. Tullis et al (1996) reported dynamic wetting in feldspar aggregates during deformation. However, it can be suspected from their images that the aggregate might have deformed (partly) by grain boundary sliding, which would explain the dynamic wetting mechanism (see Section above). Hirth and Kohlstedt (1995) and Gleason et al (1999) reported dry grain boundaries during framework deformation experiments. The wetting behaviour during dislocation creep in the norcamphor–ethanol experiments of this study is unclear, although in one experiment the well-wetting ethanol liquid actually behaved as if it was non-wetting during dislocation creep. However, this has not been verified with other experiments, yet. In experiments in which air served as an analogue for a non-wetting liquid phase, the temporary network, that formed during GBS deformation broke down once grain boundary migration recrystallization accommodated dislocation creep commenced in the aggregate (Fig. 7.6). These observations would rather suggest a dynamic “drying” than a dynamic wetting mechanism, however, these initial observations have to be verified by further experiments.

Although the issue of dynamic wetting is still largely unexplained (Daines, 1997), the distinction of instantaneous and equilibrium wetting angles (Fig. 7.1) possibly provides a new approach to further investigation in these issues. Especially dynamic wetting during framework deformation mechanisms, such as dislocation and diffusion creep, remains unexplained. However, it can be argued that, regardless of the deformation mechanism, the higher the non-hydrostatic stress is, the higher the potential influence of stress as opposed to the “equilibrium” influence of surface energy forces on the liquid distribution. From this viewpoint it can be expected that dynamic wetting is far more important in high strain-rate experiments than in the low strain-rate nature.



**Appendix A: Notation**

- $A_i$  area of phase  $i$ ,  $m^2$ .
- $a_i^k$  activity of component  $i$  due to curvature  $k$  (Chapter 2).
- $|A|$  mean grain area at time  $t$  (grain growth, Chapter 2),  $m^2$ .
- $|A|_0$  mean grain area in the beginning of an experiment (Chapter 2),  $m^2$ .
- $|d|$  mean grain diameter at time  $t$  (Ostwald ripening, Chapter 2),  $m$ .
- $|d|_0$  mean grain diameter in the beginning of an experiment (Chapter 2),  $m$ .
- $F$  Helmholtz free energy (Chapter 2),  $J$ .
- $F_{\perp}$  normalized perpendicular force on a triple junction.
- $F_{\parallel}$  normalized parallel force on a triple junction.
- $G$  Gibbs free energy (Chapter 2),  $J$ .
- $k$  permeability,  $m^2$ .
- $k_g$   $T$  and material dependent parameter for grain growth (Chapter 2).
- $k^s$  solid-liquid curvature:  $k^s = 1/r_{\text{grain}}$ ,  $m^{-1}$ .
- $k$  liquid pocket curvature:  $k = -k^s$ ,  $m^{-1}$ .
- $k_{\text{mean}}^s$  mean solid-liquid curvature in a 3-D system:  $k_{\text{mean}}^s = 0,5(1/r_1 + 1/r_2)$ ,  $m^{-1}$ .
- $k_{\text{mean}}$  mean curvature of a 3-D liquid pocket:  $k_{\text{mean}} = -k_{\text{mean}}^s$ ,  $m^{-1}$ .
- $n$  exponent of the Blake-Carman-Cozony equation.
- $n_i$  moles of component  $i$ .
- $P$  pressure,  $Pa$ .
- $T$  temperature,  $K$ .
- $v$  triple junction velocity,  $\mu m/h$ .
- $V$  volume,  $m^3$ .
- $w$  work,  $J$ .

- $\Gamma_S$  solid-solid surface tension vector, N/m.
- $\Gamma_{SL}$  solid-liquid surface tension vector, N/m.
- $\Gamma$  surface energy, surface tension (scalar), J/m<sup>2</sup>, N/m.
- $\Gamma_{SS}$  solid-solid surface energy, J/m<sup>2</sup>, N/m.
- $\Gamma_{SL}$  normalized solid-liquid surface energy.
- $\Gamma$  total surface energy of a system, J/m<sup>2</sup>.
- $\Gamma_{SL}$  total solid-liquid surface energy of a system, J/m<sup>2</sup>.
- $\theta$  general dihedral or wetting angle, degree.
- $\theta_{tr}$  true wetting angle measured perpendicular to a solid-solid-liquid line interface, degree.
- $\theta_{ap}$  apparent wetting angle measured at an unknown angle to a solid-solid-liquid line interface, can over- or underestimate  $\theta_{tr}$ , degree.
- $\theta_{eq}$  equilibrium true wetting angle (static), degree.
- $\theta_{dy}$  dynamic true wetting angle (moving), degree.
- $\theta_{inst}$  instantaneous true wetting angle (moving or static), degree.
- $\mu_i$  chemical potential of component i.
- $\rho$  density, kg/m<sup>3</sup>.
- $f$  liquid fraction.
- $f_{bulk}$  bulk liquid fraction.
- $f_{SZ}$  liquid fraction in a shear zone.
- $f_{local}$  local liquid fraction.
- $\theta_{GSP}$  grain shape percentage.
- $\theta_{GBS-L}$  grain boundary sliding – grain boundary locking threshold.

## Appendix B: Movie captions

The following list describes the movies from analogue experiments that were performed as part of my Ph.D. project. The movies are saved in Quicktime format and can be found on the enclosed DVD. Nearly all movies from successful experiments are enclosed, however, the important or interesting movies are marked by bold experimental numbers in the following list. Because nearly every movie displays some interesting or surprising behaviour, there is a lot more information contained in them than could be described in the text. Experiments were either performed statically to investigate the sample behaviour during static recrystallization, or deformation experiments were performed. The static experiments with the norcamphor-ethanol systems were performed at room temperature, which inhibited thermal gradients. The partially-molten nitrate experiments were heated, so that thermal gradients existed within the sample. The sometimes surprising effects of thermal gradients on a partially molten system can be observed in the nitrate movies. The deformation experiments were performed with three motors with different displacement and strain rates:

Motor **A**: Displacement rate 5,90 mm/h, strain rate  $3,28 \cdot 10^{-4} \text{ s}^{-1}$  for a sample width of 5 mm.

Motor **B**: Displacement rate 0,941 mm/h, strain rate  $5,23 \cdot 10^{-5} \text{ s}^{-1}$  for a sample width of 5 mm.

Motor **C**: Displacement rate  $4,06 \cdot 10^{-2} \text{ mm/h}$ , strain rate  $2,26 \cdot 10^{-6} \text{ s}^{-1}$  for a sample width of 5 mm.

The strain rate changes in a constant displacement experiment depending on the distance of the pistons. The strain rate was calculated for a typical sample width of 5 mm.

Much of the information about the experimental conditions is already contained in the movie titles. For example the title **31-3-C-10x-94h-192°** means: Experimental number (**31-3**), used motor (**C**), objective magnification (**10 times**), movie duration (**94 hours**), experimental temperature (**192°C**). All movie titles on the DVD are coded according to that scheme. If no A,B, or C is added, the experiment is static. All experiments with temperatures below 100°C are norcamphor experiments, all other experiments are partially-molten  $\text{KNO}_3\text{-LiNO}_3$  experiments. A question mark (?) indicates that this particular information in question was not properly recorded or lost, but could be reconstructed with some certainty. Please contact me, if you make interesting observations that escaped my attention or that can be interpreted differently and feel free to use these movies for teaching purposes.

### Static norcamphor– ethanol experiments

#### Overview movies

**2.04-10x**: duration 75 hours, width of view 2 mm,  $T = 26^\circ\text{C}$ .

Static liquid assisted recrystallisation, low liquid fraction. Interesting is the behaviour of the trapped air bubbles, that migrates episodic.

**2.05-5x:** duration 46 hours, width of view 4 mm, T = 27°C.

Static liquid assisted recrystallisation, low liquid fraction. Many disequilibrium features.

**2.05-3-10x:** duration 45 hours, width of view 2 mm, T = 25°C.

Static liquid assisted recrystallisation, low liquid fraction. Many disequilibrium features. Compare with Figs. 4.2, 5.4, and 6.2.

**2.06-1-10x:** duration 14 hours, width of view 2 mm, T = 25°C.

Static liquid assisted recrystallisation with a liquid of 25 vol.% ethanol + 75 vol.% water. In contact with norcamphor, the liquid forms two separate phases, a saturated ethanol rich phase and a water phase. The fluid inclusions are probably water rich, they are markers for the old cores of the grains that were not swept by a grain boundary. Abnormal grain growth can be observed at the top where two grains grow at the expense of smaller grains.

2.06-2-3-10x: duration 42 hours, width of view 2 mm, T = 25°C.

Like 2.06-1, only with a higher liquid fraction.

**2.09-1+2-5x:** duration 71 hours, width of view 4 mm, T = 25°C.

Nice overview of a statically recrystallizing aggregate starting with a small grain size and a moderate liquid fraction.

**2.10-1-5x:** duration 94 hours, width of view 4 mm, T = 25°C.

Good overview with a moderate to low liquid fraction (sample dries during the experiment), many disequilibrium features. It can be observed that the liquid fraction appears to increase during the grain coarsening, which comes from the liquid which is situated at the grain boundaries. Since the total length of the grain boundaries decreases with increasing mean grain size, more liquid is situated in triple junctions.

2.11-5x: duration 17 hours, width of view 4 mm, T = 25°C.

50 vol.% ethanol + 50 vol.% water.

2.12-5x: duration 71 hours, width of view 4 mm, T = 25°C.

50 vol.% ethanol + 50 vol.% water, somewhat unusual grain growth.

**2.13-1-5x:** duration 220 hours, width of view 4 mm,  $T = 25^{\circ}\text{C}$ .

50 vol.% ethanol + 50 vol.% water. Starts with a varying grain size, although the differences become less pronounced during grain growth, it can still be inferred even after a long time. Towards the end the sample dries up.

2.13-2-5x: duration 152 hours, width of view 4 mm,  $T = 25^{\circ}\text{C}$ .

Continuation of 2.13-1.

**2.14-6-5x:** duration 120 hours, width of view 4 mm,  $T = 20^{\circ}\text{C}$ .

50 vol.% ethanol + 50 vol.% water. Recrystallization, sample starts to dry up towards the end. It is not clear, how the gas gets to some of the spots where bubbles form (oversaturated liquid?).

**2.15-1-10x:** duration 19 hours, width of view 2 mm,  $T = 20^{\circ}\text{C}$ .

50 vol.% ethanol + 50 vol.% water. Similar to 2.06-1, water inclusions trace the old cores of the grains which were not swept by the grain boundaries.

**2.16-1-3-5x:** duration 214 hours, width of view 4 mm,  $T = 25^{\circ}\text{C}$ .

50 vol.% ethanol + 50 vol.% water. Ostwald ripening with a high liquid fraction.

**2.17-10x:** duration 12 hours, width of view 2 mm,  $T = 20^{\circ}\text{C}$ .

This is an experiment with undersaturated liquid. This has the effect of lowering the equilibrium wetting angle to zero (see Chapter 7). The liquid therefore quickly wets all grain boundaries and starts to dissolve them. Shortly afterwards a dissolution front passes that dissolves the whole aggregate. That can possibly be explained by a diffusional dominated system. It takes too much time to dissolve the aggregate from within, after an initial small amount of dissolution the dissolution reaction is restricted by the diffusion of the dissolved matter to the outside of the aggregate. The diffusion front is probably mainly reaction controlled, in this case it is faster to dissolve the aggregate from the outside by the reaction controlled process, than to dissolve it from within by the diffusion controlled process.

**2.19-5x:** duration 24 hours, width of view 4 mm,  $T = 20^{\circ}\text{C}$ .

This is an experiment with undersaturated liquid, similar to 2.17. In the second half of the movie, an opening liquid lens can be observed (see Fig. 7.5). In experiments with saturated ethanol, liquid lenses always have a lowered dynamic or instantaneous wetting angle with regard to the equilibrium angle ( $\theta_{\text{inst}} < \theta_{\text{eq}}$ ), so they always close. However, although the instantaneous angle in this experiment is the same as in experiments with saturated liquid, the equilibrium angle is effectively lowered to zero so that  $\theta_{\text{inst}} > \theta_{\text{eq}}$ , the lens opens and the grain boundary is wetted. Compare with Fig. 7.5.

**2.21:** duration 6 weeks, width of view 8 mm (?), T = 25°C (?).

Long term experiment with high liquid fraction.

**2.22-5x:** duration 13 days, width of view 4 mm, T = 25°C.

Initially dry norcamphor aggregate, that is in contact with saturated ethanol. Since ethanol is a wetting liquid, it is energetically favourable to percolate into the norcamphor layer. Note the initial enhancement of the recrystallization rate that seems to slow down during the rise of the liquid fraction. This is an analogue for the surface energy driven influx of melt into quartzite layers e.g. in migmatites. Melt is mainly produced in the metapelite layers but can thereby percolate in the metapsammities, which can produce an inverted competence contrast between the layers.

**2.22-8-5x:** duration 8 hours, width of view 4 mm, T = 25°C.

The aggregate was first equilibrated with saturated ethanol and subsequently flushed with water. Water has a higher equilibrium wetting angle than ethanol, however, water does not mix with saturated ethanol, so that the experiment is not clear. The wetting angles appear to rise in the beginning, at the same time dissolution takes place, then everything becomes fuzzy.

**2.26-1-5x:** duration 64 hours, width of view 4 mm, T = 25°C.

Grain growth with two layers of grains in the beginning. Interesting are the linear traces of fluid inclusions.

**2.35-1-20x:** duration 62 min, width of view 0,9 mm, T = 25°C.

Recrystallization starting with a very small grain-size. Liquid fraction at the bottom right is lowest and dries up further during the experiment. It is interesting to see that recrystallization in the region with the lowest liquid fraction is fastest (pinning effect of liquid pools), and that the capillary forces are not strong enough to keep up with the drying at the lower right to equalize the liquid fraction in the aggregate (which is energetically favourable for  $\theta_{eq} < 60^\circ$ ). An interesting question concerns the interaction between the capillary forces, that work to equalize the liquid fraction in an aggregate and the faster grain growth and grain boundary migration rate of the regions with less liquid, that might actually work against liquid equilibration distribution.

**2.37-1-10x:** duration 125 min, width of view 2 mm, T = 25°C.

Recrystallization with a moderate liquid fraction and a low starting grain size.

**2.37-2-10x:** duration 770 min, width of view 2 mm, T = 25°C.

see above.

**2.37-3-10x:** duration 28 hours, width of view 2 mm,  $T = 25^{\circ}\text{C}$ .

see above, interesting “wetting“ behaviour of the air bubble.

**2.52-1-5x:** duration 37 hours, width of view 4 mm,  $T = 30^{\circ}\text{C}$ .

Partly crossed polarizers. Note the migrating air bubble and the trace, which is marked by elongated crystals.

**2.57-2-5-10x:** duration 163 hours, width of view 2 mm,  $T = 25^{\circ}\text{C}$ .

Very good example for static grain growth.

## Details

**2.07-20x:** duration 199 hours, width of view 0,9 mm,  $T = 25^{\circ}\text{C}$ .

Disappearance of a small grain. Development of fully wetted grain boundary after a neighbour switch, and subsequent trapping of a liquid lens can be observed. After the grain has disappeared, the liquid slowly reassumes its equilibrium distribution. In this film the formation and result of altered dynamic wetting angles can be observed. Note the subgrain boundary at the liquid pool on the left side of the small grain, that raises the dynamic wetting angle so that the triple junction actually migrates to the left for a short time. Compare with Fig. 4.5.

**2.14-5-50x:** duration 4 min, width of view ??? mm,  $T = 25^{\circ}\text{C}$ .

The last minutes of a disappearing grain. Beautiful liquid lenses.

**2.32-3:** duration 224 min, width of view ??? mm,  $T = 25^{\circ}\text{C}$ .

Formation of a large liquid pool. Compare with Fig. 4.6.

**2.32-5:** duration 17 hours, width of view ??? mm,  $T = 25^{\circ}\text{C}$ .

Disappearance of a grain at a low liquid fraction. Compare with Fig. 4.3.

**2.32-6+7:** duration 16 hours, width of view ??? mm,  $T = 25^{\circ}\text{C}$ .

Disappearance of a grain at a moderate liquid fraction, note the altered dynamic wetting angles. Compare with Figs. 4.4 and 5.15.

**2.55-2-20x:** duration 2 min, width of view 0,9 mm,  $T = 30^{\circ}\text{C}$ .

The last seconds of a dissolving grain at a high liquid fraction. The colour of the norcamphor grains is produced by sticky tape that was used to fix the sample. Note the highly raised dynamic wetting angle between the two grains ( $\theta_{dy} > 90^{\circ}$ ).

**2.55-3-20x:** duration 20 min, width of view 0,9 mm, T = 30°C.

see above.

**2.57-8-20x:** duration 119 hours, width of view 0,9 mm, T = 30°C.

The earlier neighbour switch between the central grain and the grain at the bottom resulted in a fully-wetted grain boundary. Once the grain has disappeared, the disturbed liquid slowly reassumes the stable distribution in triangular liquid pools. Note the dynamically lowered wetting angle at the triple point of the closing grain boundary at the bottom. Compare with Fig. 5.9.

**2.57-9-20x:** duration 20 min, width of view 0,9 mm, T = 25°C.

Last minutes of the disappearance of a small grain. Note the high dynamic wetting angle at the quickly moving triple junctions. The time resolution is too high to observe the liquid redistribution at the other disequilibrium features. Compare with Fig. 5.16.

**2.57-11-20x:** duration 25 hours, width of view 0,9 mm, T = 25°C.

Continuation from 2.57-9, the liquid is redistributed into a more stable configuration. Note the different time scale between 2.57-11 and 2.57-9!

**2.57-17+18-20x:** duration 169 hours, width of view 0,9 mm, T = 25°C.

Disappearance of a grain, the dynamic alteration of the wetting angles are easily observable.

**2.57-19-22-50x:** duration 341 min, width of view ??? mm, T = 25°C.

Disappearance of another grain, the dynamic alteration of the wetting angles are easily observable.

**2.57-27-50x:** duration 21,5 hours, width of view ??? mm, T = 25°C.

As above, note the influence of the subgrain boundary.

**2.57-28-20x:** duration 115 hours, width of view 0,9 mm, T = 25°C.

Disappearance of another grain.

## **Norcamphor–ethanol deformation experiments**

### **High strain rate (Motor A)**

**2.52-2-A-5x:** duration 87 min, width of view 4 mm, T = 30°C.

Once the deformation starts, the grains are pressed against each other and the liquid is pressed out of the sample. The grains are deformed internally and show undulose extinction and develop subgrain boundaries. The grain boundaries become very mobile and sweep over other grains probably driven by strain energy. The aggregate deforms by grain boundary migration recrystallization accommodated dislocation creep. possibly. Note the smaller mean grain size compared to the deformation experiments with a lower strain rate.

### *Experiment 2.53*

**2.53-1-5x:** duration 15 hours, width of view 4 mm, T = 35°C.

Static annealing to create a larger grain size. Interesting because of the uneven grain size at the beginning.

**2.53-2+3-A-5x:** duration 82 min, width of view 4 mm, T = 30°C.

Deformation is by granular flow and localized grain boundary sliding ( $\Delta_{\text{bulk}} > \Delta_{\text{GBS-L}}$ , see Chapter 6) with a slowly decreasing liquid fraction. Note the behaviour of the air bubble, that spreads between the other grain during GBS deformation.

**2.53-4:** duration 29 hours, width of view 4 mm, T = 30°C.

Static annealing of the deformed sample. The air that dispersed among the grains during deformation collects again in an oval bubble. Note the different time scale compared to 2.53-2+3.

**2.53-5-A-10x:** duration 25 min, width of view 2 mm, T = 30°C.

Close up at the air bubble during subsequent deformation. The air spreads again between the adjacent grains. The aggregate starts to deform by framework deformation ( $\Delta_{\text{bulk}} < \Delta_{\text{GBS-L}}$ ) and the air behaves interestingly.

**2.53-6-5x:** duration 49 hours, width of view 4 mm, T = 30°C.

Static annealing of the deformed sample. Very fast initial grain boundary mobility, probably driven by stored strain energy. The result is a strain free foam texture. It is unclear why the air vanishes.

**2.53-7-A-5x:** duration 37 min, width of view 4 mm, T = 26°C.

Deformation of the annealed sample.

**2.53-8-5x:** duration 19 hours, width of view 4 mm, T = 27,5°C.

Annealing of the deformed sample. The final result is a coarse grained aggregate without visible traces of deformation. =>Analogue for quartz ribbons.

*Experiment 2.54*

**2.54-1-5x:** duration 25 hours, width of view 4 mm, T = 30°C.

Static recrystallization of the sample. Interesting is the uneven grain size at the beginning of the experiment.

**2.54-2-5x:** duration 41 hours, width of view 4 mm, T = 30°C.

see above, another area.

**2.54-3-5x:** duration 52 min, width of view 4 mm, T = 30°C.

**2.54-5-5x:** duration 70 hours, width of view 4 mm, T = 30°C.

Static annealing, the grains in the liquid poor areas form a coarse grained strain free foam texture. In the lower right a higher liquid fraction slows the coarsening process by pinning of the grain boundaries.

**2.54-6+7-5x:** duration 54 min, width of view 4 mm, T = 30°C.

Localized grain boundary sliding regime ( $\dot{\epsilon}_{\text{GBS-L}} < \dot{\epsilon}_{\text{bulk}} < \dot{\epsilon}_{\text{GSP}}$ , see Chapter 6). Most of the strain is taken up by small shear zones that are slowly rotating towards the horizontal plane. Note the tendency of the air bubbles to reside in the deforming areas, typical for localized GBS deformation.

**2.54-8-5x:** duration 145 min, width of view 4 mm, T = 30°C.

Static annealing.

### **Medium strain rate (Motor B)**

**2.25-3-5x:** duration 355 min, width of view 4 mm, T = 25°C.

Beautiful grain boundary migration recrystallization accommodated dislocation creep. The old grain boundaries can still be recognized in the beginning of the movie.

**2.27-5x:** duration 19,5 hours, width of view 4 mm, T = 25°C.

Loose lower piston.

**2.34-1-3-5x:** duration 16 hours, width of view 4 mm, T = 25°C (?).

In the beginning some grain rearrangement can be observed before grain boundary migration recrystallization sets in. Note the parallel subgrain boundaries and the episodic transport of the air.

**2.36-1-20x:** duration 20 min, width of view 0,9 mm, T = 25°C.

Static recrystallization with a moderate liquid fraction.

2.36-2-5x: duration 280 min, width of view 4 mm,  $T = 25^{\circ}\text{C}$ .

Deformation and grain boundary migration recrystallization.

**2.36-3+4-5x**: duration 50h, width of view 4 mm,  $T = 25^{\circ}\text{C}$ .

Episodic deformation by grain boundary migration accommodated dislocation creep with subsequent annealing. After every increment of deformation the mean grain size raises much higher than during longer static recrystallization. The largest grain size can therefore be produced by short episodes of deformation followed by longer times of static recrystallization.

**2.50-1-4-5x**: duration 74 hours, width of view 4 mm,  $T = 28^{\circ}\text{C}$ .

Aggregate starts with a small grain size and is deformed by granular flow. The liquid fraction slowly decreases, but the film stops before framework deformation sets in.

**2.51-1-5x**: duration 20 min, width of view 0,9 mm,  $T = 30^{\circ}\text{C}$ .

After a short period of granular flow framework deformation by grain boundary migration recrystallization begins. Compare with Fig. 6.8.

**2.55-4-7-5x**: duration 29 hours, width of view 4 mm,  $T = 30^{\circ}\text{C}$ .

Before the deformation the norcamphor grains form elongated grain aggregates and chains, which is energetically favourable for wetting angles above  $0^{\circ}$ . These chains are broken at the beginning of the deformation. It is easier at high liquid fraction to break the few bonds of the grain aggregates and deform by granular flow than to deform the whole aggregate by crystal plastic deformation (dislocation creep). As the liquid fraction decreases a switch to framework deformation occurs at the stage where it requires less energy to deform the whole framework than to break the bonds between the grains (the GBS-L threshold, see Chapter 6).

**2.56-1-10x**: duration 69 hours, width of view 2 mm,  $T = 40^{\circ}\text{C}$ .

Static recrystallization of norcamphor plus water. Although the temperature is much higher than in the norcamphor-ethanol experiments, the recrystallization rate is much lower. This can possibly be explained by the lower solubility of norcamphor in water and a higher wetting angle. Even after some time the water does not approach an "equilibrium" distribution which is expected for a wetting liquid.

2.56-2-10x: duration 96 hours, width of view 2 mm,  $T = 40^{\circ}\text{C}$ .

Further recrystallization.

**2.56-3+4-10x:** duration 23 hours, width of view 2 mm,  $T = 40^{\circ}\text{C}$ .

Ethanol plus water deformation experiment. The sample deforms by dislocation creep, partly accommodated grain boundary migration recrystallization, although the grain boundaries are less mobile than in norcamphor-ethanol systems. The water acts as a better pinning phase than the ethanol, probably because of the higher wetting angle.

**2.56-5+6-10x:** duration 69 hours, width of view 2 mm,  $T = 40^{\circ}\text{C}$ .

Annealing after the deformation. In the beginning not much happens, then an ethanol (?) liquid front reaches the aggregate and it suddenly forms a foam texture. This is an excellent example for the importance of the nature of the liquid for the microstructure during recrystallization and deformation.

### Low strain rate (Motor C)

**2.24-1+2-10x:** duration 93 hours, width of view 2 mm,  $T = 25^{\circ}\text{C}$ .

Two-layered grain coarsening.

**2.24-3+4-10x:** duration 48 hours, width of view 2 mm,  $T = 25^{\circ}\text{C}$ .

Beginning of the deformation. Interesting is the dynamic spreading of the (non-wetting) air bubbles during deformation.

**2.24-5+6-5x:** duration 95 hours, width of view 4 mm,  $T = 25^{\circ}\text{C}$ .

The aggregate deforms by grain boundary migration accommodated dislocation creep with local grain boundary sliding.

**2.24-7+8-5x:** duration 49 hours, width of view 4 mm,  $T = 25^{\circ}\text{C}$ .

continued from 2.24-5+6.

**2.25-1-3-5x:** duration 215 hours, width of view 4 mm,  $T = 25^{\circ}\text{C}$ .

Deformation is by grain coarsening accommodated compaction. Disappearing small grains leave a gap that is taken up by larger grains. Partly crossed polarizers.

**2.33-1-4-5x:** duration 118 hours, width of view 4 mm,  $T = 25^{\circ}\text{C}$ .

In the beginning of the experiment the sample displays liquid assisted surface energy driven recrystallization. As soon as the sample experiences strain, the norcamphor grains are internally deformed and show undulose extinction and the formation of parallel aligned subgrain boundaries. The grain boundaries become highly mobile and (probably strain energy driven) grain boundary migration recrystallization begins. The grain boundaries sweep over other grains and quickly raise the

grain size up to >1 cm. The liquid is quickly swept out of the aggregate by the migrating grain boundaries, however, it can be observed in the centre of the sample, that the liquid pockets temporarily act as pinning phases, that prevent migration of the grain boundaries. In this film (surface energy driven) static and (strain energy driven) dynamic recrystallisation can be compared: During surface energy driven static grain growth, the grain boundaries always migrate in the direction of their concave side to straighten up, while during dynamic recrystallisation the grain boundaries migrate much faster and often in the opposite direction. Compare with Figs. 6.6 and 7.6.

**2.35-2-3-5x:** duration 142 hours, width of view 4 mm, T = 25°C.

Similar to 2.33-1-4, partly crossed polarizers. Interesting are the many subgrain boundaries that preferably develop perpendicular to the shortening direction.

**2.48-1+2-5x:** duration 98 hours, width of view 4 mm, T = 30°C.

The experiment starts with a high liquid fraction. Initially, the grains coarsen by Ostwald ripening and form aggregates of several grains with common dry grain boundaries. This aggregation is energetically favourable for solid-liquid systems with an equilibrium wetting angle  $>0^\circ$ . Deformation is by granular flow, welded grain boundaries are often destroyed by small shear zones. Compare with Fig. 6.4.

**2.49-1-8-5x:** duration 259 hours, width of view 4 mm, T = 30°C.

Deformation experiment that displays all stages of textural development. In the beginning the grain size increases by Ostwald ripening, which also accommodates the initial compaction of the aggregate. As small grains are dissolved larger grains slide in the remaining voids. The next deformation stage is characterized by granular flow, which is distributed through the whole aggregate in the beginning. As the bulk liquid fraction decreases (below  $\square_{GSP}$ ), the grain boundary sliding localizes in small shear zones, while the grains in between form a coherent cluster. At even lower liquid fraction the whole aggregate forms one coherent cluster that deforms by grain boundary migration accommodated dislocation creep. Compare with Figs. 6.3 and 6.5.

### **KNO<sub>3</sub>–LiNO<sub>3</sub> experiments**

**1-5:** duration 2 hours, image width 2 mm, T = 160°C, motor B.

Deformation experiment with moderate to high melt fraction, the KNO<sub>3</sub> crystals show an angular morphology, deformation is by granular flow.

**1-6+7:** duration 2 hours, image width 2 mm, T = 160°C, motor B.

continued from 1-5. Because of a lower melt fraction, the aggregate deforms by localized grain boundary sliding until a load bearing framework is established that compacts and possibly deforms by diffusion creep (flattened crystals).

**2-1:** duration 21 hours, image width 0,9 mm, T = 160°C, static.

Ostwald ripening with a high melt fraction.

**2-2:** duration 200 min, image width 4 mm, T = 200°C, static.

Grain coarsening in a temperature gradient (T decreases towards the upper left).

**2-3:** duration 2 hours, image width 2 mm, T = 200°C, motor B.

Deformation is by localized grain boundary sliding. Although the initial melt fraction is very low, dynamic porosity is created by the gaps that are created as grains slide past each other, which draws in melt from the edge of the sample. Compare with Fig. 6.9.

**2-4:** duration 158 min, image width 4 mm, T = 200°C, motor B.

Continued from 2-3 with a lower magnification. The sample is deformed by conjugate shear zones that create a raised melt fraction. Progressive deformation slowly increases the bulk melt fraction of the sample. As a result, the deformation becomes less localized and deformation moves towards distributed granular flow. Compare with Fig. 6.10.

**2-5:** duration 20 hours, image width 4 mm, T = 190°C, static.

Static recrystallization of the deformed sample. During annealing, the melt-filled gaps are closed and the melt fraction is lowered again. This characteristic for recrystallization in a temperature gradient, the liquid always migrates towards the hot areas. Note that hardly any traces of the deformation is preserved, although the sample experienced considerable strain (see above).

**3-1:** duration 20 hours, image width 2 mm, T = 190°C, static.

Recrystallization in a temperature gradient. Melt is transported to the hotter top of the movie.

**3-2/3:** duration 27 hours, image width 4 mm, T = 190°C (?), motor C.

Deformation with a low strain rate, low finite strain and a low liquid fraction. The aggregate deforms by surface energy driven recrystallization and grain boundary sliding (?). The air is spread throughout the sample during the deformation.

**4-1:** duration 24 hours, image width 4 mm, T = 200°C, static.

Recrystallization in a small sample. Melt is collected at the edges because of the T gradient.

**4-2:** duration 40 hours, image width 4 mm,  $T = 180^{\circ}\text{C}$ , static.

Continued recrystallization from 4-1.

**4-3:** duration 13 hours, image width 4 mm,  $T = 180^{\circ}\text{C}$ , motor C.

Deformation of the sample by localized grain boundary sliding. The porosity of the sample is increased and the melt that was situated at the edge is distributed within the sample.

**4-4:** duration 36 hours, image width 8 mm,  $T = 180^{\circ}\text{C}$ , static.

Static recrystallization after the deformation.

**5-1:** duration 22 hours, image width 8 mm,  $T = 200^{\circ}\text{C}$ , static.

Static recrystallization of a small sample before deformation.

**5-2:** duration 14 hours, image width 8 mm,  $T = 200^{\circ}\text{C}$ , motor C.

Deformation by grain boundary sliding. Here, the grain coarsening can keep up with the deformation, so that the melt stays at the edge of the sample.

**6-1:** duration 68 hours, image width 4 mm,  $T = 200^{\circ}\text{C}$  (?), motor C.

Grain coarsening accommodated grain boundary sliding with oblique pistons, which produces general shear.

**6-2:** duration 150 hours, image width 8 mm,  $T = 200^{\circ}\text{C}$ , static.

Typical static recrystallization in a  $T$  gradient. Grain boundaries and melt migrate from the colder centre radially towards the hotter edge of the sample. Once the melt is gone, recrystallization is slowed.

**6-3:** duration 102 hours, image width 4 mm,  $T = 200^{\circ}\text{C}$  (?), motor C.

Deformation of the aggregate without melt.

**7-1:** duration 23 hours, image width 4 mm,  $T = (?)$ , motor C.

Surface energy driven grain coarsening accommodated deformation.

**7-2:** duration 25 hours, image width 4 mm,  $T = (?)$ , motor C.

Continued from 7-1.

**8-1:** duration 45 hours, image width 0,9 mm,  $T = 200^{\circ}\text{C}$  (?), static.

Melt segregation along a thermal gradient, the melt migrates along the grain edges or even through the grains. Once the melt is segregated, a foam texture of nitrate grains is left over that hardly recrystallizes any more.

**9-1:** duration 19 hours, image width 0,9 mm,  $T = 200^{\circ}\text{C}$  (?), static.

Ostwald ripening in a small sample. Interesting is, that the grains with a hexagonal morphology and crystal facets grow much faster than the grains with rounded grain boundaries.

**10-1:** duration 20 hours, image width 4 mm,  $T = 200^{\circ}\text{C}$  (?), static.

Static recrystallization in a thermal gradient.

**10-2:** duration 6 hours, image width 0,9 mm,  $T = 200^{\circ}\text{C}$  (?), static.

Continued from 10-1 with a higher magnification.

**11-1:** duration 40 hours, image width 4 mm,  $T = 200^{\circ}\text{C}$  (?), static.

Grain growth around an aluminium piston.

**12-2:** duration 48 hours, image width 4 mm,  $T = (?)$ , motor C.

Simulation of an opening gap with melt and air influx.

**13-1:** duration 2 hours, image width 4 mm,  $T = 200^{\circ}\text{C}$  (?), motor C.

Simulation of an opening gap with melt and air influx.

**14-1:** duration 20 hours, image width 0,9 mm,  $T = (?)$ , static.

recrystallization

**15-1:** duration 43 hours, image width 0,9 mm,  $T = 200^{\circ}\text{C}$  (?), static.

Recrystallization in a thermal gradient. Note the grain boundary migration recrystallization at low melt fraction. The exact mechanism is unclear, however, it always occurs at low melt fraction combined with a thermal gradient.

**16-1:** duration 10 hours, image width 0,9 mm,  $T = 180^{\circ}\text{C}$  (?), static.

Ostwald ripening at a high melt fraction. Note the formation of grain aggregates that suggests a finite non-zero wetting angle in the nitrate-melt system.

**16-2:** duration 60 hours, image width 0,9 mm,  $T = 180^{\circ}\text{C}$ , static.

Formation of a grain aggregate at the colder side of the sample.

**16-3:** duration 47 hours, image width 0,9 mm, T = 180°C, static.

Continued from 16-2. Now, the sample displays grain boundary migration recrystallization. This is always the result of very low melt fraction in a thermal gradient.

**17-1:** duration 48 hours (?), image width 2 mm, T = (?), motor C (?).

Surface energy driven grain coarsening and possibly diffusion creep accommodated deformation. Note the spreading behaviour of the air during deformation. Compare with Fig. 7.6.

19-2: duration 24 hours, image width 2 mm, T = (?), Motor (?).

19-3: duration 24 hours, image width 2 mm, T = (?), static.

19-4: duration 24 hours, image width 2 mm, T = (?), Motor C.

21-1: duration 45 hours, image width 0,9 mm, T = (?), static.

Recrystallization

21-2: duration 180 hours, image width 2 mm, T = (?), static.

Recrystallization

21-2: duration 180 hours, image width 2 mm, T = (?), static.

**22-1:** duration 17 hours, image width 0,9 mm, T = (?), static.

Recrystallization. The second liquid that spreads around the sample is silicone grease.

**23-1:** duration 23 hours, image width 0,9 mm, T = (?), static.

Ostwald ripening with a high melt fraction. The angular grains with crystal facets slowly develop round morphology with curved boundaries.

**23-2+3:** duration 112 hours, image width 0,9 mm, T = (?), static.

Continued from 23-1. The grains form a cluster at the lower side of the sample, which is the “coldest” part. The solid fraction slowly decreases, possibly by dissipation of the nitrates.

24-1: duration 112 hours, image width 0,9 mm, T = (?), static.

**25-2:** duration 48 hours, image width 2 mm, T = (?), motor C.

Deforming sample with a moderate melt fraction, the grains have an irregular shape. Deformation is by grain boundary sliding, in the end a framework is formed that compacts and possibly deforms by diffusion creep (pressure solution?).

25: duration 10 days, image width 0,9 mm, T = (?), static.

Static Ostwald ripening and rearrangement at moderate to high melt fraction.

26-2: duration 24 hours, image width 0,9 mm, T = 190°, static.

Static grain growth.

26-3: duration 20 hours, image width 0,9 mm, T = 190°, static.

Continued from 26-2, the effect of the thermal gradient and the melt migration can be observed.

26-4: duration 90 hours, image width 4 mm, T = 137°, motor C.

Deformation mainly by compaction and by conjugate shear zones.

26-5: duration 30 hours, image width 2 mm, T = 150°, motor C.

27-1: duration 32 hours, image width 0,9 mm, T = 200°, static.

Static recrystallization

**31-1:** duration 25 hours, image width 0,9 mm, T = 192°, static.

Static grain coarsening in a thermal gradient. The melt migrates towards the upper left which is the hottest region in the field of view. The thermal gradient and the liquid migration probably also produce the grain boundary migration recrystallization, that can be observed.

**31-2:** duration 62 hours, image width 2 mm, T = 190°, static.

Unusual static grain boundary migration recrystallization. This kind of recrystallization can normally be observed in high temperature deformation environments during dislocation creep. However, the driving mechanism seems to come from the thermal gradient and the melt behaviour in the gradient, it is however, not explained in detail, yet.

**31-3:** duration 94 hours, image width 2 mm, T = 192°, motor C.

Low strain rate deformation at a low melt fraction. The sample deforms at localized grain boundary sliding shear zones and by flattening of the grains, possibly by diffusion creep.

**32-1+2:** duration 110 hours, image width 2 mm, T = 192°, static.

This movie shows all stages of texture development that can be observed in partially molten nitrates in a thermal gradient. The sample starts with Ostwald ripening at a small grain size and a high melt fraction, so that the mean grain size increases. At the same time the melt fraction decreases because the melt migrates towards the hottest area out of the field of view (to the upper left in the movie). Once the grains touch each other, the melt cannot migrate freely anymore, so that the grains are directly affected by the liquid migration. This is probably the driving mechanism for the grain boundary migration recrystallization, that is active as long as there is any melt left. Once the aggregate is melt-free, the grain boundaries suddenly straighten up and a stable foam texture is produced.

**34-1-3:** duration 133 hours, image width 0,9 mm, T = (?), static.

see 32-1+2.

**35-1+2:** duration 119 hours, image width 0,9 mm, T = 188°C, static.

see 32-1+2.

**36:** duration 119 hours, image width ca. 1cm, T = 180°C, motor C.

Experiment to investigate the development of microboudinage in partially-molten samples. The boudins are made of aluminium foil and are placed in the sample. They are separated by the pure shear deformation. The boudin neck opens during progressive deformation, however, no melt collects in the boundin neck but the aggregate migrates into the opening gap by a graular flow mechanism. The last part of the film is characterized by a flattening of the crystals, possibly by diffusional creep.

**37-1+2:** duration 123 hours, image width ca. 1 cm, T = 155°C, Motor C.

Similar to 36 with broader microboundins. In the beginning of the deformation the area below the boudins deforms by compaction (framework deformation), once the melt fraction is sufficiently low grain boundary migration recrystallization sets in, which results in a sudden dramatic increase of the grain size. This part is now more competent than the rest of the sample, so that the boudins now open in an oblique way. Melt and grains are flowing into the boudin neck from above along small shear zones that deform by grain boundary sliding.

**38:** duration 12 hours 40 min, image width ca. 1 cm, T = (?), motor B.

Similar to 36 with a higher strain rate. The boudins are separated by discrete shear zones, the development of a large grain by grain boundary migration can be observed below the left boudin. This “sudden“ grain growth often occurs in the nitrate experiments at framework deformation with a low melt fraction. Compare with Fig. 6.11.

**39:** duration 26 hours, image width ca. 1 cm, T = 200°C, motor B.

Similar to 37. The boudins open obliquely and the solid-melt aggregate flows into the opening neck along shear zones that deform by grain boundary sliding. The common observation of all experiments with microboudins is, that there is no melt segregation in the boudin necks, as can often be observed in nature (melt or quartz precipitated from a fluid). This shows that no melt segregation occurs in the deforming areas during granular flow or grain boundary sliding dominated deformation. Granular flow rather keeps the grains dispersed in the melt, as in a magma.

40-1+2: duration 75 hours, image width 2 mm, T = 200°C, static.

Static recrystallization in a thermal gradient.

40-3: duration 2 hours, image width 2 mm, T = 170°C, static.

continued from 40-1+2.

**40-4:** duration 26 hours, image width ca. 1 cm, T = 160°C, motor B.

Similar to experiment 36 with microboudins. The grain-melt aggregate flows into the opening boudin neck along two conjugate grain boundary sliding shear zones. Note that after the deformation hardly any traces of the deformation mechanism are preserved.

**41-1:** duration 40 hours, image width 2 mm, T = 200°C, static.

Static recrystallization with the hot part of the sample at the bottom.

**41-2:** duration 150 hours, image width ca. 1 cm, T = 200°C, static.

Similar to 40-4. Probably because of the lower strain rate (and the lower liquid fraction?) no localized shear zones are formed, the aggregate flows rather into the opening boudin neck by distributed granular flow, possibly partly accommodated by diffusion creep.

**45-1:** duration 17 hours, image width ca. 1 cm, T = (?), static.

A somewhat unusual behaviour during recrystallization.

**45-2:** duration 26 hours, image width ca. 1 cm, T = (?), motor B.

Semi-brittle deformation of the aggregate.

**46-1:** duration 24 hours, image width ca. 1 cm, T = 200, motor B.

Semi-brittle deformation of the aggregate without melt. Note the beautiful deformation twins that develop in the beginning of the strain (analogue for calcite).

**47:** duration 119 hours, image width ca. 1 cm, T = (?), motor C.

Semi-brittle deformation of the aggregate, very unusual grain boundary behaviour.

**48:** duration 84 hours, image width 4 mm, T = 200°C, motor C.

Semi-brittle deformation of a melt-free aggregate with a starting foam text



## References

- Aksay, I.A., Hoge, C.E., Pask, J.A., 1974. Wetting under chemical equilibrium and nonequilibrium conditions. *Journal of Physical Chemistry* 78, 1178-1183.
- Allaby, M., Allaby, A. (Eds.), 1990. *The concise Oxford dictionary of Earth sciences*. Oxford University Press, Oxford, 410 pp.
- Anderson, M.P., 1988. Simulation of grain growth in two and three dimensions, In: Hansen, N., et al. (Eds.), *Recovery, recrystallization and grain growth*. Roskilde, Riso National Laboratory, pp. 15-34
- Arnold, J., Jacoby, W.R., Schmeling, H., Schott, B., 2001. Continental collision and the dynamic and thermal evolution of the Variscan orogenic crustal root - numerical models. *Journal of Geodynamics* 31, 273-291.
- Arzi, A.A., 1978. Critical phenomena in the rheology of partially melted rocks. *Tectonophysics* 44, 173-184.
- Atkinson, H.V., 1988. Overview no. 65: theories of normal grain growth in pure single phase systems. *Acta Metallica* 36, 469-492.
- Bagdassarov, N., Dorfman, A., 1998. Granite rheology: magma flow and melt migration. *Journal of the Geological Society London* 155, 863-872.
- Barcilon, V., Richter, F.M., 1986. Non-linear waves in compacting media. *Journal of Fluid Mechanics* 164, 429-448.
- von Bargen, N., Waff, H., 1986. Permeabilities, interfacial areas and curvatures of partially molten systems: Results of numerical computations of equilibrium microstructures. *Journal of Geophysical Research* 91, 9261-9276.
- Bauer, P., Rosenberg, C., Handy, M.R., 2000. 'See-through' deformation experiments on brittle-viscous norcamphor at controlled temperature, strain rate and applied confining pressure. *Journal of Structural Geology* 22, 281-289.
- Bear, J., 1972. *Dynamics of Fluids in Porous Media*, Dover Publications, New York.
- Becker, J.K., Koehn, D., Walte, N.P., Jessel, M., Bons, P.D., Passchier, C.W., Evans, L., 2003. Numerical simulation of disequilibrium microstructures in solid-melt systems during grain growth. *Journal of the Virtual Explorer*, 11.
- Bergantz, G.W., 1989. Underplating and partial melting: Implications for melt generation and extraction. *Science* 245, 1093-1095.
- Best, M.G., 2003. *Igneous and metamorphic petrology*. Blackwell Publishing, 729 pp.
- Bons, P.D., 1993. Experimental deformation of polyphase rock analogues. *Geologica Ultraiectina* 110, Utrecht.
- Bons, P.D., Jessell, M.W., Passchier, C.W., 1993. The analysis of progressive deformation from dispersed marker-particles. *Journal of Structural Geology* 15, 403-411.
- Bons, P.D., Jessell, M.W., Evans, L., Barr, T.D., Stüwe, K., 2001. Modelling of anisotropic grain growth in minerals, In: Koyi, H.A., Mancktelow, N.S. (eds.), *Tectonic Modeling: A Volume in Honor of Hans Ramberg*, Geological Society of America Memoir 193, 39-49.
- Bons, P.D., van Milligen, B.P., 2001. New experiment to model self-organized critical transport and accumulation of melt and hydrocarbons from their source rocks. *Geology* 29, 919-922.
- Bons, P.D., Arnold, J., Elburg, M.A., Kalda, J., Soesoo, A., van Milligen, B.P. Melt extraction and accumulation from partially molten rocks, in press *Lithos*
- de Bresser, J.H.P., Peach, C.J., Reijs, J.P.J., Spiers, C.J., 1998. On dynamic recrystallization during solid state flow: Effects of stress and temperature *Geophysical Research Letters* 25, 3457-3460.
- Brown, M., 1994. The generation, segregation, ascent and emplacement of granite magma: the migmatite-to-crustally-derived granite connection in thickened orogens. *Earth-Science Reviews* 36, 83-130.
- Brown, M., 2001. Orogeny, migmatites and leucogranites: A review. *Proceedings of the Indian Academy of Science (Earth and Planetary Science)* 110, 313-336.

- Brown, M., Rushmer, T., 1997. The role of deformation in the movement of granitic melt: views from the laboratory and the field. In: Holness, M. B. (Ed.), *Deformation enhanced Fluid Transport in the Earth's Crust and Mantle*. The Mineralogical Society Series 8, Chapman and Hall, London, pp. 111-144.
- Brown, M., Solar, G., 1998. Shear-zone systems and melts: feedback relations and self-organization in orogenic belts. *Journal of Structural Geology* 20, 211-227.
- Bruhn, D., Groebner, N., Kohlstedt, D.L., 2000. An interconnected network of core-forming melts produced by shear deformation. *Nature* 403, 883-886.
- Bulau, J.R., Waff, H.S., Tyburczy, J.A., 1979. Mechanical and thermodynamical constraints on fluid distribution in partial melts. *Journal of Geophysical Research* 84, 6102-6108.
- Bureau, H., Keppler, H., 1999. Complete miscibility between silicate melts and hydrous fluids in the upper mantle; experimental evidence and geochemical implications. *Earth and Planetary Science Letters* 165, 187-196.
- Carlson, W.D., 1999. The case against Ostwald ripening of porphyroblasts. In: Rivers, T., Pattison, D.R.M., Martin, R.F. (Eds.), *Mineral-scale processes in metamorphic petrology, the Kretz volume*. *The Canadian Mineralogist* 37, 403-413.
- Carman, P.C., 1956. *Flow of Gases Through Porous Media*, Academic Press, New York, 182 pp.
- Chamberlain, C.P., Sonder, L.J., 1990. Heat-producing elements and the thermal and baric patterns of metamorphic belts. *Science* 250, 763-769.
- Clemens, J.D., Mawer, C.K., 1992. Granitic magma transport by fracture propagation. *Tectonophysics* 204, 339-360.
- Cmíral, M., Fitz Gerald, J.D., Faul, U.H., 1998. A close look at dihedral angles and melt geometry in olivine-basalt aggregates: A TEM study. *Contributions to Mineralogy and Petrology* 130, 336-345.
- Connolly, J.A.D., Podladchikov, Y.Y., 2004. Fluid flow in compressive tectonic settings: Implications for midcrustal seismic reflectors and downward fluid migration. *Journal of Geophysical Research* 109, doi: 10.1029/JB002822.
- Daines, M.J., 1997. Melt distribution in partially molten peridotites: implications for permeability and melt migration in the upper mantle. In: Holness, M.B. (Ed.), *Deformation-enhanced fluid transport in the Earth's crust and mantle*, Chapman & Hall, London, 62-81.
- Daines, M.J., Kohlstedt, D.L., 1997. Influence of deformation on melt topology in peridotites. *Journal of Geophysical Research* 102, 10257-10271.
- Davies, J.H., Bickle, M.J., 1991. A physical model for the volume and composition of melt produced by hydrous fluxing above subduction zones. *Philosophical Transaction of the Royal Society of London* 335, 355-364.
- Dell'Angelo, L.N., Tullis, J., 1988. Experimental deformation of partially melted granitic aggregates. *Journal of Metamorphic Geology* 6, 495-515.
- Einstein, A., 1906. Eine neue Bestimmung der Moleküldimensionen. *Annalen der Physik* 19, 289-306.
- Ellis, D.J., Obata, M., 1992. Migmatite and melt segregation at Cooma, New South Wales. In: Brown, P.E., Chappel, B.W. (Eds.), *The second Hutton symposium on the origin of granites and related rocks, proceedings, Special Paper - Geological Society of America* 272, 95-106.
- England, P.C., Thompson, A.B., 1984. Pressure-temperature-time paths of regional metamorphism, I, Heat transfer during the evolution of regions of thickened continental crust. *Journal of Petrology* 25, 894-928.
- England, P.C., Thompson, A.B., 1986. Some thermal and tectonic models for crustal melting in continental collision belts. In: Coward, M.P., Ries, A.C. (Eds.), *Collision tectonics*, Geological Society Special Publication, London.
- Evans, B., Renner, J., Hirth, G., 2001. A few remarks on the kinetics of static grain growth in rocks. *International Journal of Earth Science* 90, 88-103.

- Faul, U.H., 1994. Intergranular basaltic melt is distributed in thin, elongated inclusions. *Geophysical research Letters* 21, 29-32.
- Faul, U.H., 1997. Permeability of partially molten upper mantle rocks from experiments and percolation theory. *Journal of Geophysical Research* 102, 10299–10311.
- Faul, U.H., 2000. Constraints on the melt distribution in anisotropic polycrystalline aggregates undergoing grain growth. In: Bakdassarov, N., et al. (Eds.), *Physics and chemistry of partially molten rocks*, Dordrecht, Kluwer Academic Publications, 67–92.
- Faul, U.H., 2001. Melt retention and segregation beneath mid-ocean ridges. *Nature* 410, 920–921.
- de Gennes, P.D., 1985. Wetting: statistics and dynamics. *Reviews of Modern Physics* 57, 827-863.
- Ghods, A., Arkani-Hamed, J., 2000. Melt migration beneath mid-ocean ridges. *Geophysical Journal International* 140, 687-697.
- Glazier, J.A., Stavans, J., 1989. Nonideal effects in the two-dimensional soap froth. *Physical review A* 40, 7398-7401.
- Gleason, G.C., Bruce, V., Green, H.W., 1999. Experimental investigation of melt topology in partially molten quartzo-feldspathic aggregates under hydrostatic and non-hydrostatic stress. *Journal of metamorphic Geology* 17, 705-722.
- Gray, G.W., Winsor, P.A., 1974. *Liquid crystals & Plastic crystals*, volume 1. John Wiley & Sons, New York.
- Guizani, M., Zamali, H., Jemal, M., 1998. The  $\text{KNO}_3\text{-LiNO}_3$  phase diagram. *Comptes Rendus de l'Academie des Sciences* 1, 787-789.
- Handy, M.R., Mulch, A., Rosenau, M., Rosenberg, C.L., 2001. The role of fault zones and melts as agents of weakening, hardening and differentiation of the continental crust: a synthesis. In: Holdsworth, R.E., Strachan, R.A., Magloughlin, J.F., Knipe, R.J. (Eds.). *The nature and tectonic significance of fault zone weakening*. Geological Society, London, Special Publications 186, 305-332.
- Herweg, M., Handy, M.R., 1996. The evolution of high-temperature mylonitic microfabrics: Evidence from simple shearing of a quartz analogue (norcamphor). *Journal of Structural Geology* 18, 689–710.
- Higgins, M.D., 1999. Origin of megacrysts in granitoids by textural coarsening, a crystal size distribution (CSD) study of microcline in the Cathedral Peak Granodiorite, Sierra Nevada, California. In: Castro, A., Fernandez, C., Vigneresse, J.L. (Eds.), *Understanding granites, integrating new and classical techniques*, Geological Society Special Publication 168, 207-219.
- Hippert, J., Rocha, A., Lana, C., Egydio-Silva, M., Takeshita, T., 2001. Quartz plastic segregation and ribbon development in high-grade striped gneisses. *Journal of Structural Geology* 23, 67-80.
- Hirth, G., Tullis, J., 1992. Dislocation creep regimes in quartz aggregates. *Journal of Structural Geology* 14, 145-159.
- Hirth, G., Kohlstedt, D.L., 1995a. Experimental constraints on the dynamics of the partially molten upper mantle: Deformation in the diffusion creep regime. *Journal of Geophysical Research* 100, 1981-2001.
- Hirth, G., Kohlstedt, D.L., 1995b. Experimental constraints on the dynamics of the partially molten upper mantle: Deformation in the dislocation creep regime. *Journal of Geophysical Research* 100, 15441-15449.
- Holness, M.B., 1996. Surface-chemical controls on pore-fluid connectivity. In: Jamtveit, B., Yardly, W.D. (Eds.), *Fluid Flow and Transport in Rocks: Mechanisms and Effects*, Chapman & Hall.
- Holness, M.B., Siklos, S.T.C., 2000. The rates and extent of textural equilibrium in high-temperature fluid-bearing systems. *Chemical Geology*, 162, 137-153.
- Holtzman, B.K., Groebner, N.J., Zimmerman, M.E, Ginsberg, S.B. and Kohlstedt, D.L., 2003a. Stress-driven melt segregation in partially molten rocks. *Geochemistry, Geophysics, Geosystems* 4, 8607, doi:10.1029/2001GC000258.

- Holtzman, B.K., Kohlstedt, D.L., Zimmerman, M.E., Heidelbach, F., Hiraga, T., Hustoft, J., 2003b. Melt segregation and strain partitioning: implications for seismic anisotropy and mantle flow. *Science* 103, 1227-1230.
- Holyoke, C.W., Rushmer, T., 2002. An experimental study of grain scale melt segregation mechanisms in two common crustal rock types. *Journal of metamorphic Geology* 20, 493-512.
- Huppert, H.E., Sparks, S.J., 1988. The generation of granitic magmas by intrusion of basalt into continental crust, *J. Petr.* 29, 599-624.
- Jung, H., Waff, H.S., 1998. Olivine crystallographic control and anisotropic melt distribution in ultramafic partial melts. *Geophysical Research Letters* 25, 2901-2904.
- Jurewicz, S.R., Watson, E.B., 1985. The distribution of partial melt in a granitic system, the application of liquid phase sintering theory. *Geochimica et Cosmochimica Acta* 49, 5, 1109-1121.
- Karato, S.I., 1989. Grain growth kinetics in olivine aggregates. *Tectonophysics* 168, 255-273.
- Kelemen, P.B., Hirth, G., Shimizu, N., Spiegelman M., Dick, H.J.B., 1997. A review of melt migration processes in the asthenospheric mantle beneath oceanic spreading centers. *Philosophical Transactions of the Royal Society London* 355, 283-318.
- Keszthelyi, L.P. and the Galileo Solid State Imaging Team., 2001. Imaging of volcanic activity on Jupiter's moon Io by Galileo during the Galileo Europa Mission and the Galileo Millennium Mission. In: McEwen, A.S. (Prefacer), *Geology and geophysics of Io*. *Journal of Geophysical Research, E, Planets* 106, 33025-33052.
- Kohlstedt, D.L., 1992. Structure, rheology and permeability of partially molten rocks at low melt fractions. In: Morgen, P.G., et al. (Eds.), *Mantle flow and melt generation at mid-ocean ridges*, American Geophysical Union Geophysical Monograph 71, 103-121.
- Laporte, D., 1994. Wetting behaviour of partial melts during crustal anatexis: the distribution of hydrous silicic melts in polycrystalline aggregates of quartz. *Contributions to Mineralogy and Petrology* 116, 486-499.
- Laporte, D., Provost, A., 2000a. The grain-scale distribution of silicate, carbonate and metallosulfide partial melts: A review of theory and experiments. In: Bakssarov, N., et al. (Eds.), *Physics and chemistry of partially molten rocks*, Dordrecht, Kluwer Academic Publications, 93-140.
- Laporte, D., Provost, A., 2000b. Equilibrium geometry of a fluid phase in a polycrystalline aggregate with anisotropic surface energies, dry grain boundaries. *Journal of Geophysical Research* 105, 25937-25953.
- Laporte, D., Watson, E.B., 1995. Experimental and theoretical constraints on melt distribution in crustal sources: The effect of crystalline anisotropy on melt interconnectivity. *Chemical Geology* 124, 161-184.
- Laporte, D., Rapaille, C., Provost, A., 1997. Wetting angles, equilibrium melt geometry, and the permeability threshold of partially molten crustal protoliths. In: Bouchez, J.L., Hutton, D.H.W., Stephens, W.E. (Eds.), *Granite: From segregation of melt to emplacement fabrics*. Kluwer Academic Publications, Dordrecht, 31-54.
- Léger, L., Joanny, J.F., 1992. Liquid spreading. *Rep. Prog. Physics* 55, 431-486.
- Leshner, C.E., Walker, D., 1988. Cumulate maturation and melt migration in a temperature gradient. *Journal of Geophysical Research* 93, 10295-10311.
- Lifshitz, I.M., Slyozov, V.V., 1961. The kinetics of precipitation from supersaturated solid solutions. *Journal of Physics and Chemistry of Solids* 19, 35-50.
- Marchildon, N., Brown, M., 2002. Grain-scale melt distribution in two contact aureole rocks: implications for controls on melt localization and deformation. *Journal of Metamorphic Geology* 20, 381-396.
- McCrone, W.C., 1949. Boundary migration and grain growth. *Disc. Faraday Society* 5, 158-166.
- McKenzie, D., 1984. The generation and compaction of partially molten rock. *Journal of Petrology* 25, 713-765.

- McKenzie, D., 1987. The compaction of igneous and sedimentary rocks. *Journal of the Geological Society, London* 144, 299–307.
- McKenzie, D., Bickle, M.J., 1988. The volume and composition of melt generated by extension of the lithosphere. *Journal of Petrology* 29, 625–679.
- Means, W.D., 1989. Synkinematic microscopy of transparent polycrystals. *Journal of Structural Geology* 11, 163-174.
- Means, W.D., Park, Y., 1994. New experimental approach to understanding igneous texture. *Geology* 22, 323-326.
- Mecklenburgh, J., Rutter, E.H., 2003. On the rheology of partially molten synthetic granite. *Journal of Structural Geology* 25, 1575-1585.
- Mei, S., Bai, W., Hiraga, T., Kohlstedt, D.L., 2002. Influence of melt on the creep behaviour of olivine-basalt aggregates under hydrous conditions. *Earth and planetary science letters* 201, 491-507.
- Miyazaki, K., 1991. Ostwald ripening of garnet in high P/T metamorphic rocks. *Contributions to Mineralogy and Petrology* 108, 118-128.
- van der Molen, I., Paterson, M.S., 1979. Experimental deformation of partially-melted granite. *Contributions to Mineralogy and Petrology* 70, 299-318.
- Obata Masaaki, Takazawa Eiichi, 2004. Composition continuity and discontinuity in the Horoman Peridotite, Japan, and its implication for melt extraction processes in partially molten upper mantle. *Journal of Petrology* 45, 223-234.
- O’Nions, K., McKenzie, D., 1993. Estimates of mantle thorium/uranium ratios from Th, U and Pb isotope abundances in basaltic melts. In: Cox, K.G., McKenzie, D., White, R.S. (Eds.), *Melting and melt movement in the Earth*. Philosophical Transactions of the Royal Society of London A 342, 65-77.
- Ono Shigeaki, Mibe Kenji, Yoshino Takashi, 2002. Aqueous fluid connectivity in pyrope aggregates, water transport into the deep mantle by a subducted oceanic crust without any hydrous minerals. *Earth and Planetary Science Letters* 203, 895-903.
- Ostwald, W., 1901. *Analytische Chemie*. Engelmann, Leipzig.
- Park, Y., Means, W.D., 1996. Direct observation of deformation processes in crystal mushes. *Journal of Structural Geology* 18, 847-858.
- Passchier, C.W., Trow, R., 1996. *Microtectonics*. Springer, Berlin, Heidelberg, New York, 289 pp.
- Paterson, M.S., 2001. A granular flow theory for the deformation of partially molten rock. *Tectonophysics* 335, 51-61.
- Paterson, S.R., Vernon, R. H., 1995. Bursting the bubble of ballooning plutons: a return to nested diapirs emplaced by multiple processes. *Geological Society of America Bulletin* 107, 1356-1380.
- Petford, N., Koenders, M.A., 1998. Granular flow and viscous fluctuations in low Bagnold number granitic magmas. *Journal of the Geological Society, London* 155, 873-881.
- Rabinowicz, M., Genthon, P., Ceuleneer, G., Hillairet, M., 2001. Compaction in a mantle mush with high melt concentrations and the generation of magma chambers. *Earth and Planetary Science Letters* 188, 313-328.
- Renner, J., Evans, B., Hirth, G., 2000. On the rheological critical melt fraction. *Earth and planetary science letters* 181, 585-594.
- Renner, J., Evans, B., Hirth, G., 2002. Grain growth and inclusion formation in partially molten carbonate rocks. *Contributions to Mineralogy and Petrology* 142, 501-514.
- Richter, F.M., McKenzie, D., 1984. Dynamic models for melt segregation from a deformable matrix. *Journal of Geology* 92, 729-740.
- Rosenberg, C.L., 2001. Deformation of partially molten granite, a review and comparison of experimental and natural case studies. In: Dresen, G., Handy, M., (Eds.). *Deformation mechanisms, rheology and microstructures*. *International Journal of Earth Sciences* 90, 60-76.

- Rosenberg, C.L., Handy, M.R., 2000. Syntectonic melt pathways during simple shearing of a partially molten rock analogue (norcamphor-benzamide). *Journal of Geophysical Research* 105, 3135–3149.
- Rosenberg, C.L., Riller, U., 2000. Partial-melt topology in statically and dynamically recrystallized granite. *Geology* 28, 7–10.
- Rosenberg, C.L., Handy, M.R., 2001. Mechanisms and orientation of melt segregation paths during pure shearing of a partially molten rock □□□□□□(norcamphor-benzamide). *Journal of Structural Geology* 23, 1917–1932.
- Rutter, E.H., 1997. The influence of deformation on the extraction of crustal melts: a consideration of the role of melt-assisted granular flow. In: Holness, M.B. (Ed.), *Deformation enhanced Fluid Transport in the Earth's Crust and Mantle*. The Mineralogical Society Series 8, Chapman and Hall, London, 82–110.
- Rutter, E.H., Neumann, D.H.K., 1995. Experimental deformation of partially molten westerly granite under fluid-absent conditions, with implications for the extraction of granitic magmas. *Journal of Geophysical Research* 100, 15697–15715.
- Ryerson, F.J., Weed, H.C., Piwinski, A.J., 1988. Rheology of subliquidus magmas 1, Picritic compositions. *Journal of Geophysical Research* 93, 3421–3436.
- Sawyer, E., 2001. Melt segregation in the continental crust: distribution and movement of melt in anatectic rocks. *Journal of Metamorphic Geology* 19, 291–309.
- Schmeling, H., 1986. A simple statistical model on the degree of interconnection in partially molten rocks. *Journal of Geophysics* 59, 142–145.
- Schmeling, H., 2000. Partial melting and melt segregation in a convecting mantle. In: Bagdassarov, N., Laporte, D., Thompson, A.B. (Eds.), *Physics and chemistry of partially molten rocks*. Kluwer, 141–178.
- Schott, B., Schmeling, H., 1998. Delamination and detachment of a lithospheric root. *Tectonophysics* 296, 225–247.
- Scott, D., Stevenson, D., 1986. Magma ascent by porous flow. *Journal of Geophysical Research* 91, 9283–9296.
- Smith, C.S., 1964. Some elementary principles of polycrystalline microstructure. *Metallurgical Review* 9, 1–48.
- Spence, D.A., Turcotte, D.L., 1990. Buoyancy-driven magma fracture: A mechanism for ascent through the lithosphere and the emplacement of diamonds. *Journal of Geophysical Research* 95, 5133–5139.
- Stephenson, I.M., White, J., 1967. Factors controlling microstructure and grain growth in two-phase (one solid + one liquid) and in three-phase (two solid + one liquid) systems. *Transactions of the British Ceramic Society* 66, 443–483.
- Stevenson, D., 2000. Europa's ocean, the case strengthens. *Science* 289, 1305–1307.
- Stipp, M., Stünitz, H., Heilbronner, R., Schmid, S.M., 2002. Dynamic recrystallization of quartz, correlation between natural and experimental conditions. In: de Meer, S., Drury, M.R., de Bresser, J.H.P., Pennock, G.M. (Eds.), *Deformation mechanisms, rheology and tectonics, current status and future perspectives*. Geological Society Special Publications 200, 171–190.
- Stipp, M., Stünitz, H., Heilbronner, R., Schmid, S., 2002. The eastern tonalite fault zone: a 'natural laboratory' for crystal plastic deformation of quartz over a temperature range from 250 to 700°C. *Journal of Structural Geology* 24, 1861–1884.
- Storre, B., 1972. Dry melting of muscovite plus quartz in the range  $P_s = 7$  GPa to  $P_s = 20$  GPa. *Contributions to Mineralogy and Petrology* 37, 87–89.
- Thomas, R., Webster, J.D., Heinrich, W., 2000. Melt inclusions in pegmatite quartz; complete miscibility between silicate melts and hydrous fluids at low pressure. *Contributions to Mineralogy and Petrology* 139, 394–401.
- Thompson, A.B., 1982. Dehydration melting of pelitic rocks and the generation of H<sub>2</sub>O-undersaturated granitic liquids. *American Journal of Science* 282, 1567–1595.
- Tullis, J., Jund, R., Farver, J., 1996. Deformation-enhanced fluid distribution in feldspar aggregates and implications for ductile shear zones. *Geology* 24, 63–66.

- Tungatt, P.D., Humphreys, F.J., 1981. An in-situ optical investigation of the deformation behaviour of sodium nitrate, an analogue for calcite. In: Lister, G.S., Behr, H.J., Weber, K., Zwart, J.J. (Eds.), *The effect of deformation on rocks*. Tectonophysics 78, 661-675.
- Tungatt, P.D., Humphreys, F.J., 1984. The plastic deformation and the dynamic recrystallization of polycrystalline sodium nitrate. *Acta Metallica* 32, 1625-1635.
- Urai, J.L., 1983. Deformation of wet salt rocks: an investigation into the interaction between mechanical properties and microstructural processes during deformation of polycrystalline carnallite and bischofite in the presence of a pore fluid. PhD Thesis, University of Utrecht.
- Urai, J.L., Means, W.D., Lister, G.S., 1986. Dynamic recrystallization of minerals. In: Hobbs, B.E., Heard, H.C. (Eds.), *Mineral and rock deformation: laboratory studies; the Paterson volume*. Geophysical monograph 36, 161-199.
- Vernon, R.H., 1976. *Metamorphic processes. Reactions and microstructure development*. George Allen & Unwin Ltd., London, 247 pp.
- Viggiani, G., Küntz, M., Desrues, J., 2001. An experimental investigation of the relationships between grain size distribution and shear banding in sand. In: Vermeer, P.A., Diebels, S., Ehlers, W., Herrmann, H.J., Luding, S., Ramm, E. (Eds.), *Continuous and discontinuous modelling of cohesive-frictional materials*. Springer, Berlin, Heidelberg, New York, 111-127.
- Vigneresse, J.L., Barbey, P., Cuney, M., 1996. Rheological transitions during partial melting and crystallization with application to felsic magma segregation and transfer. *Journal of Petrology* 37, 1579-1600.
- Vigneresse, J.L., Tikoff, B., 1999. Strain partitioning during melting and crystallizing felsic magmas. *Tectonophysics* 312, 117-132.
- Waff, H.S., 1980. Effects of the gravitational field on liquid distribution in partial melts within the upper mantle. *Journal of Geophysical Research* 85, 1815-1825.
- Waff, H., and Faul, U.H., 1992. Effects of crystalline anisotropy on fluid distribution in ultramafic partial melts. *Journal of Geophysical Research* 97, 9003-9014.
- Walte, N.P., Bons, P.D., Passchier, C.W., Koehn, D., 2003. Disequilibrium melt distribution during static recrystallization. *Geology* 31, 1009-1012.
- Wark, D.A., Watson, E.B., 1998. Grain-scale permeability of texturally equilibrated, monomineralic rocks. *Earth and Planetary Science Letters* 164, 591-605.
- Wark, D.A., Williams, C.A., Watson, E.B., Price, J.D., 2003. Reassessment of pore shapes in microstructurally equilibrated rocks, with implications for permeability of the upper mantle: *Journal of Geophysical Research* 108, 2050, DOI 10.1029/2001JB001575.
- Wearie, D., Rivier, N., 1984. Soap, cells and statistics—Random patterns in two dimensions. *Contemporary Physics* 25, 59-99.
- Weinberg, R.F., Podladchikov, Y.Y., 1994. Diapiric ascent of magmas through power law crust and mantle. *Journal of Geophysical Research* 99, 9543-9559.
- Weinberg, R.F., 1999. Mesoscale pervasive felsic magma migration, alternatives to dyking. In: Sial, A.N., Stephens, W.E., Ferreira, V.P. (Eds.), *Granites, crustal evolution and associated mineralization*. *Lithos* 46, 393-410.
- Wiggins, C., Spiegelman, M., 1995. Magma migration and magmatic solitary waves in 3-D. *Geophysical Research Letters* 22, 1289-1292.
- Weaire, D., Rivier, N., 1984. Soap, cells and statistics - random patterns in two dimensions. *Contemporary Physics* 25, 59-99.
- Wyllie, P.D., 1988. Magma genesis, plate tectonics, and chemical differentiation of the Earth. *Reviews in Geophysics* 26, 370-404.
- Xu, Yaqin, Zimmerman, M.E., Kohlstedt, D.L., 2004. Deformation behaviour of partially molten mantle rocks. In: Karner, G.D., Taylor, B., Driscoll, N.W., Kohlstedt, D.L. (Eds.), *Rheology and deformation of the lithosphere at continental margins*. *Margins theoretical and experimental Earth science series*.
- Zhu, W., Hirth, G., 2003. A network model for permeability in partially molten rocks. *Earth and Planetary Science Letters* 212, 407-416.

## Zusammenfassung

Das Verhalten von Schmelzen und Fluiden im Kornmaßstab bestimmt wichtige Parameter in teilgeschmolzenen Systemen wie z.B. deren Porosität-Permeabilität und Rheologie. Somit übt die kleinräumige ( $\mu\text{m}$  bis  $\text{mm}$ ) Schmelzverteilung einen direkten Einfluss auf großräumige geologische Prozesse wie z.B. die Schmelzsegregation und Migration an Mittelozeanischen Rücken oder Subduktionszonen aus. Obwohl viele der grundlegenden Mechanismen der Gleichgewichtsschmelzverteilung im Kornmaßstab gut bekannt sind, ist der mögliche Einfluss von parallel ablaufenden Prozessen wie z.B. Rekristallisation, Deformation oder chemischem Ungleichgewicht auf die Schmelzverteilung bisher noch unsicher. Für die vorliegende Arbeit wurden Analogexperimente mit Norcamphor-Ethanol und partiell geschmolzenem  $\text{KNO}_3$ - $\text{LiNO}_3$  durchgeführt, die es ermöglichen, die Wechselwirkungen zwischen der Schmelzverteilung im Gleichgewicht und den verschiedenen modifizierenden Faktoren *in-situ* zu beobachten. Das Norcamphor-Ethanol System hat einen Benetzungswinkel von ca.  $25^\circ$  und gleicht in der Hinsicht natürlichen geschmolzenen System wie z.B. Quarz oder Olivin plus Schmelze. Statische Experimente mit Norcamphor-Ethanol ergaben, dass Rekristallisation kontinuierlich zu einer lokalen Ungleichgewichtsverteilung von der Schmelze führt (4. Kapitel). Der normalerweise als statisch angenommenen charakteristischen Benetzungswinkel in dem Analogsystem wurde ebenfalls durch Kornwachstum verändert. Der dynamische Benetzungswinkel ist hierbei eine Funktion der Geschwindigkeit, mit der sich die fest-fest-flüssig Grenze bewegt (5. Kapitel).

Bei Deformationsexperimenten (6. Kapitel) wurden abhängig von der Schmelzfraktion drei unterschiedliche Deformationsregimes beobachtet. Bei über 10 Vol.% Schmelzanteil deformierte das Aggregate durch granuläres Fließen und Kompaktion. Bei einer Flüssigkeitsfraktion  $< 8$ -10 Vol.% wurde das Korngrenzgleiten in Scherzonen lokalisiert, die wenig deformierende Kornaggregate voneinander abgrenzten. Unterhalb einer systemspezifischen Flüssigkeitsfraktion bildeten sich zusammenhängende Aggregate aus allen Kristallen, welches intern z.B. kristallplastisch deformiert wurde. Die Schmelzsegregation in den Experimenten hing von dem jeweiligen Deformationsmechanismus ab. Korngrenzgleiten oder granuläres Fließen hielt eine bestimmte geometrisch notwendige Flüssigkeitsfraktion in dem deformierenden Gebiet (z.B. in einer Scherzone), während die Flüssigkeit sehr effizient aus kristallplastisch deformierenden Bereichen gepresst wurde (6. Kapitel).

Während der Deformation durch granuläres Fließen oder Korngrenzgleiten kam es außerdem zu einem „dynamische Benetzung“ genannten Prozess, bei dem normalerweise nichtbenetzende Flüssigkeiten (z.B. Gasblasen im Norcamphor) ein temporäres

Flüssigkeitsnetzwerk bilden konnten (7. Kapitel). Diese Prozesse wurden mit der Bildung und den Konsequenzen von dynamischen Benetzungswinkeln erklärt.



## **Danksagung**



## **Lebenslauf**

**Nicolas Walte**

Geboren am 12.03.1974 in Bremen, Deutschland

Staatsbürger der Bundesrepublik Deutschland

Aktuelle Adresse:     c/o Fleischhammer  
                              Rhabanusstraße 17  
                              55118 Mainz

**e-mail:**                 walte@mail.uni-mainz.de

- 1995-1998**     Studium der Geologie/Paläontologie an der Ruprecht Karls Universität Heidelberg.
- 1998-2001**     Studium der Geologie/paläontologie an der Johannes Gutenberg-Universität Mainz. Abschluss als Diplom Geologe/Paläontologe.
- 2001-2004**     Doktorarbeit im Rahmen des Graduiertenkollegs „Stoffbestand und Entwicklung von Mantel und Kruste“ an der Johannes Gutenberg-Universität Mainz.



